Deterministic and stochastic dynamics in bacterial systems

Dissertation

zur Erlangung des
Doktorgrades der Naturwissenschaften
(Dr. rer. nat.)

dem Fachbereich Physik
der Philipps-Universität Marburg
vorgelegt von

Felix Konrad Schmidt

aus Frankfurt am Main
Marburg, 2019

Vom Fachbereich Physik der Philipps-Universität Marburg (Hochschulkennziffer 1180) als Dissertation angenommen am:

Author Felix Konrad Schmidt

Erstgutachter Bruno Eckhardt
Fachbereich Physik
Philipps Universität Marburg

Zweitgutachter Knut Drescher
Fachbereich Physik
Philipps Universität Marburg

Tag der mündlichen Prüfung: 16.07.2019

Abstract

Microorganisms form an essential part of our biosphere and represent roughly 14 percent of the biomass on earth. In spite of this abundance, the majority of chemical and physical processes governing the live of microorganisms remain poorly understood. In this work, we focus on three different phenomena from the realm of microorganisms and aim to explain the physical processes behind them. We examine how the bacterium Shewanella Putrefaciens exploits a mechanical instability to wrap its flagellum around its cell body, effectively forming a screw that allows the bacterium to escape from traps. Based on a numerical model we study the onset of screw formation in dependence of the flagellar geometry and the existence of multiple equilibrium configurations of the flagellum.

Furthermore, we study the effects of actively swimming microorganisms on the diffusion of passive tracer particles. By means of a numerical simulation we examine a single swimmer-tracer interaction and use the results to develop a model based on continuous time random walks that captures a series of swimmer-tracer interactions. We derive an analytical expression for the one dimensional probability density function of the tracer displacements and use numerical simulations to approximate the two- and three-dimensional distributions. We then extend the model to include periods of free tracer diffusion between the tracer-swimmer interactions and fit this extended model to a number of experimentally observed tracer distributions.

In the third part of this work we examine how the cylindrical shape of a bacterium affects the isotropic trajectories of membrane proteins when observed with a microscope. We derive an analytical expression for the anisotropic distribution of the particle displacements when projected in the observation plane and use this result to calculate the mean squared displacement curves. Finally, we use numerical simulations to study the effects of a limited focus depth and to understand the resulting challenges for the estimation of the diffusion coefficients.

Zusammenfassung

Mikroorganismen sind ein wichtiger Bestandteil unserer Biosphäre und machen rund 14 Prozent der Biomasse der Erde aus. Trotz ihrer Allgegenwärtigkeit ist ein Großteil der

physikalischen und chemischen Prozesse die in und um Mikroorgansimen ablaufen noch unerforscht. In dieser Arbeit werden drei dieser Prozesse genauer betrachtet und erklärt. Wir untersuchen wie das Bakterium Shewanella Putrefaciens eine mechanische Instabilität seines Flagellums verwendet um dieses um seinen Zellkörper zu wickeln und damit eine Schraube formt, die es ihm erlaubt sich aus Hindernissen zu befreien. Anhand eines numerischen Models wird dabei untersucht welchen Einfluss die Geometrie des Flagellums und das Vorhandensein mehrerer Gleichgewichtskonfigurationen auf das Formen der Schraube hat.

Des Weiteren untersuchen wir den Einfluss von aktiv schwimmenden Mikroorganismen auf die Diffusion von passiven Tracer Partikeln. Mit Hilfe von numerischen Simulationen untersuchen wir den Ablauf einer einzelnen Schwimmer-Tracer Interaktion und entwickeln daraus ein Modell, das mit Hilfe von zeitlich kontinuierlichen "Random Walks" eine Serie von Schwimmer-Tracer Interaktionen beschreibt. Wir entwickeln einen analytischen Ausdruck für die Wahrscheinlichkeitsdichte Funktion der Tracer Verschiebungen in einer Dimension und verwenden numerische Simulationen um die Verteilungen in zwei und drei Dimensionen zu nähern. Anschließend erweitern wir das Model, so dass die Tracerpartikel zwischen den Interaktionen mit den Schwimmern frei diffundieren können und fitten dieses erweiterte Modell an eine Reihe von experimentell beobachteten Tracer Verschiebungs Verteilungen.

Im dritten Teil dieser Arbeit wird untersucht, welchen Einfluss die zylindrische Form eines Bakteriums auf die, mit einem Mikroskop beobachteten Trajektorien von Membranproteinen hat. Wir entwickeln einen analytischen Ausdruck für die anisotrope Verteilung der Verschiebungen der Proteine, die durch die Projektion in die Beobachtungsebene entsteht und berechnen damit die mittleren quadratischen Verschiebungen. Abschließend untersuchen wir mit Hilfe von numerischen Simulationen den Einfluss einer begrenzten Fokus Höhe auf die beobachtbaren Trajektorien um die resultierenden Herausforderungen bei der Bestimmung der Diffusionskonstanten dieser Proteine zu verstehen.

Contents

1 Introduction

Microorganisms are central to earths biosphere. They can be found in almost all regions on earth Bar-On et al., 2018 including even extreme areas as hydrothermal vents in the deep sea Glud et al., 2013, the arctic permafrost regions Vazquez et al., 1995; Michaud et al., 2004 or acidic volcanic springs Reed et al., 2013. In spite of their importance and their seeming simplicity compared to complex multicellular organisms like animals, a large part of the live of microorganisms and the complex processes that drive them remains poorly understood. Advances in the field of microbiology, especially the development of gene sequencing- and editing-techniques have led to a wealth of new datasets and enabled researchers to take control over parts of the complex chemical processes that take place in the cells. Combined with modern microscopy techniques these processes can be studied in great detail, partly even at single molecule level. But even with these advanced techniques, the large amount of different species of microorganisms in combination with their various living conditions the This work focuses on microorganisms living in aqueous conditions and aims to explain three physical phenomena that arise

This work is organized as follows: In the second chapter we explore a new mechanism that allows the bacterium *Shewanella Putrefaciens* to escape from obstacles in its environment. We use a numerical model to study the onset of screw formation under various conditions. The model is constructed to include polymorphic shape changes of the flagellum and allows the combination of building blocks with different geometries.

In the third chapter we focus on the question how a number of active swimming microorganisms affect the diffusion of passive tracer particles in a solution. We develop a theoretical framework based on continuous time random walks that models the tracer diffusion as a series of swimmer-tracer-interactions and allows us to study the probability distribution of the tracer displacement over time. The resulting distributions are compared to data obtained by experiments with genetically modified strains of *Shewanella Putrefaciens* that demonstrate different swimming patterns.

The fourth chapter focuses on the diffusion of particles on the surface of a bacterial cell. We explain how the cylindrical shape of the bacteria affects the tracer trajectories observed via microscopy and seek to understand the consequences for the estimation of diffusion coefficients.

2 The bacterial screw

Recent observations of the monotrichous strain of the bacterium *Shewanella putrefaciens* with a fluorescently labeled flagellar filament revealed a new way how bacteria use their flagellum to escape from obstacles and avoid getting trapped. This escape mechanism is driven by a polymorphic transition of the flagellum, causing the filament to wrap around the cell body in a screw-like motion.

We start this chapter with a short overview of the biological relevance and the structure of the flagellum and continue with a detailed description of the observations and corresponding experimental conditions. We then introduce a numerical model that is capable of simulating the bacterial flagellum and study the different conditions that lead to flagellar screw formation. We further extend the model to examine the effect of different spatial organizations of the two building blocks that form the flagellum of *S. putrefaciens*.

2.1 The bacterial flagellum

Over time microorganisms have developed a number of different motility mechanisms. One of these mechanisms is the bacterial flagellum, a helical filament that extends from the cell surface and is connected to a rotary motor embedded in the cell membrane. The ways in which the flagellum is used by bacteria are diverse. The primary function is locomotion, but flagella are also known to play a major role in biofilm formation Pratt and Kolter, 1998; Klausen et al., 2003 and can act as a sensor for external conditions Wang et al., 2005.

The number of flagella per cell and their location on the cell body vary for different strains of bacteria and are categorized into multiple groups. Peritrichous bacteria like the well studied organism *Escherichia coli* or the wild-type strain of *Shewanella putrefaciens*, one of the model organisms used in this work, have multiple flagella projecting in all directions over the cell body. In contrast, monotrichous bacteria have a single flagellum, mostly located at one of the cell poles. Examples for monotrichous bacteria are the human pathogen *Vibrio cholerae* or the $\Delta flagL$ mutant of *S. putrefaciens* for which the formation of lateral flagella is suppressed by the mutation.

The flagellum is divided into two functionally distinct regions. The part closest to the cell is the flagellar hook, a short, flexible region connecting the rotary motor and the filament. Depending on the species under observation, the hook region is between $0.01\mu m$ and $0.05\mu m$ long. It functions as a universal joint, transmitting torque generated by the motor to the filament over a wide range of bending angles relative to the motor axis Samatey et al., 2004.

The flagellar filament is the dominant part of the flagellum and reaches a typical length of up to several cell body lengths. In the case of *Shewanella* the polar flagellum is approximately $6.5\mu m$ long Kühn et al., 2017. The flagellar rotation is driven by a molecular motor which is anchored in the cell membrane. For most bacteria it is powered by a flow of protons or, in the case of some marine species, by sodium ions Berg, 2003. This flow is induced by a chemical gradient across the membrane. For experiments with fluorescent beads attached to short fragments of flagellar filament the proton driven motor is reported to rotate at frequencies of up to 350 Hz Chen and Berg, 2000; Berg and Turner, 1993; Berg, 2003. For bacteria with a sodium-driven motor, rotation rates up to 1800 Hz have been observed Magariyama et al., 1994; Magariyama et al., 1995. For a wide range of frequencies, the motor creates a constant torque which decreases linearly above a critical frequency Berg, 2003; Berg and Turner, 1993.

2.1.1 Molecular structure and polymorphism

The basic building block of the flagellar filament is a protein called flagellin. Different variants of flagellin are combined to form larger structures, the protofilaments. By arranging eleven of these protofilaments in a circular structure, the flagellar filament is formed which is basically a hollow tube. During the construction process, the flagellin proteins are transported through the tube and assemble at the end, gradually increasing the length of the flagellum. Due to their spiral staircase-like arrangement the protofilaments impose an intrinsic curvature onto the macroscopic structure, resulting in the typical helical shape. For a variety of bacteria, different variations of flagellin have been reported Fujii et al., 2008, corresponding to changes in geometrical and mechanical properties of the flagellum.

In addition to these variations due to different flagellin types, a number of experiments have demonstrated that the flagellum is capable of changing the arrangement of its protofilaments under different external influences, like mechanical forces and torques, changes in pH value, temperature or salinity Kamiya and Asakura, 1976b; Kamiya and Asakura, 1976a; Hasegawa et al., 1982; Hotani, 1980; Seville et al., 1993; Macnab and Ornston, 1977; Darnton and Berg, 2007. These changes occur because a flagellin monomer may adopt two different conformations, called R-state and L-state Calladine, 1975; Darnton and Berg, 2007. These states differ in their molecular shape. To accommodate for these differences, the arrangement of protofilaments has to adapt, resulting in distinct helical structures.

Furthermore, the flagella of most bacteria include multiple types of flagellins, often spatially organized along the filament due to the temporal order in which they are synthesized. Kostrzynska et al., 1991. For example, *S. putrefaciens* has two types of flagellin, called major- and minor-flagellin, that locate in different flagellar regions. To achieve this arrangement, the cells always maintain a low concentration of minor flagellin proteins inside the cytosol in order to quickly construct the base of a new flagellum. The production of major flagellins is then started once the concentration of minor flagellin decreases due to their utilization in the construction process Kühn et al., 2018. The question why *Shewanella* and other bacteria retain multiple flagellin types is a focus of current research and is partly answered in this chapter.

2.2 Observation of the bacterial screw

Many bacteria live in structured environments like sediments or organic tissues where different obstacles, cavities or changes in the environmental viscosity restrict their motion. To move efficiently under these conditions, bacteria have developed different strategies Ranjard and Richaume, 2001; Mannik et al., 2009; Cisneros et al., 2006; Wei et al., 2011. Recent experiments with a monoflagelated variant of *S. putrefaciens* that has fluorescently dyed filament uncovered a new mechanism how cells use their flagellum to escape from traps and increase their overall mobility in structured environments.

With a single flagellum, the cells are capable of moving forward and backward by rotating their flagellum counter-clockwise (CCW) or clockwise (CW). In contrast to many peritrichous bacteria, where the flagellar handedness changes together with the sense of rotation, the flagellum of monoflagelated bacteria has to keep its handedness (left-handed for *Shewanella*) to allow for bidirectional swimming.

Recent studies performed by Son et al. Son et al., 2013 and Xie et al. Xie et al., 2011 demonstrated that in order to change their swimming direction, these bacteria exploit a buckling instability to quickly reorient the flagellum and generate a lateral force on the cell body, resulting in a reorientation of the latter. This instability occurs during the pushing phase when the cellular motor torque is increased, resulting in a high load on the flagellar base.

Although this mechanism is a good way to change the swimming direction of the bacterium, there are cases where it is not sufficient to free the cell from small cavities. Then a new escape mechanism becomes active which is depicted in figure 2.1. When the cell body gets trapped, the cell tries to escape by regular backward motion, rotating the flagellum clockwise. If the pulling force generated by the filament is not sufficient, the cell presumably increase its motor torque. At some point, the flagellum is pulled towards the cell body and starts to wrap around the latter, forming a helical screw. This screw rotates around the cell body and enables the cell to slowly move backwards again and thereby to escape from the trap. For cells swimming freely in an aqueous solution, screw formation is hardly observed at all - less than 5% of the active cells showed screws. Experiments conducted by M. Kühn Kühn et al., 2017 demonstrated that the frequency at which the cells start to form a screw can be increased by the addition of Ficoll® to the swimming medium. Ficoll® is a mixture of long-chained polymers that increase the fluid viscosity Fissell et al., 2009. As depicted in figure 2.2, the percentage of cells forming a screw increases almost linearly with the Ficoll® concentration. Measurements of the swimming speed demonstrated that cells move significantly slower in screw mode compared to cells with a regularly formed flagellum (figure 2.2). Therefore, the screw offers an advantage for trapped cells only while it is an disadvantage under obstacle-free swimming conditions and has to be avoided in this environment.

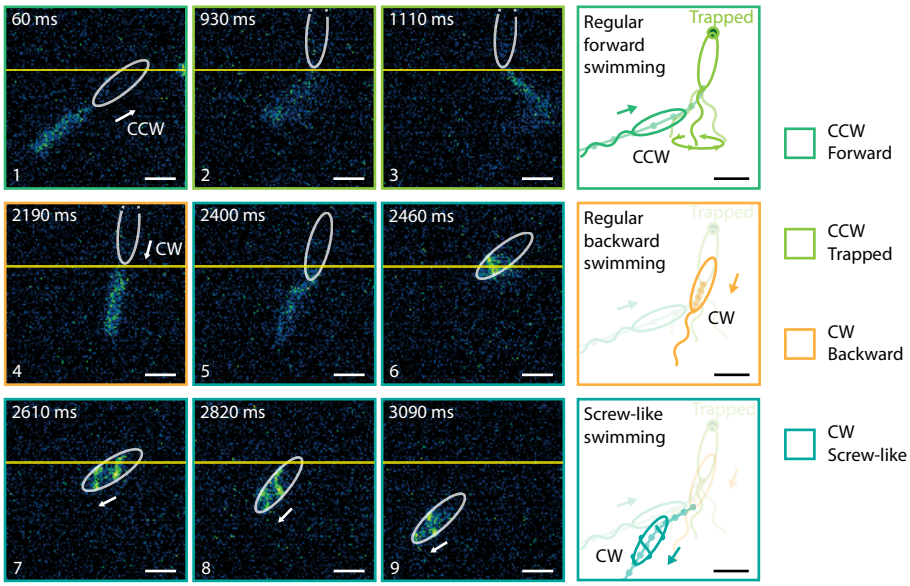

Fig. 2.1: Time series of micrograph images showing screw formation. The flagellum was labeled with a fluorescent dye and images were recorded with an exposure time of 30 ms. The cell starts in forward swimming mode (1) and is trapped by an obstacle (2-3). The cell switches to clockwise rotation (4) but fails to escape with regular backward swimming (5). By further increasing the motor torque, the flagellum is pulled towards the cell body (5). During this motion, the filament wraps around the cell body, forming a screw (6-7). The screw enables the cell to move again and to escape from the trap. Pictures are provided by M. Kühn Kühn et al., 2017.

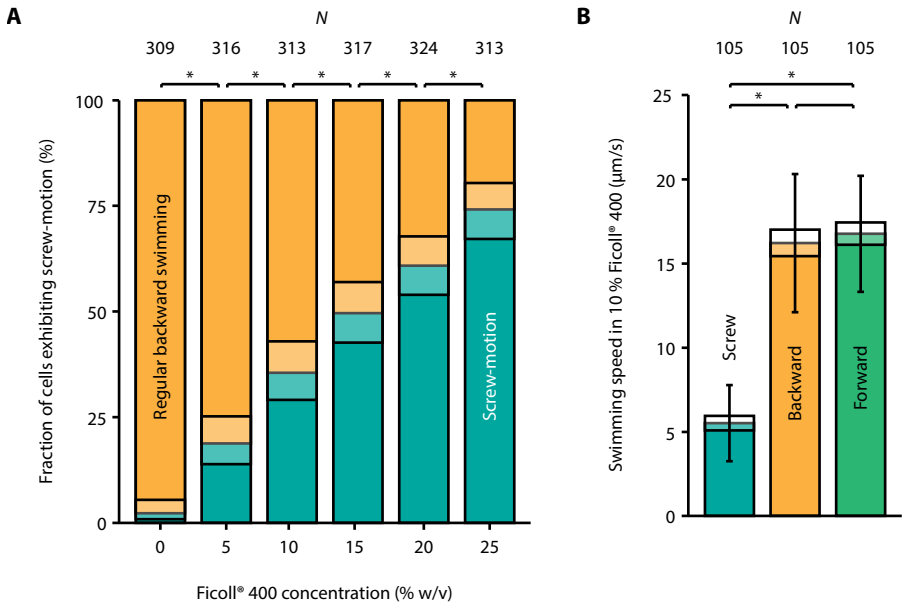

Fig. 2.2: (A) Proportion of cells forming a screw during observation time for increasing weight per volume (% w/v) concentrations of Ficoll®. Significant differences according to Fisher's exact test of independence between the different conditions are denoted by the * symbol. N is the number of observed cells for each condition and the standard deviation is indicated by light colors. (B) Swimming speed of *S. putrefaciens* in LB medium with increased viscosity. Diagram provided by M. Kühn Kühn et al., 2017.

2.3 Dynamics of the helical flagellum

A detailed analysis of microscopy images demonstrates that the screw formation is initiated at the flagellar base and accompanied by a distortion of the helical shape. These findings suggest that mechanical instabilities are a key factor for the occurrence of the screw; they will be investigated here.

Theoretical work on filaments is capable of capturing the nonlinear dynamics and corresponding shape changes for straight filaments under selected boundary conditions Goriely and Tabor, 2000; Powers, 2010 or predicting the propulsion efficiency of undistorted helices Lighthill, 1976; Rodenborn et al., 2013. In order to capture both hydrodynamic and dynamical shape changes, one has to rely on numerical simulations. Many experiments explore a parameter range where the model flagellum retains its helical shape Liu et al., 2011 or study the dynamics of a straight filament Coq et al., 2008. In a recent experiment, Jawed et al. Jawed et al., 2015 studied the behavior of a rotating steel helix in glycerin, creating a system similar to the bacterial flagellum. They did not report the observation of a screw but noted strong deviations from the helical shape for increased motor torques. Although these macroscopic experiments are quite instructive, numerical models offer a greater flexibility and are used by a large number of recent studies on flagellar dynamics. Many of these focus on peritrichous bacteria and the effects of flagellar bundling or the characteristics of swarming motility. The property of interest for the understanding of the flagellar screw is the dynamic stability of the flagellum's helical shape. An overview of the helical stability and shape transitions under changing motor torques is provided by Vogel and Stark, 2012. Another study by Park et al. Park et al., 2017 based on a numerical model explores the effects of numerous geometrical and mechanical parameters e.g. helical radius or length of the flagellum. In the pushing state, both studies predict a stable rotation with a nearly undistorted helical shape up to a critical motor torque. For higher torques, the flagellum starts to depart from its initial helical shape and precesses around the cell axis. For even higher torques, the flagellum undergoes strong shape transitions and rotates in an irregular fashion.

Both studies do not include the repulsive potential of the cell body or that of the flagellum, which are necessary for screw formation. They also use different approaches to model the hook region, a potentially important factor for screw formation, since it is responsible for the torque transmission between motor and flagellum. A recent study by Adhyapak and Stark Adhyapak and Stark, 2016 which focused on the reverse rotation of the lateral flagella of *E. coli* reported strong flagellar shape deformations. The study included repulsive interaction of both the cell body as well as the filament, but no screw-like behavior was reported.

To understand the details of screw formation, a numerical model based on the work of Vogel et al. is used to study the dynamics under different conditions. The model is introduced in the next section.

2.4 Theory of elastic filaments

To model the mechanical properties of the flagellum we, assume that Hook's law is valid, that is, the forces caused by small deformations of the flagellum increase linearly with the magnitude of the perturbations. We make use of the Frenet-Serret equations to effectively characterize the flagellum's conformation. For that purpose, we parametrize its spacecurve $\mathbf{r}(s)$ by the arc length s and introduce the tangent vector $\mathbf{t}(s) = \partial_s \mathbf{r}(s)$ which is pointing along the local tangent of $\mathbf{r}(s)$. Its derivative with respect to s gives the local curvature κ, a measure for the deviation of the spacecurve from a straight line,

$$\kappa(s) = \left| \frac{\partial \mathbf{t}(s)}{\partial s} \right|. \tag{2.1}$$

For a space curve with non-vanishing curvature, one can introduce the normal vector $\mathbf{n}(s) = \partial_s \mathbf{t}(s)/\kappa(s)$, a vector orthogonal to $\mathbf{t}(s)$. Together with the binomial vector $\mathbf{b} = \mathbf{t} \times \mathbf{n}$, $\boldsymbol{t}$ and $\boldsymbol{n}$ form a right-handed orthogonal basis, the Frenet frame. With the help of $\mathbf{b}$ and $\mathbf{n}$, the torsion of the system is defined as

$$\tau(s) = -\partial_s \mathbf{b}(s) \cdot \mathbf{n}(s). \tag{2.2}$$

For given $\kappa(s)$ and $\tau(s)$, one can reconstruct the Frenet frame by solving the Frenet-Serret relations, a system of differential equations,

$$\partial_s \mathbf{t}(s) = \kappa(s)\mathbf{n}(s), \tag{2.3}$$
$$\partial_s \mathbf{n}(s) = -\kappa(s)\mathbf{t}(s) + \tau(s)\mathbf{b}(s), \tag{2.4}$$
$$\partial_s \mathbf{b}(s) = -\tau(s)\mathbf{n}(s). \tag{2.5}$$

In order to represent the filament's material frame, we introduce a left-handed trihedron of unit vectors $\mathbf{f}(s), \mathbf{v}(s), \mathbf{u}(s)$, where $\mathbf{u}(s)$ is tangential to $\mathbf{r}(s)$, while $\mathbf{f}(s)$ and $\mathbf{v}(s)$ are normal to $\mathbf{r}(s)$. The evolution of $\mathbf{f}, \mathbf{v}, \mathbf{u}$ with s is characterized by the equation

$$\partial_s \mathbf{e}(s) = \boldsymbol{\Omega}(s) \times \mathbf{e}(s) \tag{2.6}$$

where $\mathbf{e}$ stands for either $\mathbf{f}$, $\mathbf{v}$ or $\mathbf{u}$. The angular strain vector $\boldsymbol{\Omega}$ contains information about the change of the orientation of the material frame, similar to curvature and torsion for the Frenet frame. However, in contrast to the latter, the angular strain vector also includes information about the local twist of the material frame around the tangent vector $\mathbf{u}$. By introducing the twist angle ϕ we can express $\boldsymbol{\Omega}$ in terms of κ and τ,

$$\Omega_1 = \kappa \sin\phi, \tag{2.7}$$
$$\Omega_2 = \kappa \cos\phi, \tag{2.8}$$
$$\Omega_3 = \tau + \partial_s \phi. \tag{2.9}$$

Since the flagellum has a circular cross section, we may set $\phi = 0$ and represent the flagellum's configuration at rest with the strain vector $\boldsymbol{\Omega}_0 = (0, \kappa_0, \tau_0)$. Since flagellar curvature and torsion are hard to observe directly, we have to derive them from observable

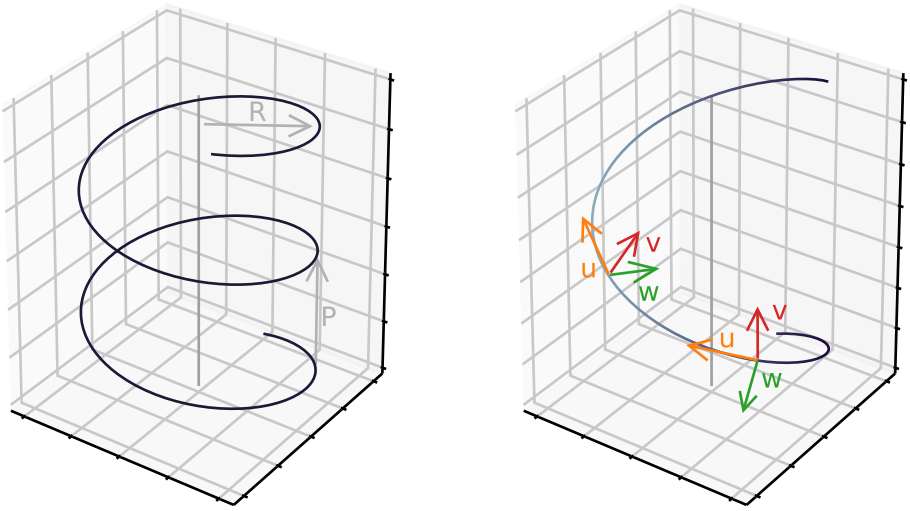

Fig. 2.3: A helix and its parameters and parameterizations. (Left) Illustration of a helix with radius R and pitch P. (Right) Sketch of a helical filament with the material frame represented by the vectors $\mathbf{u}(s)$, $\mathbf{v}(s)$ and $\mathbf{f}(s)$; the frame moves with the position along the helix measured by the arc-length s according to (2.6).

quantities. Consequently, the configuration of a helical filament is best expressed in terms of pitch P and helix radius R (see Fig. 2.3), which are related to κ and τ by

$$\tau = \frac{2\pi P}{4\pi^2 R^2 + P^2}, \tag{2.10}$$

$$\kappa = \frac{4\pi^2 R}{4\pi^2 R^2 + P^2}. \tag{2.11}$$

To model the dynamics of the filament we use Kirchhoff's theory for elastic rods. One of its main assumption is that while local bending of the filament can lead to large global displacements, the changes in the local coordinate system of the material frame remain small and can be described with linear elasticity theory. Kirchhoff's theory expresses the elastic free energy of a filament in terms of its present deformation $\mathbf{\Omega}$ from its ground state $\mathbf{\Omega}_0$ as

$$\mathcal{F}_K = \int_0^L f_{el}(\mathbf{\Omega}, \mathbf{\Omega_0}) ds \tag{2.12}$$

$$= \int_0^L \frac{A}{2}\left[\Omega_1^2 + (\Omega_2 - \kappa_0)^2\right] + \frac{C}{2}(\Omega_3 - \tau_0)^2 \, ds, \tag{2.13}$$

where A and C are material parameters, corresponding to bending stiffness and torsional rigidity Landau and Lifshitz, 1986 and L is the total contour length of the filament. In section 2.7.1, we will extend this model expression by including multiple ground states to account for flagellar polymorphism. The mechanical forces $\mathbf{f}_{el}$ and torques $\mathbf{m}_{el}$ resulting

from these deviations are derived by forming the functional derivative of $\mathcal{F}_K$ with respect to $\mathbf{r}$ and twist angle ϕ, i.e.

$$\mathbf{f}_{el} = \frac{\delta \mathcal{F}}{\delta \mathbf{r}}, \tag{2.14}$$

$$\mathbf{m}_{el} = \frac{\delta \mathcal{F}}{\delta \phi}\mathbf{u}. \tag{2.15}$$

2.5 Numerical model

In the numerical representation, the flagellum is divided into N discrete segments each of which is characterized by a position $\mathbf{r}_i$ and a local tripod of unit vectors ($\mathbf{f}^{(i)}$, $\mathbf{v}^{(i)}$, $\mathbf{u}^{(i)}$) corresponding to the material frame introduced earlier. The points are distributed uniformly along the flagellum so that each segment has a length $h = L_0/N$, where L_0 is the filament's total contour length. The unit vectors $\mathbf{u}_i$ are related to the positions by $\mathbf{u}_i = (\mathbf{r}_{i+1} - \mathbf{r}_i)/|\mathbf{r}_{i+1} - \mathbf{r}_i|$. The normal vectors $\mathbf{f}_i$ for the initial helix configuration are obtained from the relation $\mathbf{f_i} = (\mathbf{u}_{i-1} \times \mathbf{u}_i)/\sin(\theta_i)$, where θ_i is the angle included by segment $i-1$ and i. For each time-step of the simulation, $\mathbf{f_i}$ is adjusted following a procedure proposed by Chirico and Langowski Chirico, 1996. The orientation of $\mathbf{v}_i$ is completely characterized by $\mathbf{v}_i = \mathbf{u}_i \times \mathbf{f}_i$.

The local strain $\mathbf{\Omega}$ for each segment is calculated as

$$\Omega_1^i = -\frac{\theta_i}{\mathbf{u}_i \cdot \mathbf{u}_{i+1}}\mathbf{v}_i \cdot \mathbf{u}_{i+1}, \tag{2.16}$$

$$\Omega_2^i = \frac{\theta_i}{\mathbf{u}_i \cdot \mathbf{u}_{i+1}}\mathbf{f}_i \cdot \mathbf{u}_{i+1}, \tag{2.17}$$

$$\Omega_3^i = \phi_i \tag{2.18}$$

where ϕ_i is the local twist angle. By following the derivations in Vogel, 2012, ϕ_i can be expressed as

$$\sin\phi_i = \cos\theta_i\,(\mathbf{v}_i \cdot \mathbf{f}_{i+1}) - (\mathbf{v}_i \cdot \mathbf{u}_{i+1})\,(\mathbf{u}_i \cdot \mathbf{f}_{i+1}) + \frac{(\mathbf{f}_i \cdot \mathbf{u}_{i+1})\,(\mathbf{u}_i \cdot \mathbf{v}_{i+1})}{1+\cos\theta_i}. \tag{2.19}$$

To control the amount of stretching of the flagellum, the global harmonic spring potential

$$\mathcal{F}_S = (K/2)\int_0^L (\partial\mathbf{r}/\partial s)^2\, ds \tag{2.20}$$

is added. The elastic constant K keeps the relative variations in length below 0.1 per cent.

As in the continuous case above, the elastic forces and torques follow from the functional derivative $\delta\mathcal{F}/\delta\mathbf{r}$ and $\delta\mathcal{F}/\delta\phi\mathbf{u}$ of the combined functional $\mathcal{F}_K + \mathcal{F}_S$. The expression for the stretching force is derived analytically, so that, for instance, the force acting on segment i is given by

$$\mathbf{F}_s^i = -K\left[(L_i - L_0)\,\mathbf{u}_i - (L_{i+1} - L_0)\,\mathbf{u}_{i+1}\right], \tag{2.21}$$

while the free energy derivatives corresponding to bending and twisting forces are calculated by finite differences.

The flagellum's rotation is driven by a constant motor torque $\mathbf{M}_0$ which is applied to the first segment. To account for the effects of the bacterial hook which is much more flexible than the flagellum Son et al., 2013, this segment is allowed to rotate freely and thereby transmit the torque to the following segments. The dynamics of the motor segment are described by

$$\omega_0 = \mu_0 \left[\mathbf{M}_0^z + \mathbf{M}_0^u - A\left[\left(\Omega_1 - \Omega_{0,1}\right)\mathbf{f}_0 + \left(\Omega_2 - \Omega_{0,2}\right)\mathbf{v}_0\right] - C\left(\Omega_3 - \Omega_{0,3}\right)\mathbf{u}_0\right], \tag{2.22}$$

where $\mathbf{M}_0^z = M_0(\sqrt{1-\alpha^2\sin^2\phi} - \alpha\cos\phi)\mathbf{e}_z$ and $\mathbf{M}_0^u = \alpha M_0 \mathbf{u_1}$. The parameter α is used to control the amount of torque that acts along the filament independently of its orientation. ϕ is the angle between the tangential motor segment u_0 and the first filament segment u_1. The variable μ_0 is the motor segment's self mobility and depends on the rotational and translational friction. To the last segment, torque free boundary conditions are applied.

In addition to the elastic forces, we account for interactions between the flagellum and the cell body as well as interactions between different flagellar segments, that are caused by strong shape deformations. The cell body is modeled as a cylindrical object of radius $R_{cell} = 0.45\mu m$ that is sufficiently long, so that the flagellum does not pass underneath it. The filament is assumed to be $20nm$ thick and distances between approaching segments are computed following a procedure proposed by Adhyapak and Stark Adhyapak and Stark, 2016. In both cases, the repulsion between different flagellar segments or the cell body was modeled with a Lennard-Jones type potential truncated at its minimum,

$$\Phi_c = \begin{cases} \epsilon\left[\left(r_m/r\right)^{12} - 2\left(r_m/r\right)^6\right], & \text{if } r \le r_m \\ 0, & \text{otherwise} \end{cases} \tag{2.23}$$

where r_m is either the cell- or filament radius and ϵ is the strength of the potential, so that the forces vary continuously

For the frictional forces, we use resistive force theory Lighthill, 1976. The local motion of the flagellum's segments is characterized by three local friction coefficients Lighthill, 1976 that depend on the geometry of the flagellum.

$$\gamma_\perp = \frac{4\pi\eta}{\ln\left(0.09l/r_f\right) + 1/2} \tag{2.24}$$

is the friction coefficient for motion perpendicular to the flagellum's centerline, where η is the viscosity, r_f is the filament radius and $l = \sqrt{4\pi^2R^2 + P^2}$ is the contour length of one helical turn. The tangential friction coefficient is given by

$$\gamma_\parallel = \frac{2\pi\eta}{\ln\left(0.09l/r_f\right)} \tag{2.25}$$

and the friction encountered by the filament during rotation is

$$\gamma_{rot} = 4\pi\eta r_f^2. \tag{2.26}$$

The mobilities μ_t and μ_r that enter the equation of motion are related to the friction coefficients by

$$\mu_t = \mathbf{u}_i \otimes \mathbf{u}_i / \gamma_p + (1 - \mathbf{u}_i \otimes \mathbf{u}_i) / \gamma_n \tag{2.27}$$

and

$$\mu_r = 1/\gamma_r. \tag{2.28}$$

The translational equation of motion for segment i is expressed in terms of the elastic force $\mathbf{F}_{el}$, the stretching force $\mathbf{F}_{st}$ and the repulsive forces $\mathbf{F}_c$ and $\mathbf{F}_{fl}$ resulting from filament-cell as well as filament-filament interactions. It is given by

$$\frac{\partial \mathbf{r}_i}{\partial t} = \mu_t \left(\mathbf{F}_{i,el} + \mathbf{F}_{i,st} + \mathbf{F}_{i,c} + \mathbf{F}_{i,fl} \right). \tag{2.29}$$

The change in the torsion angle ϕ_i of segment i depends on the elastic torque M_{el} only:

$$\frac{\partial \phi_i}{\partial t} = \mu_r M_{i,el}, \tag{2.30}$$

To achieve high numerical accuracy while keeping the computational costs low, the equations of motions were integrated using the Cash-Karp method Cash and Karp, 1990, a high-order Runge-Kutta integrator with embedded error estimation and step size control. During each partial integration step, the segment positions are updated in a first step as $\mathbf{r}_i(t + h_t) = \mathbf{r}_i(t) + h_t \mathbf{v}_i$, where $\mathbf{v}_i = \frac{\partial \mathbf{r}_i}{\partial t}$ and h_t is the partial step size. Using the new positions and $\omega_i = \frac{\partial \phi_i}{\partial t}$ the attached tripods are aligned in a second step, following the procedure proposed by Chirico and Langowski Chirico, 1996.

2.5.1 Initial conditions and parameters

Following the observations described in Kühn et al., 2017, we choose a left-handed helix with $P = 2.0\mu m$ and $R = 0.35\mu m$ for *Shewanella*, resulting in $\tau = 1.42\mu m^{-1}$ and $\kappa = 1.56\mu m^{-1}$. The contour length of the flagellum is set to $L_c = 6\mu m$ corresponding to 2 helical turns and the discretization length is $h = 0.15\mu m$, comparable to the values taken by Vogel and Stark.

For the elastic constants A and C introduced in equation (2.12), no direct measurements have been reported so far. As a starting point, force measurements of the response to deformations of a flagellum as well as observations based on thermal fluctuations for certain bacterial strains provide rough estimates of the filamentous bending and twisting stiffnesses Darnton and Berg, 2007; Fujime et al., 1972; Hoshikawa and Kamiya, 1985; Trachtenberg and Hammel, 1992. While the flagellum's crystal structure differs from that of well studied organisms like *E. coli*, we anticipate that its mechanical properties will not differ significantly from that of *E. coli* and hence choose the values $A = C = 3.5pN\mu m^2$ in accordance to the values obtained by Darnton et al. Darnton and Berg, 2007. We also used values between $A = C = 2.5pN\mu m^2$ and $A = C = 4pN\mu m^2$ to study the influence of the rigidity on the screw formation, without noting significant differences in the qualitatively behavior. Therefore, the use of the values obtained by Darnton is justified. The various parameters used in the simulation and their values are summarized in table 2.1.

	Flagellin type	Major		Minor
Parameter	Description	Stretched	Coiled	Stretched
R	Helical radius	0.315 μm	0.42 μm	0.175 μm
P	Helical pitch	1.91 μm	1.43 μm	1.18 μm
κ	Curvature	1.64 $\mu^{-1}m$	1.83 $\mu^{-1}m$	2.66 μm^{-1}
τ	Torsion	-1.59 μm^{-1}	-0.99 μm^{-1}	-2.91 $\mu^{-1}m$
L_c	Contour length	6.5 μm		
A	Bending rigidity	3.5 $pN\mu m^2$		
C	Twisting rigidity	3.5 $pN\mu m^2$		
K	Stretching stiffness	10000 $pN\mu/m$		
R_{cell}	Cell radius	0.45 μm		
H_{cell}	Cell height	3.0 μm		
$\gamma_\perp$	Friction coefficient, normal to flagellum	2.85 η	2.80 η	3.25 η
$\gamma_\parallel$	Friction coefficient, parallel to flagellum	1.61 η	1.57 η	1.86 η
γ_r	Rotational friction coefficient	0.0012 η		
η	Viscosity	0.001 Pas		
h_0	Segment length	0.125 μm		

Tab. 2.1: Parameters of the numerical model and the values used for the simulations.

2.6 Stability and dynamics of screw formation

In this section, we characterize the flagellar dynamics that leads to screw formation. We start by analyzing the stability of the flagellum's helical shape for different motor torques, comparing the results to previous studies.

With the parameters listed in table 2.1, a number of simulations with motor torques M_0 ranging from $-8pN\mu m$ to $8pN\mu m$ were performed. The simulations were initialized with a resting flagellum in its equilibrium configuration, followed by a short acceleration phase of $T = 10ms$ in which the motor torque was linearly increased up to its final value. One should note that a negative torque corresponds to forward motion for the left-handed helix of *S. putrefaciens*. The hook friction coefficient was set to $\alpha_h = 0$ and the integration time for each run was $150ms$. This setup corresponds to the study performed by Vogel et al. Vogel and Stark, 2012, with a helix geometry adapted to *S. putrefaciens*. To characterize the shape transitions and the overall dynamical behavior, the position and strain vectors of the resulting motion, as well as the forces F_c acting on the first segment respectively the cell body are recoded. To quantify and locate deviations from the helical ground state, the elastic free energy density (2.12) is calculated along the flagellum. As a measure of the rotational dynamics the frequency spectrum is obtained by means of a fast Fourier transform. The observed behavior for a negative motor torque as depicted in figure 2.4 is qualitatively similar to the results reported in Vogel and Stark, 2012, with an inverted sign of the torque due to a right handed model helix. For small torques, the flagellum undergoes only slight shape change and angular motion is dominated by a single frequency. The pushing force F_c increases linear with M_0, in agreement with the predictions of resistive force theory for a rotating helix, as derived by Lighthill Lighthill, 1976. Above a critical motor torque of $M_{c1} = -2.84pN\mu m$, the flagellum starts to precess around the cell axis and a second frequency is observed in the spectrum. This behavior shows up in the force

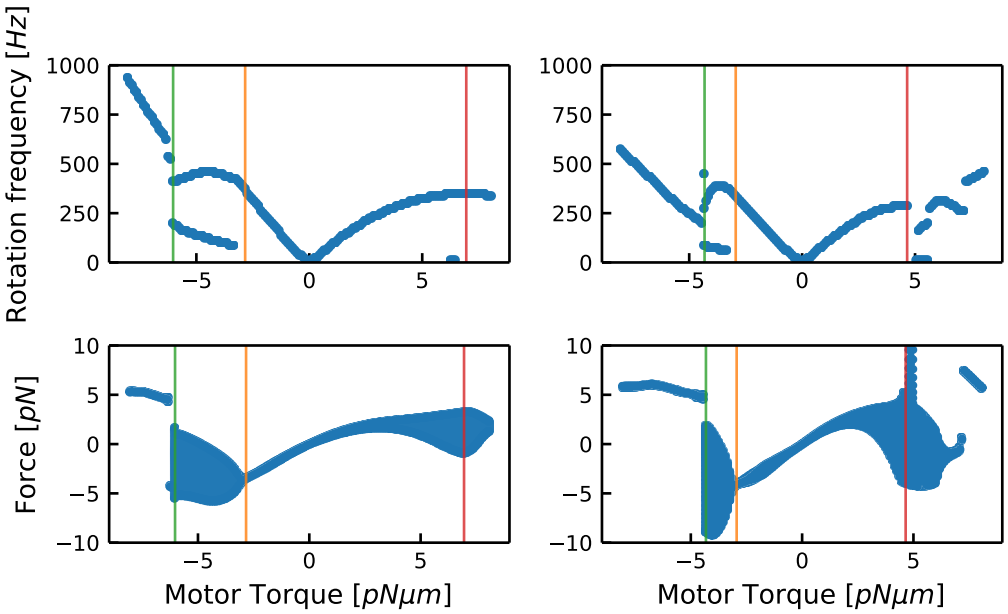

Fig. 2.4: Flagellar rotation frequency and force exerted on the cell body by the flagellum for increasing motor torques after a simulation time of $T = 0.5s$. The hook friction coefficient is set to $\alpha_h = 0$ (left column) and $\alpha_h = 0.4$ (right column), respectively. For forward swimming mode ($M_0 < 0$), the flagellum rotates around the cellular axis in a stable fashion and the pushing force increases linearly with M_0. For a critical motor torque ($M_{c1} = -2.84pN\mu m$ for $\alpha_h = 0.0$ and $M_{c1} = -2.94pN\mu m$ for $\alpha_h = 0.4$) (orange line), a second frequency appears in the spectrum and the flagellum slowly precesses about the cellular axis. For even stronger negative motor torques ($M_{c2} = -6.03pN\mu m$ for $\alpha_h = 0.0$ and $M_{c2} = -4.32pN\mu m$ for $\alpha_h = 0.4$) (green line), the flagellum starts to whirl around. In backward swimming mode ($M_0 > 0$), rotation is unstable and the flagellar axis slowly moves away from the cell axis, visible by the increasing spread between maximal and minimal force. Above a value of $M_{c3} = 6.95pN\mu m$ for $\alpha = 0.0$ and $M_{c3} = 4.65pN\mu m$ for $\alpha_h = 0.4$ (red line), the flagellum starts to partly unwind at its base, with the hook being almost perpendicular to the cellular axis. This behavior compensates the flagellar drift. For $\alpha_h = 0.4$, an additional transition is visible in the force diagram: for $M_{c4} > 7.15pN\mu m$ the flagellum is already pulled towards the cell body but is not able to form screws. Complete screw formation starts for $M_{screw} > 7.95pN\mu m$.

diagram as oscillations in the force acting on the cell body. Above a second critical torque of $M_{c2} = -6.03pN\mu m$, additional frequencies appear in the system and the flagellum is significantly deformed.

For positive motor torques the flagellum starts to rotate clockwise. In contrast to forward motion, the force acting on the cell is only approximately characterized by a linear dependence on M_0 and oscillates even for small motor torques.

While for counter-clockwise rotation at low angular velocities the flagellum remains aligned with the cell axis, backward motion is unstable: the helical axis slowly deviates from the cell axis, approaching a perpendicular orientation to the latter. This drift was already reported by Vogel et al. Vogel and Stark, 2012 and is visible in the force diagram 2.4 by the increasing spread between minimal and maximal force. For the fixed cell body in the simulation, the sideways motion results in an increased force component radial to the cell axis. For a free cell body, the radial force should lead to a reorientation of the cell body and a change in swimming direction, realigning cellular and helical axis and thereby compensating the flagellar drift Nguyen and Graham, 2017.

For small positive motor torques with $M_0 < 2pN\mu m$ the flagellum is only slightly deformed and slowly moves away from the cellular axis. For stronger motor torques the flagellar drift increases and the force acting along the cell axis starts to oscillate with an increasing amplitude as depicted in figure 2.6. Above a value of $M_{c3} > 6.95pN\mu m$ the flagellum starts to partially unwind at its base but continues to rotate in this configuration. The hook bends to the side and assumes an orientation almost perpendicular to the cell axis. For increasing motor torques, this configuration decreases the flagellar sidewards drift, with an almost vanishing drift for $M_0 = 8.0pN\mu m$. The previous simulation procedure was repeated with a nonzero hook friction parameter of $\alpha_h = 0.4$ to characterize its influence on flagellar dynamics. For small positive and negative torques the results remain similar to the model without hook friction, as the flagellum retains its equilibrium configuration and the hook has only minor influence. For stronger motor torques and the corresponding deformations and deviations form the cellular axis, the hook segment starts to deviate from its equilibrium configuration and hook friction becomes relevant. This influence is visible in the force diagram of figure 2.4: while the qualitative behavior remains similar, the transition between the individual domains occurs at different torques: The change from regular, single-frequency rotation to the regime with a second frequency happens at $M_{c1} = -2.94pN\mu m$, whereas the flagellum changes into whirling motion at $M_{c2} = -6.03pN\mu m$. In backward swimming mode, the sidewards drift is increased by hook friction, as indicated by the larger force spread, while partial unwinding at the flagellar base already starts at $M_{c3} = 4.65pN\mu m$ and a complete drift compensation happens at $M_0 = 6.95pN\mu m$. For positive motor torques above M_{c3}, the partial unwinding causes the hook to point sidewards, assuming an almost perpendicular orientation to the cell axis. In this configuration and with $\alpha_h = 0.4$, the torque transmitted by the hook includes a component that pulls the flagellum towards the cell body, as in the zero hook friction case, but also maintains the rotation around the cell axis. For motor torques with $M_0 < 7.15pN\mu m$ this pulling component is too small to actually pull the flagellum to the cell body, but for $M_0 > 7.15pN\mu m$ the flagellum starts to partially approach the cell body and finally forms complete screws for $M_{screw} > 7.95pN\mu m$. Details of this process are depicted in figure 2.5. This process is a direct way to form a screw that happens

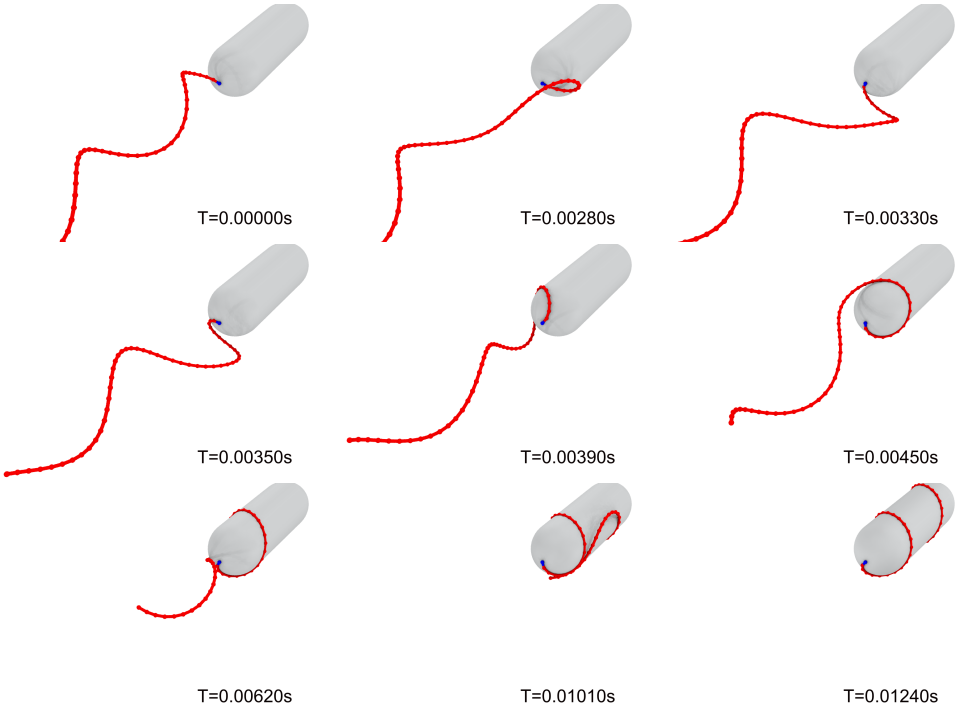

Fig. 2.5: Numerical simulation of direct screw formation with a single polymorphic state. The flagellum is driven by a motor torque of $M_0 = 8.0pN\mu m$ and a hook friction index of $\alpha_h = 0.4$ is used. Starting from a resting flagellum, the filament partly unwinds at its base ($t = 2.8ms$) and bends outwards ($t = 3.3ms$). This extended region is pulled towards the cell body ($t = 3.3ms - 3.8ms$) and starts to wind around the latter ($t = 3.9ms$), effectively inverting its orientation. The remaining flagellum gradually approaches the cell body and the region of inversely oriented segments moves along the filament, while roughly keeping its spatial location ($t = 4.5ms - 11ms$) until the whole flagellum is changed into the screw form. For $t > 12ms$ the flagellum continues to rotate around the cell body, retaining the displayed screw configuration.

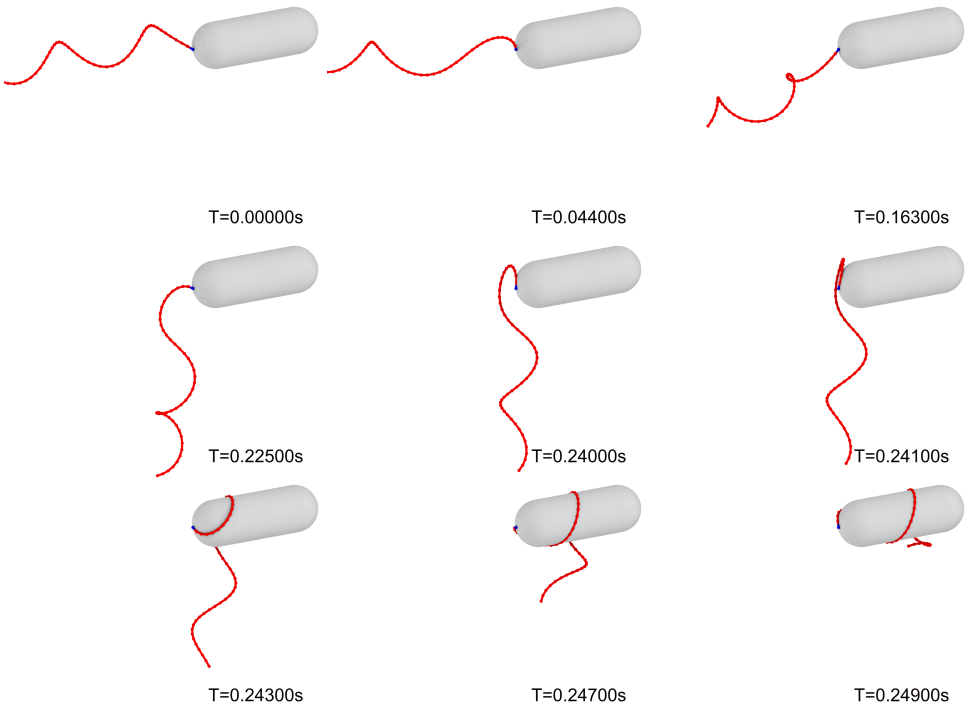

Fig. 2.6: Numerical simulation of indirect screw formation with a single conformational state. The motor torque is set to $M_0 = 4pN\mu m$ and a hook friction index of $\alpha_h = 0.6$ is used. Over the course of the simulation, the flagellum drifts sideways and assumes an almost perpendicular position to the cell axis. In this configuration, the flagellar base segments get into contact with the cell body and the screw starts to form.

rather quickly, since once the first segments start to wrap around the cell body, the screw forms within 2-3 revolutions of the flagellum.

Comparing the onset of direct screw formation for different hook frictions parameters and motor torques reveals that an increase of hook friction up to $\alpha_h = 0.65$ decreases the torque needed to form a screw. For $\alpha_h > 0.65$ the efficiency of hook formation decreases again. A second mechanism that leads to screw formation is based on the aforementioned sidewards drift of the flagellum. When the filament reaches an almost perpendicular orientation to the cell axis, the first flagellar segments touch the cell body and again hook friction leads to a rotation around the cell body of these segments, enabling the formation of a screw. This process happens even at smaller motor torques, but is significantly slower since the flagellum has to approach the perpendicular orientation first. An important prerequisite for this indirect screw formation is the limited response of the cell body to sidewards forces, since the body of a free moving cell would realign with the flagellum. Assuming that under free swimming conditions, the cell body would reorientate due to the frictional sidewards forces this second kind of screw formation should not be observed. One should note that although the flagellum temporally assumes a perpendicular orientation during the strong shape fluctuation for high motor torques in forward swimming phase, the handedness of the helical geometry prevents the formation of a screw for counter clockwise rotation.

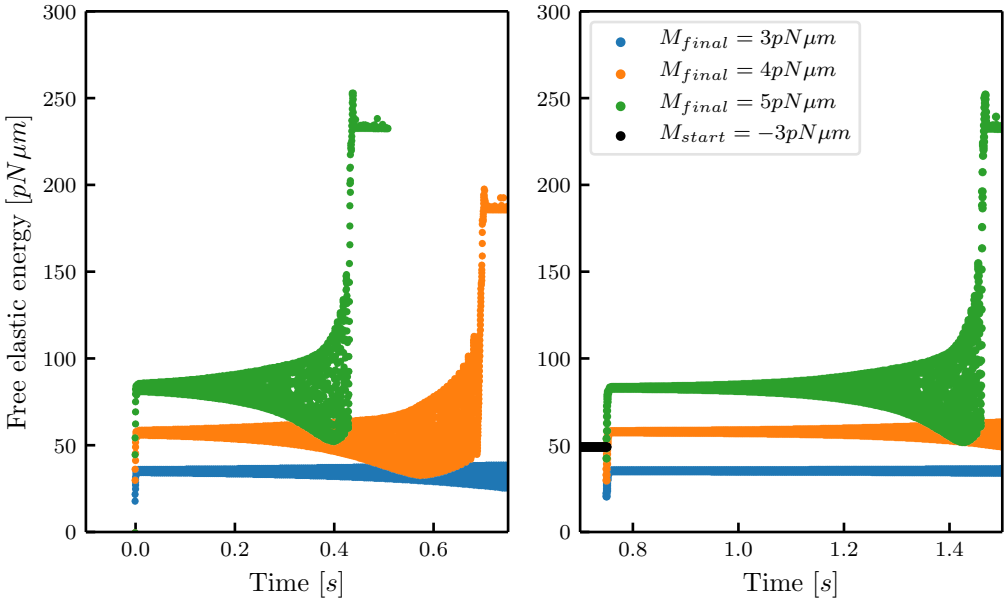

Fig. 2.7: Elastic free energy over time for static (left) and non-resting initial (right) conditions. For a simulation with dynamical initial conditions and a hook friction coefficient of $\alpha = 0.4$, the starting motor torque is set to $M_0 = -3pN\mu m$ leading to the stable motion with oscillations in the forces and buckling described above. After $t = 0.75s$ the torque is linearly increased over $T_{inc} = 0.01$ to its final value. For matching motor torques, the flagellum evolves comparable, although for resting initial conditions, the elastic energy oscillations start with a higher amplitude and lead to a shorter drift phase, resulting in an earlier onset of indirect screw formation.

2.6.1 Screw formation for non-resting flagellum

Although the previously used initial conditions with a resting flagellum are appropriate for studying stability and shape transformation, they do not comply with the experimentally observed phenomenon where the screw formation is preceded by a shift from counter-clockwise to clockwise rotation or an increase of motor torque during backward swimming. To account for this fact, the simulation is extended to use a flagellum that includes the shape deformations caused by clockwise and counter clockwise rotation with a moderate motor torque of $M_0 = 3pN\mu m$ respectively $M_0 = -3pN\mu m$. The hook friction coefficient is set to $\alpha = 0.4$. Starting from these conditions, the torque is linearly increased to the selected value M_{final}. Using the elastic free energy density to characterize deviations from the ground state, the time evolution of the non-resting initial conditions is compared to its resting counterpart. For the extreme case of a transition from forward to backward swimming, we observe that for final motor torques $M_{final} < 7.3pN\mu m$ both initial conditions converge to the same rotating helix configuration. The dynamical starting condition takes longer since it first reverses the shape deformations resulting from the counter-clockwise motion. As depicted in figure 2.7, the non resting starting conditions result in a higher initial spread of the elastic energy which is further increased due to the unstable nature of clockwise rotation. For the dynamical initial conditions, the spread increases as well, but starts with a smaller amplitude and thereby delays the drift process.

For higher final motor torques, the observed behavior remains comparable, although the resting initial conditions promote direct screw formation, as screws are already observed at a slightly lower final motor torque of $M_{final,r} = 7.95pN\mu m$ compared to $M_{final,d} = 8.05pN\mu m$ for the non-resting initial conditions. These differences become even smaller for the second case where the simulation starts from an already clockwise rotating flagellum and the torque is increased. Based on this small difference and to keep the number of free parameters small, all simulations start from the resting initial state unless stated otherwise.

2.7 Polymorphic extension

2.7.1 Numerical model of polymorphism

Although the current model is capable of explaining direct screw formation for relatively high motor torques, the shape changes and the resulting elastic forces are incompatible with the rigid structure of the flagellar filament. To resolve this limitation, the model is extended to include polymorphic transitions.

Assuming that the flagellum has N different configurations, each conformational state i corresponds to a minimum in the elastic free energy H_i with a specific torsion τ_i and curvature κ_i. Different procedures to model flagellar polymorphism based on multiple energy minima were introduced by Goldstein et al. Goldstein et al., 2000; Coombs et al., 2002, Wada and Netz Wada and Netz, 2008 and Vogel and Stark Vogel and Stark, 2010. Based on the ideas proposed in the latter publication, the elastic free energy density is defined as

$$f_{el,p} = \min_{\alpha=1\ldots N} \left\{ f_{el,s} \left(\Omega, \Omega_{0,\alpha} \right) + \delta_\alpha \right\}, \tag{2.31}$$

where $\mathbf{\Omega}_{0,\alpha}$ are the rest strain vectors for the different conformational states which are indicated by α. The variable $f_{el,s}$ is the elastic free energy density (2.12) with a single state only. The parameter δ_α sets the energy difference between state α and the ground state $\delta_0 = 0$.

Since the helical geometries for *S. Putrefaciens* are not fully characterized, the model includes two states only, namely the stretched state of the initial helix $\Omega_{0,s}$ and the coiled state of the screw $\Omega_{0,c}$. The energy difference was set to a value of $\delta_s = 0.1pN$ as in Vogel and Stark, 2010.

2.7.2 Screw formation and stability of polymorph model

The extended model was evaluated for different motor torques and hook parameters α_h and the results were analyzed using the same approach as in the previous section. As initial condition, the same helix configuration with $\tau_{0,s} = -1.59\mu m^{-1}$ and $\kappa_{0,s} = 1.64\mu m^{-1}$ as in section 2.6 was used, while the second configuration with $\tau_{0,c} = -0.99\mu m^{-1}$ and $\kappa_{0,c} = 1.83\mu m^{-1}$ corresponds to the flagellum in screw mode. All relevant parameters are listed in table 2.1.

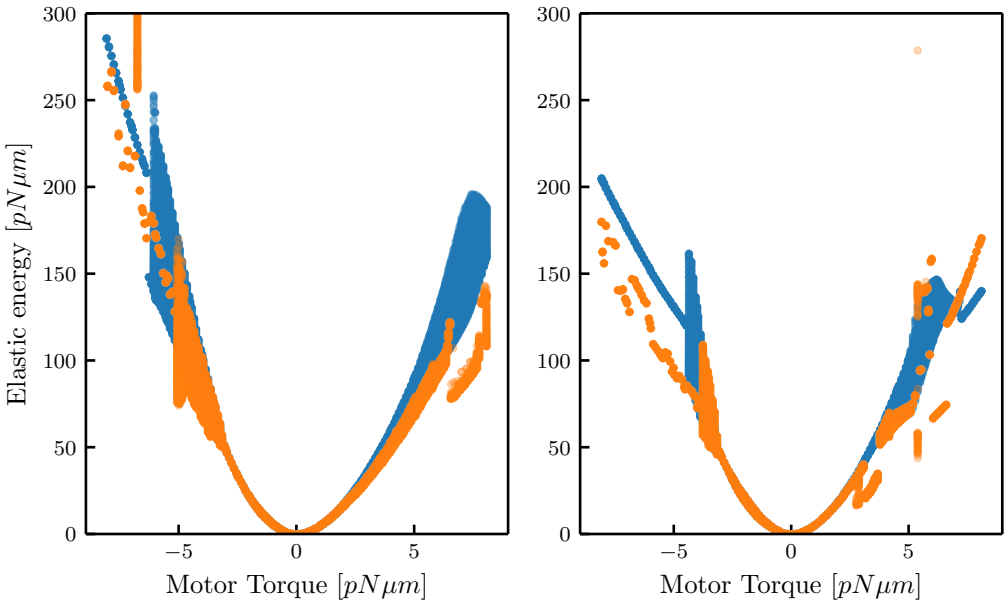

Fig. 2.8: Elastic free energy of the single-state and two-state polymorphic flagellum model for motor torques between $M_0 = -8pN\mu m$ and $M_0 = 8pN\mu m$. For small M_0, the elastic free energy increases quadratically for the hook friction coefficients $\alpha_h = 0.$ (left) and $\alpha_h = 0.4$ (right). For forward swimming, the polymorphic model (orange) as well as the single-state model (blue) exhibit a change from rotations with a single constant free energy at small motor torques to oscillatory behavior with a changing free energy. For stronger negative torques, the flagellum changes into another state where the elastic energy becomes constant over time again. Due to the unstable nature of backward motion, both models display oscillations in the elastic energy that become more pronounced with higher torques. The increase in elastic energy of the two-state model is smaller compared to the single state model, since an increasing number of segments changes into the favorable coiled state. With a hook friction coefficient of $\alpha_h = 0.4$, the two-state model has multiple discontinuities in the energy curve, accompanied by dynamic conformational state changes and direct screw formation at motor torques above $M_{c3} = 5.32pN\mu m$.

For small motor torques both models exhibit similar forces and frequencies. This behavior is in accordance with the fact that polymorphic states are separated by an energy barrier δ_s which is not crossed for small motor torques and the weak forces associated with them. For stronger torques, the flagellum is significantly deformed and a growing number of segments change into coiled state. For counter-clockwise rotations, this transition happens at lower torques since the deformations lead to a energetically favorable path in the energy potential as shown in figure 2.8.

Comparing the onset of screw formation under the different experimental conditions to the single-state model reveals screw formation for smaller torques. Although the deformations remain comparable to the single-state flagellum, the second state reduces the maximal elastic free energy density during screw formation.

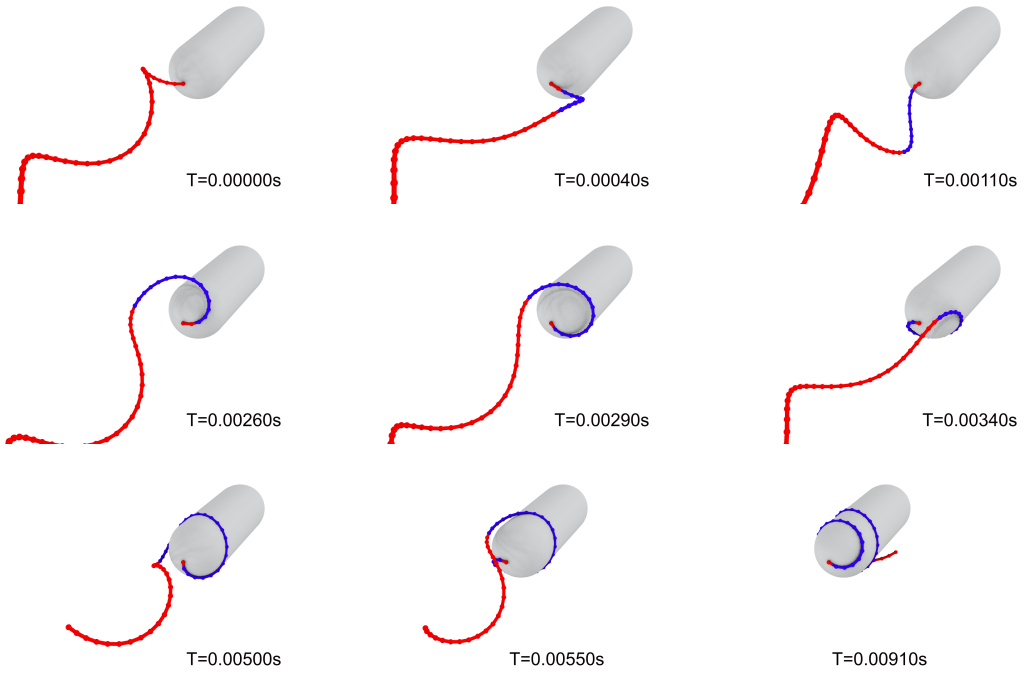

Fig. 2.9: Numerical simulation of direct screw formation with two polymorphic states. The flagellum is driven by a motor torque of $M_0 = 6.5pN\mu m$ and a hook friction index of $\alpha_h = 0.4$ is used. The current conformation of each segment is color coded with red indicating the stretched state and blue the coiled state as introduced in section 2.7.1. When the motor torque is turned on, the first segments rapidly switch into coiled state and the flagellum starts to partially unwind again. The subsequent process is similar to single-state screw formation, with the exception that an increasing number of filament segment switch into coiled state as they approach the cell body. This change reduces the energy that is needed to deform the flagellum and allows screw formation at lower torques compared to the single-state model.

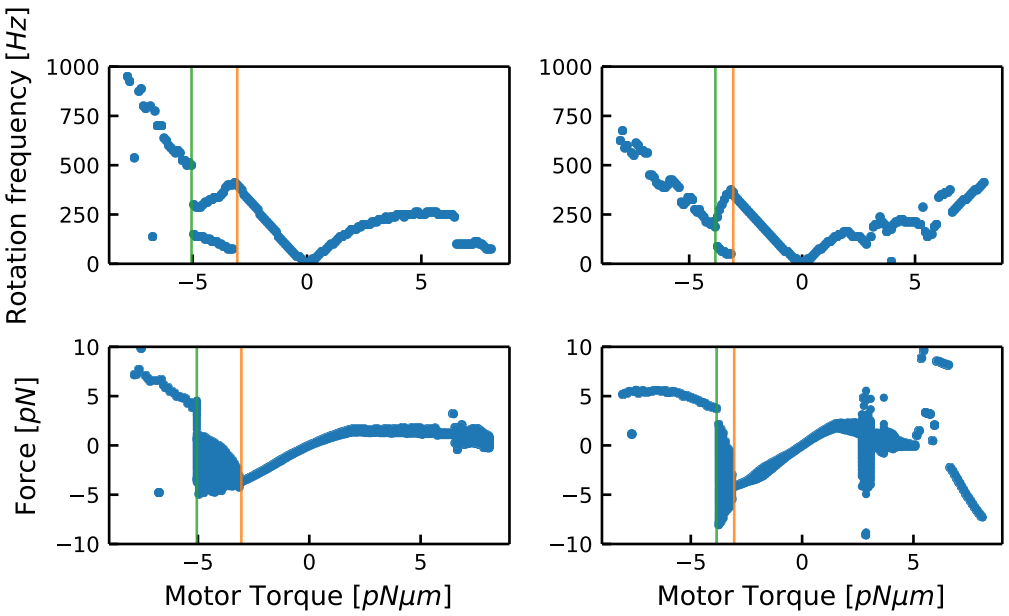

Fig. 2.10: Dependence of flagellar forces and frequencies on motor torques for the two-state polymorphic model. The hook friction coefficient is set to $\alpha_h = 0$ (left column) and $\alpha_h = 0.4$ (right column). The simulation was run for $T = 0.5s$. For forward swimming motion, the flagellum changes from stable rotation to buckling and to whirling motion. The transitions are located at $M_{c1} = -3.04pN\mu m$ (green line) and $M_{c2} = -5.05pN\mu m$ (orange line) for $\alpha_h = 0.$ and at $M_{c1} = -3.04pN\mu m$ and $M_{c2} = -3.84pN\mu m$ for $\alpha_h = 0.4$. For clockwise rotation and the case $\alpha_h = 0$, the flagellum displays only marginal drift and small fluctuations in the pulling force while for $\alpha_h = 0.4$ transitions between both conformational states lead to large fluctuation in the force diagram at a motor torque of $M_{c3} = 2.64pN\mu m$. Direct screw formation is observable above $M_{screw} = 5.32pN\mu m$.

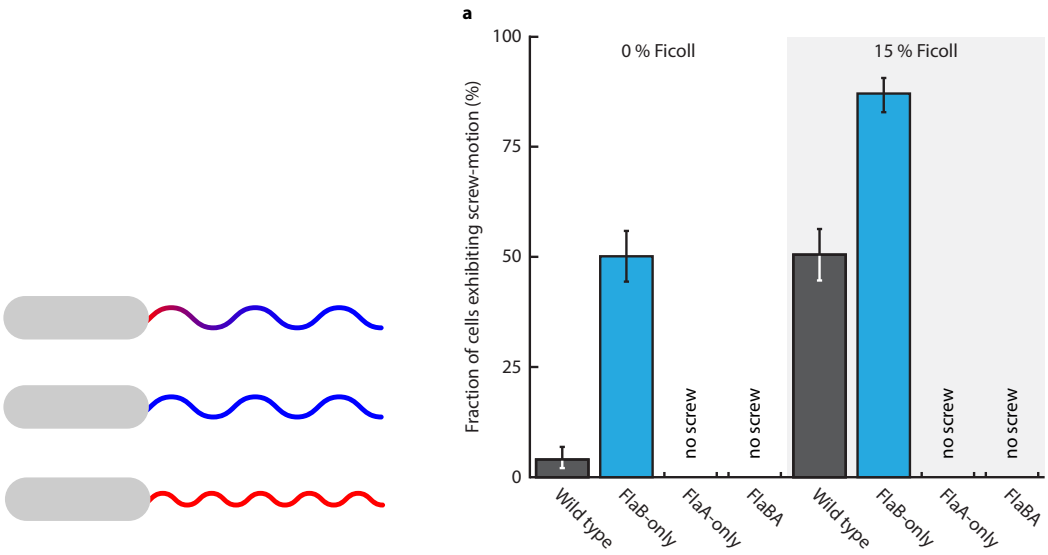

Fig. 2.11: (Left) Cartoon of flagellum composition for different mutants: The wild type (top) is composed of major (blue) and minor flagellin (red), while the FlaA-mutant (middle) is composed of minor flagellin only and FlaB (bottom) contains only major flagellin. (Right) Fraction of experimentally observed cells displaying screw-formation. Data provided by M Kühn Kühn et al., 2018

2.8 Screw formation with inhomogeneous flagellum

To understand how the arrangement of major and minor flagellin components in the flagellum affects screw formation and the swimming process, a number of experiments were performed by M Kühn Kühn et al., 2018. *S. putrefaciens* was genetically modified to obtain strains with defined variations in the spatial placement of major and minor flagellin. In the first mutant FlaA_1, the gene related to major flagellin production was deleted, resulting in a strain with a flagellum composed of minor flagellin only. The opposite was achieved for the second mutant FlaB_1, resulting in a major flagellin flagellum. The third mutant FlaBA features flagella that contain minor and major flagellin, but the order in which they are inserted into the flagellum are reversed compared to the wild type. The different configurations are illustrated in figure 2.11. To study the effects of mutations, the same experimental setup as in section 2.2 was used to record time lapse images. The observed flagellar morphology was characterized by measuring the helical radii, pitches and contour lengths. The results are summarized in figure 2.12. Although the contour length remains comparable for all mutants, the geometry of the flagellum consisting only of minor flagellin differs significantly from the other mutants by exhibiting a helix with smaller radius and pitch but an increased number of helical turns. Other remarkable inter-mutant differences were found by calculating the relation between flagella observed in regular form and screw mode, see fig. 2.11. Under standard viscosity conditions, the FlaB_1 mutant forms considerably more screws than the wild type (5% for wild type compared to 50% for the mutant). This increase still holds for high viscosity conditions, where roughly 50% of the wild type cells and 85% of the FlaB_1

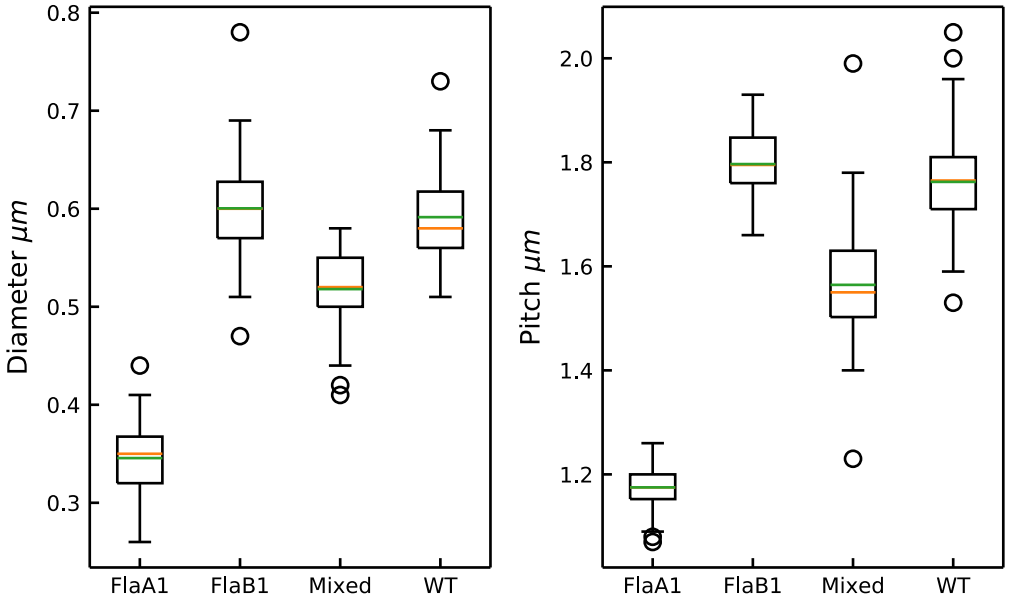

Fig. 2.12: Box-and-whisker plot of the experimentally observed helix parameters for different strains. The yellow and green lines mark the median and mean of the distributions. The size of the boxes corresponds to the interquartile range, namely the difference between upper and lower quartile. The length of the whiskers was chosen in accordance to the definition given by Mc Gill and Tukey Mcgill et al., 1978 and outliers are marked as circles.

mutant were observed in screw mode. The opposite effect is observed for the minor flagellin mutant FlaA_1 for which no screw was formed under any experimental conditions. To account for these variations in the filament, the numerical model was further extended to allow for a flagellum with individual torsion and twist coefficients for each segment. The major flagellin mutant is assumed to consist of two polymorphic states, again corresponding to regular and screw state. Since no screw was observed for the minor flagellin at all, no information about a second conformational state is available and the corresponding segments were modeled with a single state only. In addition, it is assumed that both flagellin variants have similar elastic properties, that is, equal parameters A, C and K.

2.8.1 Minor flagellin mutant

In order to investigate if the change in helix geometry is sufficient to prohibit screw formation for the minor flagellin mutant, the numerical simulation was run with increasing motor torques and varying hook friction coefficients, following the procedure outlined in section 2.6. The helical pitch was set to $P = 1.17$ and the radius to $R = 0.175$, corresponding to observations of the FlaA_1 strain (Figure 2.12). For all other simulation parameters, the values from table 2.1 were used. We observed that the flagellum is deformed with increasing motor torques, but is never able to form a screw. The helix rotates at a higher angular velocity compared to the wild type and the forces pulling on the cell body are slightly increased. The critical motor torques M_{c1} and M_{c2} that mark the transition to unstable rotation and whirling motion for counter clockwise rotation are located at $M_{c1} = -2.04 pN\mu m$ and

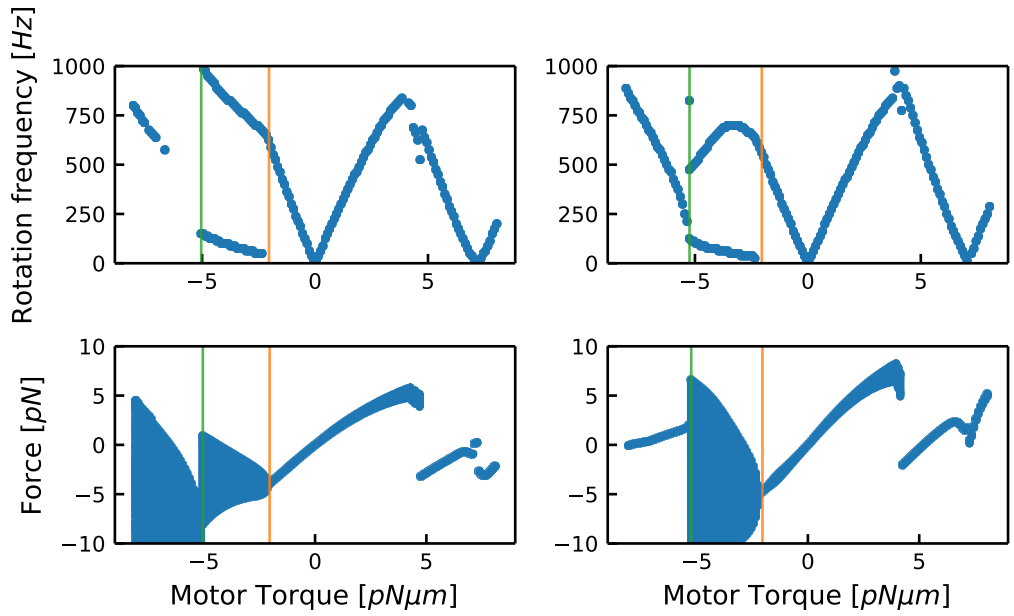

Fig. 2.13: Forces and frequencies for a flagellum composed of minor flagellin only after a simulation time of $T = 0.5s$. The hook friction coefficient is set to $\alpha_h = 0$ (left column) and $\alpha_h = 0.4$ (right column). The rotation frequency as a function of motor torque is displayed in the upper row and is in general higher than for the single-state major flagellin filament. For forward swimming motion, a second frequency appears in the spectrum below the critical motor torque $M_{c1} = -2.04pN\mu m$ for $\alpha_h = 0$ and $M_{c1} = -2.03pN\mu m$ for $\alpha_h = 0.4$. For stronger torques, the filament changes again to whirling motion, namely at $M_{c2} = -5.04pN\mu m$ and $M_{c2} = -5.24pN\mu m$. Positive motor torques lead to unstable motion with a sideway drift of the flagellum for $M_{c3} > 3.94pN\mu m$

$M_{c2} = -5.03pN\mu m$ for $\alpha_h = 0$ and $M_{c1} = -2.03pN\mu m$ and $M_{c2} = -5.24pN\mu m$ for $\alpha_h = 0.4$.

As in the major flagellin model, backward motion is unstable and the flagellum approaches a perpendicular orientation to the cell axis. Compared to the wild type, the effect is much more pronounced and the reorientation happens on shorter time scales. The drift is visible in the force diagram 2.13 for motor torques $M_0 > 3.94pN\mu m$ where both minimal and maximal force decrease with increasing torque. This is caused by a directional change of the force vector, so that now larger parts of the total force is transfered normal to the cell axis rather than parallel.

2.8.2 Simulation of an inhomogeneous flagellum

To understand why the flagellum of *S. Putrefaciens* and many other bacteria is composed of multiple flagellin types, the shape stability and the ability to form screws was studied for varying flagellar compositions. Starting with a flagellum composed of major flagellin only, the number of minor flagellin segments was gradually increased, beginning at the flagellar base. The stability and swimming efficiency of the resulting flagellum variants were studied for increasing motor torques with a fixed hook friction coefficient of $\alpha = 0.4$ by recording the elastic free energy and the force acting on the cell body. In addition, the transition

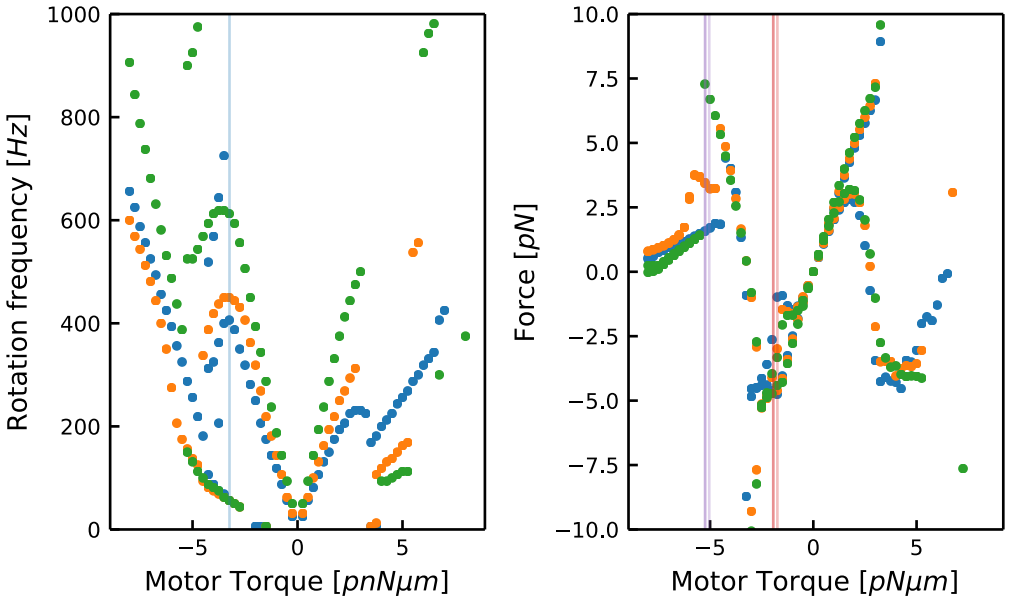

Fig. 2.14: Forces and frequencies for flagella with different compositions of minor and major flagellin after a simulation time of $T = 0.5s$. The hook friction coefficient is set to $\alpha_h = 0.4$. The rotation frequency (left) as a function of motor torque displays qualitatively similar behavior for all flagellar compositions with higher frequencies for increased numbers of minor flagellin. The force diagram (right) displays an early onset of stable buckling for $M_{c1} \approx -1pN\mu m$ for all filament variants. For stronger torques, the flagella change again to whirling motion, where the transition is shifted to stronger torques for increasing numbers of minor flagellin segments. For positive motor torques, the flagella drift sideways on undergo indirect screw formation for $M_{ci} > 3.9pN\mu m$. The onset of direct screw formation is observed for $M_{screw} > 6.3pN\mu m$ and depends on flagellar composition.

between the linear force regime and the dynamical shape change regime as well as the onset of screw formation is evaluated. Examining the force and frequency diagram (figure 2.14), it becomes clear that the inhomogeneity leads to an earlier onset of force oscillation for counter-clockwise rotation at a critical motor torque of $M_{c1} \approx -1pN\mu m$ for all observed filament variants. With an increasing number of minor flagellin segments, the onset of whirling motion moves to stronger motor torques and the rotation frequency increases. The effects of the unstable backward motion are amplified by the inhomogeneity as well, as indicated by the strong spread between minimum and maximum force for motor torques above $M_{c3} = 1.73pN\mu m$.

To further quantify the influence of the flagellar composition on the propulsion force, a number of simulations are carried out for a range of motor torques and combinations of FlaA and FlaB. The relation between propulsion force and motor torque is then approximated by a linear fit with the free parameter β_{eff} which is considered the propulsion efficiency for the given flagellar composition. The results are depicted in figure 2.15 and show an increase of the propulsion efficiency with the amount of FlaA in the flagellum. It is also important to note that the increase of β_{eff} with FlaA is not linear, but the largest gain in efficiency is between 0% and 25% FlaA. To understand how the second flagellin type changes the onset of screw formation, simulations with an increasing proportion of minor flagellin and a range of positive motor torques up to $8pN\mu m$ were performed. The radial distance from the cell

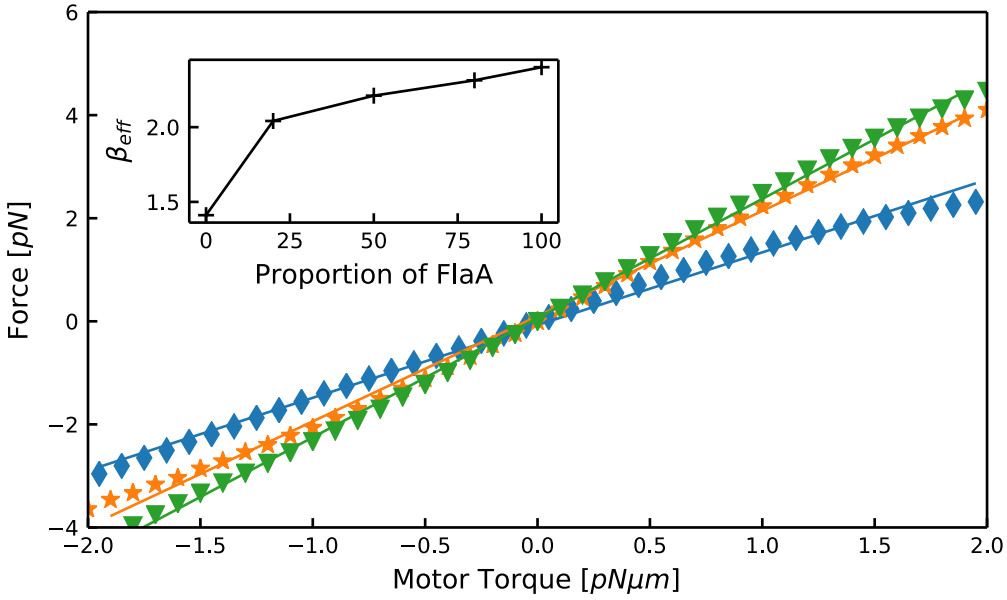

Fig. 2.15: Relation between motor torque and resulting force on the cell body. The slope of the linear fit is the propulsion efficiency β_{eff} shown in the inset for different motor torques.

axis of each segment was used in combination with the flagellum's free end position to track the screw formation process. As depicted in figure 2.16, direct screw formation is observable for strong motor torques above $M_{screw} > 6pN\mu m$ and a small amount of minor flagellin.

For longer simulation times, the number of screws increases due to the onset of indirect screw formation and even small motor torques are sufficient for screw formation. However, a high proportion of minor flagellin prevents the formation of screws, even when the flagellum reaches an almost perpendicular orientation to the cell body due to the drift.

We repeat these simulations for an inverted setup where the flagellum is composed of FlaA and segments are successively replaced by FlaB starting from the base. As depicted in figure 2.17, screw formation is only visible for a significant amount of FlaB in the flagellum. In contrast to the former setup, the motor torque required for screw formation decreases monotonically with increasing number of FlaB segments.

Combining these observations with the minor flagellin filament's increased propulsion efficiency offers an explanation for the presence of multiple flagellin variants within a single flagellum. While the minor flagellin filament offers an advantage for the free swimming cells, it prevents the formation of screws and the cell therefor have to maintain a high amount of major flagellin in their flagellum to be able to move efficiently in structured environments.

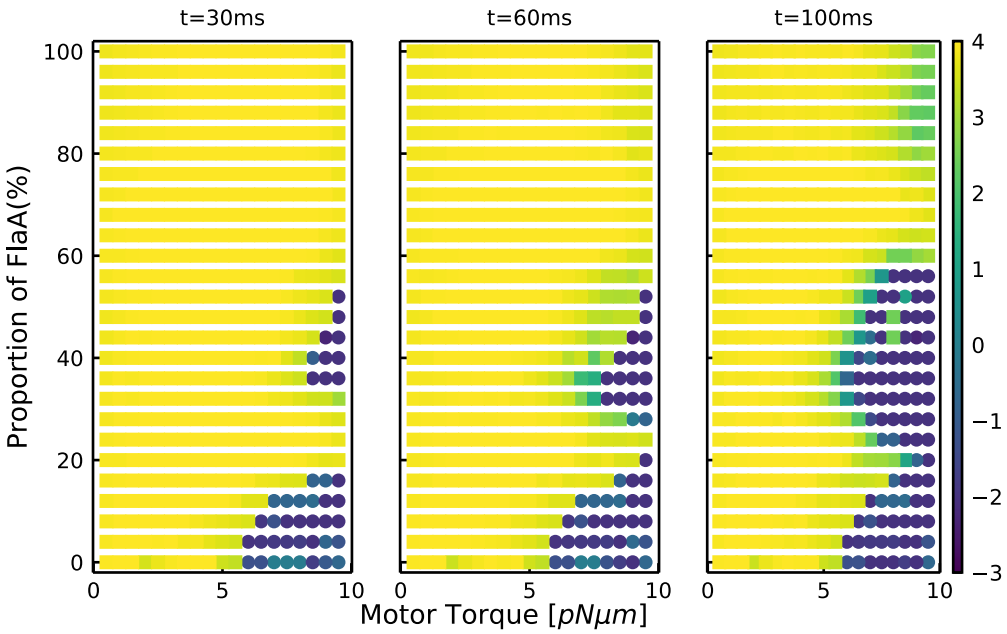

Fig. 2.16: Observation of screw formation for varying flagellin compositions after a simulation time of $T = 30ms$ (left), $T = 60ms$ (middle) and $T = 100ms$ (right). The simulations are run for flagella with an increasing number of FlaA segments, starting with a flagellum completely composed of FlaB and successively changing the segments to a FlaA configuration starting from the base. The z-position of the flagellum's free end is color coded to indicate an approach to the cell body, with negative values indicating a position below the motor segment. The formation of a screw is indicated by circular markers.

2.9 Conclusion

With the bacterial screw, a new type of locomotion mechanism has been discovered. It demonstrates a new kind of flagellar motion, in addition to the run-and-tumble mode known from *E. coli* and the reverse and flick mode previously described for monotrichous bacteria. As we have discussed, there are two paths to screw formation, of which only seems to be realized. Moreover, the assumption that screw formation is essential for survival in complex environments can motivate the presence of two kinds of flagellins in cells, since a suitable admixture of the two allows to achieve a mechanical state that is stable for forward propagation but still allows for screw formation for accessible reverse motor torque.

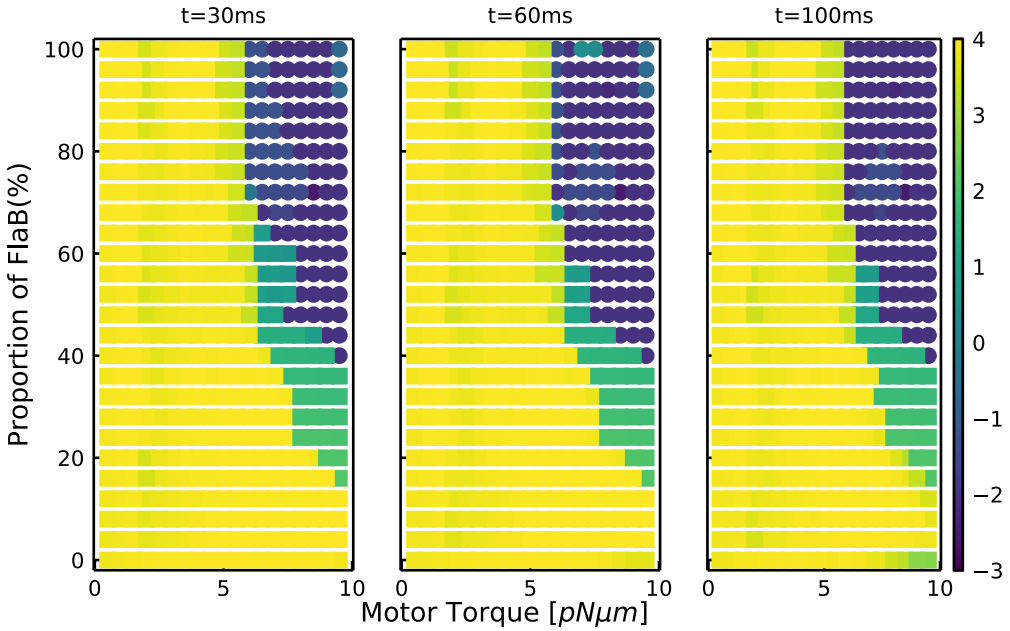

Fig. 2.17: Observation of screw formation for varying flagellin compositions for a simulation time of $T = 30ms$ (left), $T = 60ms$ (middle) and $T = 100ms$ (right). The simulations are run for flagella with an increasing number of major flagellin segments, starting with a flagellum completely composed of major flagellin and successively changing the segments to a minor flagellin configuration starting from the base. The z-position of the flagellum's free end is color coded to indicate an approach to the cell body, with negative values indicating a position below the motor segment. The formation of a screw is indicated by circular markers.

3 Enhanced diffusion

To maintain their metabolism, microorganisms depend on a constant uptake of nutrients. Over the course of evolution, they developed multiple strategies to ensure their access to new sources of food and to avoid unfavorable conditions. One of the most prominent mechanisms used by microorganisms is the ability to actively change their position by the means of different propulsion mechanisms such as cilia, pili or flagella Harshey, 2003. In addition, many organisms developed chemotaxis, i.e. the ability to follow changes in concentrations of specific molecules in their environment which enables them to search for locations with good growing conditions and to avoid unfavorable regions Berg and Brown, 1972; Macnab and Koshland, 1972; Adler, 1966. For most bacteria this search is a stochastic process, where periods of straight motion are followed by short reorientation phases. The ratio of the durations between these "run and tumble" phases are determined by the concentration of nutrients and thereby enable the organism to indirectly move toward regions with high concentrations of nutrients. During this motion, the organisms actively stir the surrounding medium, changing the position of molecules contained in the fluid. This phenomenon is known as biomixing and is the focus of current research. For example, several recent studies argue that biomixing might be an important mechanism in the mixing of the oceans Katija and Dabiri, 2009; Leshansky and Pismen, 2010; Dabiri, 2010. While this claim is still under discussion Visser, 2007; Kunze, 2011, the effects of biomixing have been observed for suspensions of microorganisms, causing enhanced diffusion of small tracer particles. These experiments lead to a number of theoretical studies.

The change in diffusive behavior was first observed by Wu and Libchaber Wu and Libchaber, 2000. They recorded tracer motion in a quasi two-dimensional soap film with fluorescent beads and swimming *E. coli* cells and noticed two different regimes in the mean square displacement. Follow-up experiments performed by Leptos et al Leptos et al., 2009, and Kurtuldu et al. Kurtuldu et al., 2011 measured the effects of different concentrations of swimmers on the probability density functions of the tracer displacements. They found the observed distributions to be non-Gaussian but also noted that they scaled with their standard deviation.

Different theoretical studies have been published to explain the enhance diffusivity and the non-Gaussian nature of tracer displacements. Based on the ideas of Katija and Dabiri Katija and Dabiri, 2009, Thiffeault and Childress argued that enhanced diffusion is caused by repeated swimmer-tracer interaction, leading to a series of tracer displacements Thiffeault and Childress, 2010. This idea was refined by Lin et al. Lin et al., 2011 to express the diffusivity in dependence of a swimmer's drift Maxwell, 1869; Darwin, 1953. Further extensions of this model include the presence of walls Miño et al., 2011, confined environments Yeomans et al., 2014 and curved swimmer trajectories Pushkin and Yeomans, 2013. Zaid et al. Zaid et al., 2011 studied regularized stresslet swimmers and were able to produce displacement distributions with non-Gaussian tails. Their work was further extended by

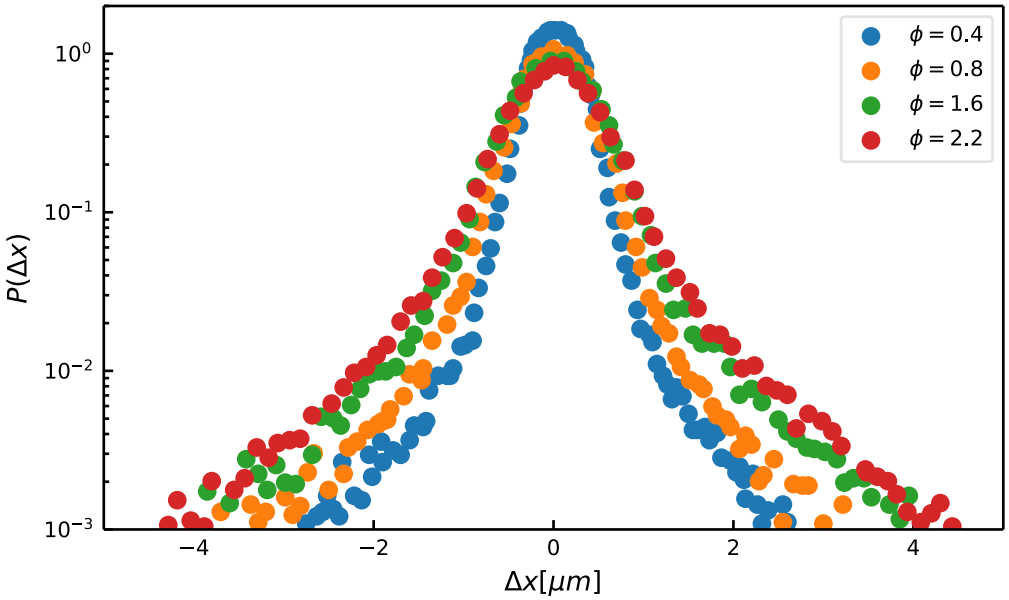

Fig. 3.1: Distribution of tracer displacements for different concentrations ϕ of the alga *Chlamydomonas reinhardtii*, measured by Leptos et al. Leptos et al., 2009

Pushkin and Yeomans to include confined environments Yeomans et al., 2014. A continuous time random walk (CTRW) model that is able to fit the distribution measured by Leptos et al. was developed by Eckhardt and Zammert, but requires a number of fitting parameters Eckhardt and Zammert, 2012.

Based on the aforementioned idea of repeated swimmer-tracer interactions, we construct a continuous time random walk model to explain the enhanced diffusivity as well as the non-Gaussian tracer displacement distributions. In addition, we compare our theoretical findings to results obtained from experiments with genetically modified bacteria and fluorescent beads. These genetic modification enable us to change the swimming patterns of the bacteria and to observe the corresponding effects on the tracer displacement.

3.1 Interaction of a bacterial swimmer with a tracer particle

We start our analysis by examining the interaction of a single swimmer with a tracer particle. On the length scales of microorganisms the flow field and hydrodynamic interactions can be approximated by the Stokes equation Purcell, 1977. To move through the surrounding fluid, a bacterium has to exert a force on the fluid, thereby generating a flow field. Since most of the relevant tracer particles are significantly smaller than the microswimmers, we assume that they behave like passive particles and instantly follow their surrounding flow field. As most swimming microorganisms have a spherical or cylindrical shape, their flow field is rotationally symmetric with respect to their swimming direction. Accordingly, we choose a cylindrical coordinate system $\boldsymbol{r} = (\rho, \theta, z)$ where the swimmer is moving along the z-axis.

The swimmer is set to travel at a fixed speed U, starting at position $\boldsymbol{r}_s(t=0) = (0, \theta_0, \lambda)$ while the tracer is placed at $\boldsymbol{r}_t(t=0) = (d, \theta_0, 0)$, where $\boldsymbol{r}_s(t)$ is the swimmer and $\boldsymbol{r}_t(t)$ the tracer position a time t. Since the tracer is passive and follows the flow field instantaneously, its dynamics is governed by the equations of motions

$$\dot{\boldsymbol{r}}_t = \boldsymbol{u}(\boldsymbol{r}_t(t), t), \tag{3.1}$$

where $\boldsymbol{u}(\boldsymbol{r}, t)$ is the flow field at position $\boldsymbol{r}$ and time t. The swimmer position is characterized by $\boldsymbol{r}_s(t) = U\boldsymbol{k}t + \boldsymbol{r}_{s,0}$, where the unit vector $\boldsymbol{k}$ defines the swimming direction and $\boldsymbol{r}_{s,0}$ is the swimmer's initial position. Using the fact that the flow field at $\boldsymbol{r}$ depends on the swimmer flow field $\boldsymbol{u}_s$ through $\boldsymbol{u}(\boldsymbol{r}, t) = \boldsymbol{u}_s(\boldsymbol{r} - \boldsymbol{r}_s(t), t)$ the equations of motion become

$$\dot{\boldsymbol{r}}_t = \boldsymbol{u}_s(\boldsymbol{r} - (U\boldsymbol{k}t + \boldsymbol{r}_{s,0}), t) \tag{3.2}$$

In order to continue our analysis and to understand the effects of a single tracer-swimmer interaction, we need to specify the flow field $\boldsymbol{u}_s$ generated by our model swimmer and solve equation (3.2).

3.1.1 Flow field model

One of the simplest models to represent a microswimmer's flow field is a multipole expansion. The leading order term is the so called "Stokeslet" or Oseen tensor $\mathrm{J}(\boldsymbol{r})$, which corresponds to a point force acting on the fluid and is given by

$$\mathrm{J}(\boldsymbol{r}) = \frac{1}{8\mu\pi}\left(\frac{\mathrm{I}}{r} + \frac{\boldsymbol{r}\boldsymbol{r}}{r^3}\right), \tag{3.3}$$

where μ is the dynamic viscosity. Due to their small size, the effect of gravity acting on a micro-swimmer can be neglected and the swimmer is basically force free. Consequently, the Stokeslet term vanishes and only higher order terms have to be taken into account. This is in agreement with experiments performed by Drescher et al. Drescher et al., 2010; Drescher et al., 2011, which demonstrated that the far field of swimming *E. coli* cells and micro algae *Volvox* is approximated by a dipole field. A corresponding flow field model for the far field of dipolar swimmers used in recent studies by Pushkin and Yeomans Pushkin et al., 2013; Pushkin and Yeomans, 2013 is the stresslet:

$$\boldsymbol{u}_s \approx -a_s\boldsymbol{k}\cdot(\boldsymbol{k}\cdot\nabla)\mathrm{J}(\boldsymbol{r}), \tag{3.4}$$

where a_s is the dipole strength and $\boldsymbol{k}$ is again a unit vector defining the swimming direction. Although the stresslet is a good model for the swimmer's far field and allows some analytic approximations for the tracer displacement Pushkin et al., 2013, it becomes singular for small swimmer tracer distances as it does not account for the finite swimmer size. To overcome this limitation, our simulations are based on the squirmer model introduced by Lighthill in 1952 Lighthill, 1952. He developed the model to explain how a sphere can swim at very low Reynolds numbers by oscillatory shape changes. The model was later extended and used to model swimming microorganisms like *Paramecium* Blake, 1971 or artificial microswimmers for example Janus particles Bickel et al., 2013. In the following text we assume a swimmer

of fixed radius a, moving with a constant speed U in the direction defined by $\boldsymbol{k}$. The flow field of the swimmer in the lab frame with $\boldsymbol{u}(\boldsymbol{r} \to \infty) = \boldsymbol{0}$ is given by

$$\begin{aligned}\boldsymbol{u}_s(\boldsymbol{r}) = B_1 \left(\frac{a}{r}\right)^3 \left(\frac{\boldsymbol{k}\cdot\boldsymbol{r}}{r}\frac{\boldsymbol{r}}{r} - \frac{\boldsymbol{k}}{3}\right) + \sum_{n=2}^{\infty}\left(\frac{a^{n+2}}{r^{n+2}} - \frac{a^n}{r^n}\right) B_n P_n\left(\frac{\boldsymbol{k}\cdot\boldsymbol{r}}{r}\right)\frac{\boldsymbol{r}}{r} \\ + \sum_{n=2}^{\infty}\left(\frac{n}{2}\frac{a^{n+2}}{r^{n+2}} - \left(\frac{n}{2}-1\right)\frac{a^n}{r^n}\right) B_n W_n\left(\frac{\boldsymbol{k}\cdot\boldsymbol{r}}{r}\right)\left(\frac{\boldsymbol{k}\cdot\boldsymbol{r}}{r}\frac{\boldsymbol{r}}{r} - \boldsymbol{k}\right),\end{aligned} \tag{3.5}$$

where P_n are Legendre polynomials, B_n are constants and W_n is defined by

$$W_n(x) = \frac{2}{n(n+1)} P_n'(x). \tag{3.6}$$

We truncate the series at $n = 2$ and note that due to the constant B_1 is related to the swimmers velocity by $U = 2B_1/3$. In addition, we introduce the squirmer parameter $\beta = B_2/|B_1|$ and divide the flow field by U, $\hat{\boldsymbol{u}} = \boldsymbol{u}/U$, to arrive at the expression

$$\begin{aligned}\hat{\boldsymbol{u}}_s(\boldsymbol{r}) = \frac{3}{2}\left(\frac{a}{r}\right)^3 \left(\frac{\boldsymbol{k}\cdot\boldsymbol{r}}{r}\frac{\boldsymbol{r}}{r} - \frac{\boldsymbol{k}}{3}\right) + \frac{\beta}{3}\left(\frac{a^4}{r^4} - \frac{a^2}{r^2}\right)\left(3\left(\frac{\boldsymbol{k}\cdot\boldsymbol{r}}{r}\right)^2 - 1\right)\frac{\boldsymbol{r}}{r} \\ + \frac{2}{3}\beta\left(\frac{a}{r}\right)^4 \left(\frac{\boldsymbol{k}\cdot\boldsymbol{r}}{r}\right)\left(\frac{\boldsymbol{k}\cdot\boldsymbol{r}}{r}\frac{\boldsymbol{r}}{r} - \boldsymbol{k}\right)\end{aligned} \tag{3.7}$$

for the flow field. By setting the squirmer parameter to $\beta < 0$, the swimmer becomes a pusher, i.e. the motor force pushes the swimmer on the rear side and is countered by the drag force acting on the cell body. Typical examples for the pusher model are polyflagelated bacteria like *E. coli*. A squirmer with $\beta > 0$ is a puller - the motor is located at the front side of the body and pulls it, as in the case of the microalgae *Chlamydomonas reinhardtii* which is driven by two flagella performing a synchronized beating motion. The flow field of neutral swimmers like the ciliated *Paramecium* correspond to $\beta = 0$. For this case, the far field decays as $\hat{\boldsymbol{u}}_s(\boldsymbol{r}) \propto r^{-3}$, while the flow field decreases as $\hat{\boldsymbol{u}}_s(\boldsymbol{r}) \propto r^{-2}$ for the pusher and puller case.

To nondimensionalize the equations of motions we choose the swimmer radius as the characteristic length scale ($\boldsymbol{r} = a\hat{\boldsymbol{r}}$) and rescale time by $t = a/U\hat{t}$, resulting in the equation

$$\frac{\partial \hat{\boldsymbol{r}}}{\partial \hat{t}} = \hat{\boldsymbol{u}}_s(a(\hat{\boldsymbol{r}} - (\boldsymbol{k}\hat{t} + \hat{\boldsymbol{r}}_0^s)). \tag{3.8}$$

3.1.2 Tracer displacement and interaction time

In order to develop a continuous time random walk model that catches the microscopic details of swimmer-tracer interactions and successfully predicts the experimental results, it is necessary to understand the characteristic features of a single swimmer-tracer interaction first. One can assume that for a dilute swimmer suspensions, the tracer's motion is dominated by the presence of a single swimmer during each interaction. The tracer follows the swimmer's flow field and experiences a displacement $\Delta r = |\boldsymbol{r}_t(t_{end}) - \boldsymbol{r}_t(t_{start})|$ at the end of the interaction. Since the displacement does not happen instantly but depends on different

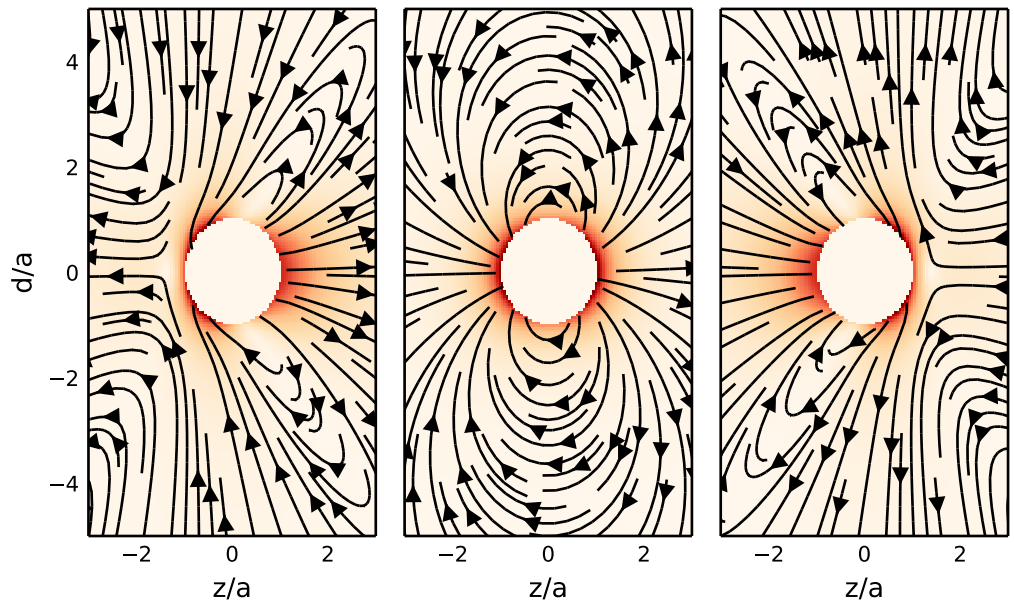

Fig. 3.2: Flow field generated by the squirmer model (3.7) for a swimmer moving along the z-axis. The left column shows a pusher with the squirmer parameter $\beta = -1$ and the right column a puller $\beta = 1$. For $\beta = 0.$, the flow field corresponds to a neutral swimmer (middle)

parameters like the swimmer speed, the impact parameter and the flow field strength, it is necessary to introduce an interaction time T - the time a tracer feels the swimmers influence. A third feature of interest is the mean tracer velocity, representing the relation between displacement and interaction time. We start our investigations by considering the ideal case of a swimmer traveling with speed U in a straight line from $z = -\infty$ to $z = \infty$ and a tracer placed at $\boldsymbol{r}_t = (d, 0, 0)$. Since it is not possible to solve equation (3.2) analytically we have to resort to numerical integration. As the flow field rapidly decays with increasing r, we define a sphere of influence R around the swimmer in which its flow field is strong enough to have a detectable effect on the tracer. Outside this sphere we neglect the flow field and have to solve the equation of motion only for swimmer tracer distances smaller than R. To study the tracer displacements Δ_r, we place the swimmer at $z = -D$, so that the tracer is just outside of sphere of influence and integrate the equations of motion until the tracer leaves the sphere again. To choose R, we select a minimal flow field strength of $u_{min} = 10^{-5}$ and calculate the corresponding R along the swimming direction $\boldsymbol{k}$. As indicated by figure 3.3, we find that the dependence of the displacement Δr on the impact parameter b can be split into two regimes. For an impact parameter smaller than the swimmer radius a, the displacement depends logarithmically on d, whereas if d exceeds the swimmer radius a, the dependence follows a power law:

$$\Delta r = \begin{cases} p_1 \log(p_2/d), & \text{if } d \leq a \\ p d^{-3}, & \text{if } d > a,\ \beta = 0 \\ p d^{-2}, & \text{if } d > a,\ \beta \neq 0 \end{cases} \tag{3.9}$$

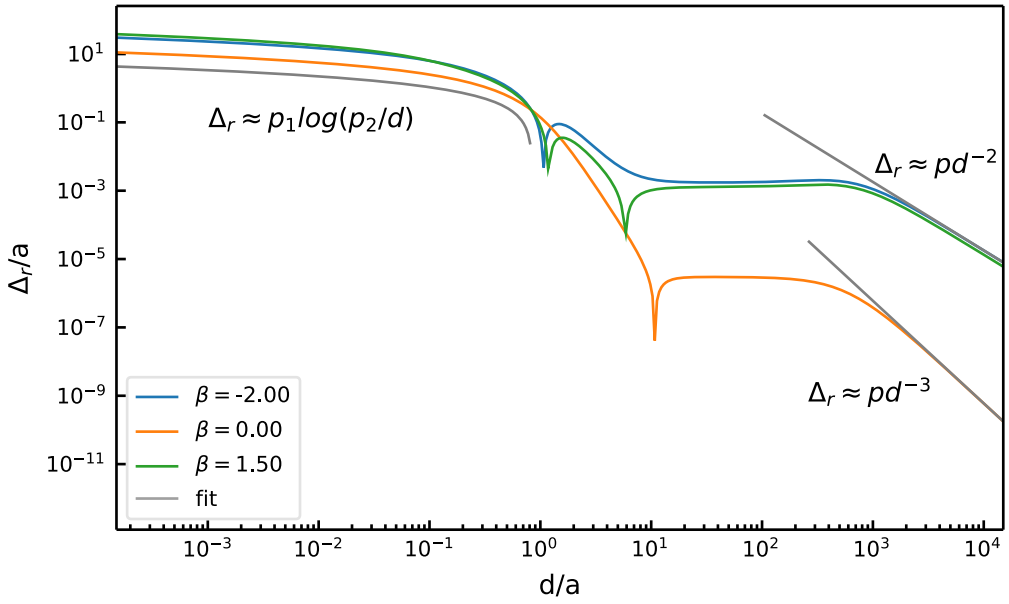

Fig. 3.3: Tracer displacement Δ_r for swimming squirmer with an infinite swimming path and a radius of a and different squirmer parameters β. For small impact parameters $d < a$, the displacement decreases logarithmically with d, while for $d > a$, the data is fitted by $\Delta r \approx d^{-3}$ and $\Delta r \approx d^{-2}$ for $\beta = 0$ resp. $\beta \neq 0$.

These results are similar to the ones presented by Thiffeault and Childress Thiffeault and Childress, 2010 who used a different flow field model but arrived at similar results.

Since most microswimmers have a finite swimming length λ, it is necessary to refine the previous results to include the effects of incomplete interactions. To achieve this, we repeat the previous simulations, but instead of defining a sphere of influence, we place the swimmer at the origin and place our tracer particles at $r_t = (d, 0, l)$. Starting from the origin the swimmer travels distance λ and the values of the initial tracer location on the z-axis l range from $l = -2\lambda$ to 3λ. The resulting displacements are displayed in figure 3.4. For large swimming lengths $\lambda > 50a$, the displacements are dominated by tracers initially placed along the swimmer's path and follow a similar pattern as for the infinite swimmer - logarithmically increasing up to a maximal displacement close to $\Delta_r = \lambda$. For smaller swimming lengths, the influence of regions close to the starting and final swimmer position become more important. While the tracer trajectories along the swimmer's path form nearly closed loops, the trajectories in the former regions remain incomplete, displaying significant displacements.

Assuming that the swimmers are isotropically distributed in the medium and show no privileged direction of motion, the probability for an interaction to occur with impact parameter l is uniformly distributed with $p(l) = 1/(l_{max} - l_{min}) = 1/7\lambda$. In order to calculate the effective displacements with respect to d, we numerically average over l. The results are presented in figure 3.5. Even for small swimming lengths, the displacements increase logarithmically with d^{-1}, especially for small values of β. This observation justifies the use of the simple model with $\lambda = \infty$ in the following calculations.

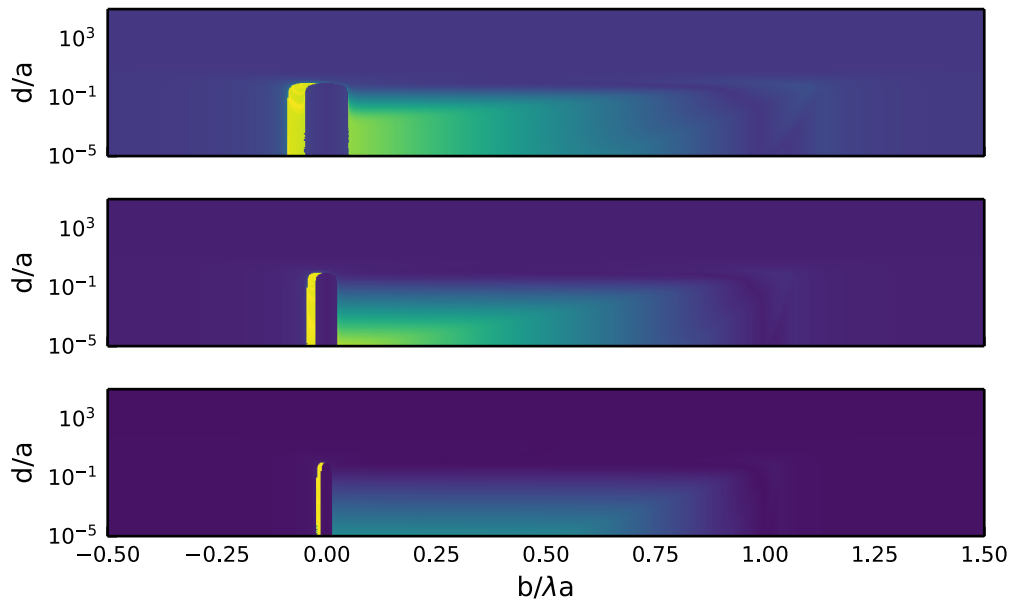

Fig. 3.4: Tracer displacement Δ_r for a squirmer with a finite swimming path λ. The path length in the upper image is set to $\lambda = 20a$, to $\lambda = 50a$ in the second image and $\lambda = 100a$ in the lower image.

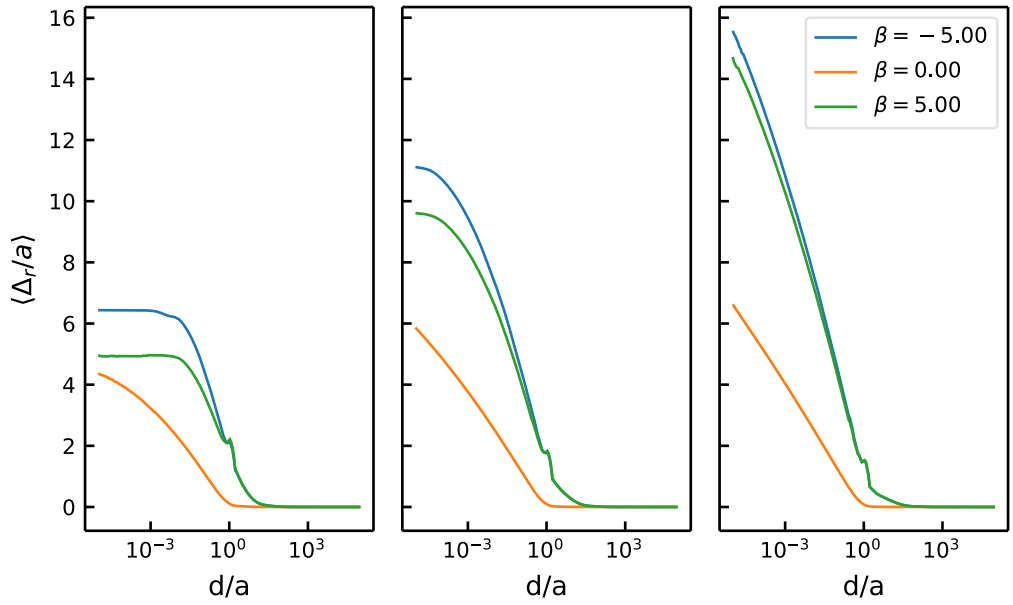

Fig. 3.5: Mean tracer displacement $\langle\Delta_r\rangle$ for squirmers with different swimming distances λ and flow field parameters β. In the left, middle and right plot the swimming distances were set to $\lambda = 20a$, $\lambda = 40a$ and $\lambda = 80a$ respectively. The flow field parameters were set to $\beta = -5$ (blue), $\beta = 0$ (orange) and $\beta = 5$ (green). The mean displacement is calculated over the z-component of all starting configurations $\boldsymbol{r}_{t,0}$

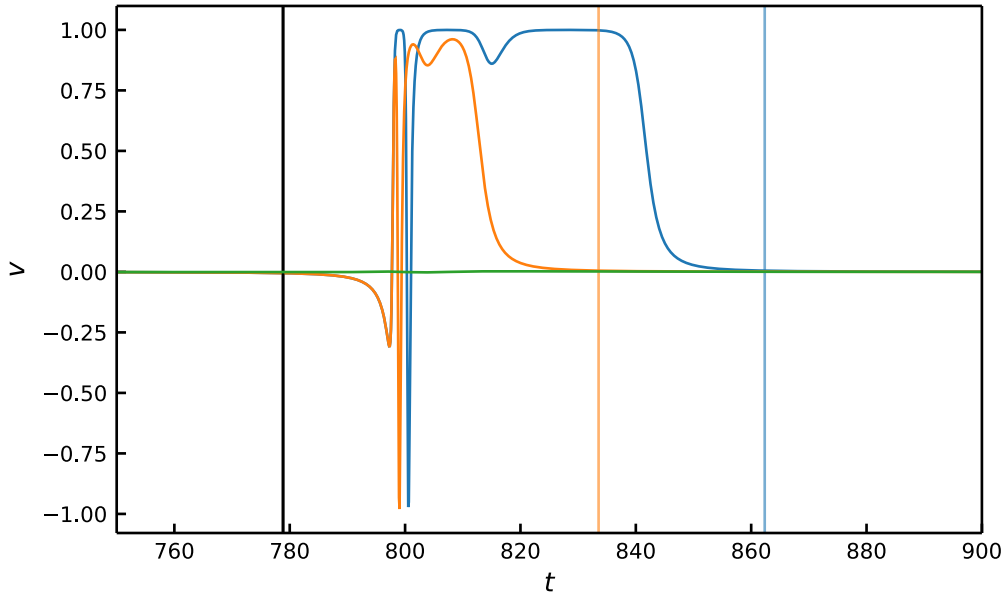

Fig. 3.6: Instantaneous tracer velocity during a swimmer-tracer interaction for different impact parameters d. The vertical lines mark the timepoints at which the tracer enters respectively leaves the swimmer's sphere of influence. The impact parameters are $d = 10^{-3}a$ (blue), $d = 2 \cdot 10^{-3}a$ (green) and $d = 3 \cdot 10^{-3}a$ (orange).

To calculate the interaction time, we again place the swimmer just outside the sphere of influence and integrate the equations of motion until the swimmers leaves the sphere of influence. We define the interaction time T as the time a tracer spends inside this sphere. As depicted in figure 3.7 we find that T depends on b in the same functional relationship as Δr, namely

$$T \approx \begin{cases} \log(p_T/d), & \text{if } d \leq a \\ d^{-3}, & \text{if } d > a,\ \beta = 0 \\ d^{-2}, & \text{if } d > a,\ \beta \neq 0. \end{cases} \tag{3.10}$$

3.1.3 Mean displacement velocity

As shown in figure 3.6 the instantaneous velocities of the tracer changes during the course of each interaction. For smaller impact parameters the tracer moves with a velocity close to the swimmer velocity v_0 for an increasing amount of time. In order to further characterize the individual swimmer-tracer encounters, we introduce the mean tracer velocity as tracer displacement per interaction time

$$v_\Delta = \frac{\Delta r}{T}. \tag{3.11}$$

By combining the previous results, we observe a linear relation between Δr and T (figure 3.7) and thereby assume a constant displacement velocity for impact parameters with notable displacements.

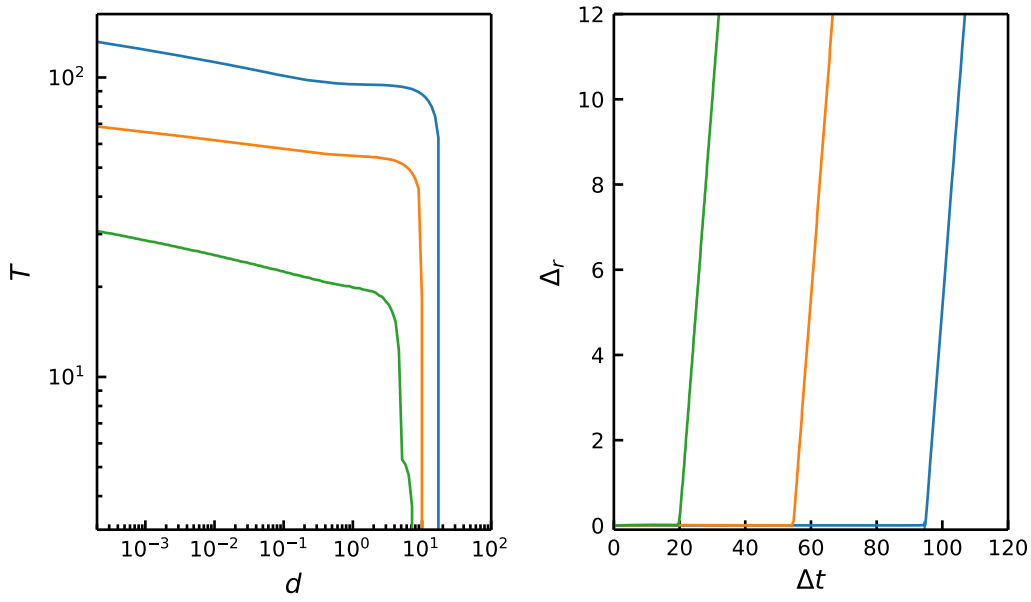

Fig. 3.7: Tracer interaction time T in dependence of impact parameter d (left) for different flow field parameters $\beta = 1.5$ (blue), $\beta = -0.5$ (orange) and $\beta = 0$ (green). Total tracer displacement Δ_r versus interaction time T (right). The displacement grows linearly with T for small impact parameters d, leading to a constant mean velocity $v_\Delta = \Delta_r/T$. For $d \geq a$ the displacements decreases as a power-law and the tracer trajectories form almost closed loops. The interaction time includes the complete trajectories and therefore decreases slower than the displacement, leading to negligible mean velocities.

3.1.4 Sequential interaction model

Summarizing the previous results, we model the tracer motion as a sequence of steps caused by individual tracer-swimmer interactions. During each step, the tracer moves with a constant velocity $\boldsymbol{v_{tr}}$ and the step distance as well as the step duration is completely characterized by the impact parameter d. The orientation of displacements depends on the swimming direction $\boldsymbol{k}$ and is thereby isotropically distributed. As in the previous section, we assume a dilute swimmer suspension so that the tracer does not interact with more than one swimmer at any time. A second assumption is, that the swimmers are distributed isotropically in the medium with random orientations. To obtain a probability density distribution of step sizes and step durations from the previously observed interaction details, we first need to specify the distribution of impact parameter d. The functional form of $p(d)$ depends on the dimensionality of our problem.

In the simplest version, i.e. the pseudo one dimensional case, the swimmer is restricted to move in the z-direction only, either starting at $z = -\infty$ with velocity $+U$ or starting at $z = \infty$ with velocity $-U$. Due to the flow field's vanishing θ-component, a tracer initially placed in the ρ-z-plane remains in this plane for all times. Although this scenario does not directly reflect experimental observations, it proves useful for the understanding of the process. Since a swimmer does not affect the tracer unless it enters its circle of influence

R_i, d is limited to $0 < d < R_i$. Hence, for the pseudo one-dimensional case d is distributed uniformly on this interval,

$$p_{1\mathrm{D}}(d) = 1/R_i. \tag{3.12}$$

In the two-dimensional case, the swimmers are allowed to assume any swimming direction in the x-z-plane. Since the starting points and the velocities are uniformly distributed, the distribution of d is also uniform,

$$p_{2\mathrm{D}}(d) = 1/R_i. \tag{3.13}$$

In the three-dimensional case, $p(d)$ is no longer uniform but increases linearly with d,

$$p_{3\mathrm{D}}(d) = 2d/R_i^2. \tag{3.14}$$

From these distributions, we can derive the distribution of interaction times $p(T)$ by a change of variables, using the relation $g_T(d) = k_t \log(c_t/d)$ from equation (3.10). Since $T(d)$ decreases monotonically with d, $p(T)$ is obtained by

$$p(T) = \left| \frac{d}{dT} g_T^{-1}(T) \right| p_{\mathrm{nD}}(g_T^{-1}(T)) \tag{3.15}$$

with $g_T^{-1}(T) = c_t \exp(-T/k_t)$ and we arrive at two-dimensional interaction time distribution

$$p_{2\mathrm{D}}(T) = \frac{1}{R_i} \frac{c_t}{k_t} e^{-T/k_t} \tag{3.16}$$

Since the displacements and interactions times are dominated by head-on collisions, we limit the radius of the interaction sphere to the range of d where $g_T > 0$ and hence choose $R_i = c_r$. As a result, $p_{2\mathrm{D}}(T)$ is reduced to the exponential distribution

$$p_{2\mathrm{D}}(T) = \frac{1}{k_t} e^{-T/k_t} \tag{3.17}$$

By making the same assumptions, the waiting time distribution for the three-dimensional case is found to be

$$p_{2\mathrm{D}}(T) = \frac{2}{k_t} e^{-2T/k_t} = \frac{1}{\tilde{k}_t} e^{-T/\tilde{k}_t} \tag{3.18}$$

with $\tilde{k}_t = k_t/2$.

3.2 Calculation of $P(x, t)$

In order to understand how an initial distribution of tracer particles evolves over time, we construct the transport equations for a continuous time random walk. The properties of this CTRW are based on the conclusions drawn in the previous section, namely a constant velocity during the steps and an exponentially distributed interaction time. Since the resulting process depends on the dimensionality of the problem, we first define the transport equation for the generic N-dimensional case and then discuss the specific results for the one, two and three-dimensional situation.

3.2.1 Transport equations

The probability to find a particle at position $\boldsymbol{r}$ and time t is given by

$$P(\boldsymbol{r},t) = \int_{\infty}^{\infty}\int_{0}^{t} \nu(\boldsymbol{r}-\boldsymbol{v}\tau, t-\tau)\Psi(\tau)h(\boldsymbol{v})d\tau d\boldsymbol{v}, \tag{3.19}$$

where $h(\boldsymbol{v})$ is the probability distribution of the step-velocities. $\nu(\boldsymbol{r},t)$ is the probability that a particle finishes its step and changes its velocity at point $\boldsymbol{r}$ and time t. The duration of the individual steps is distributed according to $\psi(t)$, while $\Psi(t) = 1 - \int_0^t \psi(\tau)d\tau$ describes the probability of not completing a step until time t. The probability $\nu(\boldsymbol{r},t)$ of velocity changes due to completion of a step is calculated by integrating over all previous times and positions $\boldsymbol{v}\tau$ where a particle might have started its walk,

$$\nu(\boldsymbol{r},t) = \int\int_{0}^{t} \nu(\boldsymbol{r}-\boldsymbol{v}\tau, t-\tau)\psi(\tau)h(\boldsymbol{v})d\tau d\boldsymbol{v} + \delta(t)P_0(\boldsymbol{r}), \tag{3.20}$$

where $P_0(\boldsymbol{r})$ is the initial probability to find a particle at position $\boldsymbol{r}$. The integral over $d\boldsymbol{v}$ is taken over complete three dimensional velocity space. To solve these equations we apply a combination of Fourier and Laplace transforms where we use $\boldsymbol{k}$ and s to denote coordinates in the Fourier and Laplace space respectively. Starting with the Fourier transform $f(\boldsymbol{k}) = \int f(\boldsymbol{r})e^{-i\boldsymbol{k}\boldsymbol{r}}d\boldsymbol{r}$ of $\nu(\boldsymbol{r},t)$, we arrive at

$$\nu(\boldsymbol{k},t) = \int\int_{0}^{t} \psi(\tau)h(v)\mathscr{F}\left[\nu(\boldsymbol{r}-\boldsymbol{v}\tau, t-\tau)\right]d\tau d\boldsymbol{v} + \delta(t)P_0(\boldsymbol{k}). \tag{3.21}$$

Using the shift property of the Fourier transform $\mathscr{F}\left[f(x+a)\right] = \mathscr{F}\left[f(x)\right]e^{+iak}$ the expression simplifies to

$$\nu(\boldsymbol{k},t) = \int\int_{0}^{t} \psi(\tau)h(\boldsymbol{v})e^{-i\tau\boldsymbol{v}\boldsymbol{k}}\nu(\boldsymbol{k},t-\tau)d\tau d\boldsymbol{v} + \delta(t)P_0(\boldsymbol{k}). \tag{3.22}$$

By taking the Laplace transform $f(\boldsymbol{s}) = \int_0^\infty f(t)e^{-st}dt$ of $\nu(\boldsymbol{k},t)$ and using its convolution and shift property $\mathscr{L}\left[e^{at}f(t)\right] = \hat{f}(s-a)$, we arrive at

$$\begin{aligned}
\nu(\boldsymbol{k},s) &= \int h(\boldsymbol{v})\mathscr{L}\left[\int_0^t d\tau\psi(\tau)\nu(\boldsymbol{k},t-\tau)e^{-i\boldsymbol{k}\boldsymbol{v}\tau}\right]_s d\boldsymbol{v} + P_0(\boldsymbol{k}) && (3.23)\\
&= \int h(\boldsymbol{v})\mathscr{L}\left[\psi(t)e^{-i\boldsymbol{k}\boldsymbol{v}t}\right]_s \nu(\boldsymbol{k},s)d\boldsymbol{v} + P_0(\boldsymbol{k}) && (3.24)\\
&= \nu(\boldsymbol{k},s)\int h(\boldsymbol{v})\psi(s+i\boldsymbol{k}\boldsymbol{v})d\boldsymbol{v} + P_0(\boldsymbol{k}), && (3.25)
\end{aligned}$$

so that

$$\nu(\boldsymbol{k},s) = \frac{P_0(\boldsymbol{k})}{1-\int h(\boldsymbol{v})\psi(s+i\boldsymbol{k}\boldsymbol{v})d\boldsymbol{v}}. \tag{3.26}$$

Repeating the above steps for $P(\boldsymbol{r},t)$ yields

$$P(\boldsymbol{k},s) = \nu(\boldsymbol{k},s)\int h(\boldsymbol{v})\Psi(s+i\boldsymbol{k}\boldsymbol{v})d\boldsymbol{v} \tag{3.27}$$

By combining this results with (3.26), we can express the transport equation 3.19 as

$$P(\boldsymbol{k}, s) = P_0(\boldsymbol{k}) \frac{\int h(\boldsymbol{v}) \Psi(s + i\boldsymbol{k}\boldsymbol{v}) d\boldsymbol{v}}{1 - \int h(\boldsymbol{v}) \psi(s + i\boldsymbol{k}\boldsymbol{v}) d\boldsymbol{v}}. \tag{3.28}$$

The difficulty of obtaining $P(\boldsymbol{r}, t)$ from this expression lies in the computation of the inverse Fourier-Laplace-transform. Nevertheless, equation (3.28) allows us to derive arbitrary moments of $P(\boldsymbol{r}, t)$ using

$$\langle \boldsymbol{r}^n \rangle = (-i)^n \nabla^n_{\boldsymbol{k}} P(\boldsymbol{k}, t)|_{\boldsymbol{k}=0}. \tag{3.29}$$

As demonstrated in the previous section, numerical simulations of tracer-swimmer interactions suggest a logarithmic relation between impact parameter and interaction time. For an isotropic distribution of swimmers, this leads to an exponential waiting time distribution in the CTRW model,

$$\psi(t) = \lambda e^{-\lambda t} \tag{3.30}$$

and a survival probability of

$$\Psi(t) = 1 - \int_0^t \psi(\tau) d\tau = e^{-\lambda t}, \tag{3.31}$$

where the rate parameter λ is defined in section 3.1.4 depends on the flow field model and the dimensionality of the system. Laplace transforming $\psi(t)$ and $\Psi(t)$ yields

$$\psi(s) = \frac{\lambda}{s + \lambda}, \tag{3.32}$$

$$\Psi(s) = \frac{1}{s + \lambda}. \tag{3.33}$$

3.2.2 Constant velocity distribution

Due to the properties of the examined tracer-swimmer interaction process, we focus exclusively on isotropic velocity distributions which depend on $|\boldsymbol{v}| = v$ only, i.e. $h(\boldsymbol{v}) = h(v)$. Motivated by our findings in section 3.1.3, we further assume a constant velocity v_0 during all steps. The explicit form of $h(v)$ depends on the system's dimensionality.

In the one-dimensional case, the tracer is restricted to either move to the left or to the right and consequently $h(v)$ is given by

$$h(v) = \frac{1}{2} \left[\delta(v - v_0) + \delta(v + v_0) \right]. \tag{3.34}$$

Inserting these results in equation (3.28), we arrive at

$$P(k, s) = \frac{\left[\Psi(s + ikv_0) + \Psi(s - ikv_0) \right]}{2 - \left[\psi(s + ikv_0) + \psi(s - ikv_0) \right]} P_0(k). \tag{3.35}$$

Upon introduction of the exponential waiting time distributions this reduces to

$$\psi(s+ikv_0)+\psi(s-ikv_0)=\frac{\lambda}{s-ikv_0+\lambda}+\frac{\lambda}{s+ikv_0+\lambda}=\frac{\lambda\,(s+\lambda)}{(s+\lambda)^2+k^2v_0^2} \tag{3.36}$$

$$\Psi(s+ikv_0)+\Psi(s-ikv_0)=\frac{1}{s-ikv_0+\lambda}+\frac{1}{s+ikv_0+\lambda}=\frac{s+\lambda}{(s+\lambda)^2+k^2v_0^2} \tag{3.37}$$

and therefore,

$$P(k,s)=\frac{\lambda+s}{s\,(\lambda+s)+k^2v^2}P_0(k) \tag{3.38}$$

We use this result to calculate the mean squared displacement by means of equation (3.29). In a first step, we take the second derivative of equation (3.38) with respect to k and evaluate the result at $k=0$,

$$\frac{d^2}{dk^2}p(k,t)|_{k=0}=\frac{2v_0^2}{s^2(s+\lambda)}. \tag{3.39}$$

By computing the inverse Laplace transform of this expression we arrive at

$$\langle r^2\rangle=\frac{2v_0^2}{\lambda^2}\left(e^{-\lambda t}+\lambda t-1\right). \tag{3.40}$$

Obviously, for large t, $\langle r^2\rangle$ approaches diffusive scaling $\langle r^2\rangle=2Dt$ with $D=v_0^2/\lambda$. By using the Taylor expansion $e^{-\lambda t}=1-\lambda t+\lambda^2t^2/2+O(t^3)$, we find that for small times t, $\langle r^2\rangle$ scales balistically $\langle r^2\rangle\approx v_0^2t^2$.

Remarkably, equation (3.38) is one of the few cases where an analytical expression of the inverse Laplace-Fourier of $p(k,s)$ is known Goldstein, 1951. As it turns out, equation (3.38) is the free space Green's function of the telegrapher's equation Masoliver et al., 1993,

$$D\frac{\partial^2P}{\partial r^2}=\frac{\partial P}{\partial t}+\lambda\frac{\partial^2P}{\partial t^2}, \tag{3.41}$$

where $D=r_0^2/\lambda$ is the diffusion constant. The solution of this differential equation which is equal to the inverse of (3.38) was published by Goldstein Goldstein, 1951 and reads

$$\begin{aligned}P(r,t)=&\,1/2e^{-\lambda t/2}\left[\delta(r-r_0-v_0t)+\delta(r-r_0+v_0t)\right]\\&+\frac{\lambda e^{-\lambda t/2}}{4v_0}\left[I_0(\chi)+\frac{\lambda t}{2\chi}I_1(\chi)\right]H(v_0t-|r-r_0|)\end{aligned} \tag{3.42}$$

with $\chi=\lambda\sqrt{v_0^2t^2-(r-r_0)^2}/2v_0$. Here $H(x)$ denotes the Heaviside step functions, whereas I_0 and I_1 are modified Bessel functions of the first kind. As shown in figure 3.8, all tracer particles are located between the ballistic fronts. These fronts travel with speed v_0 and decay exponentially with $P_{front}\approx e^{-\lambda t/2}$. To study the asymptotic behavior of distribution (3.42), we calculate the Taylor expansion of χ at r_0 up to the second order and find

$$\chi(r,t)=\frac{\lambda t}{2}\left(1-\frac{(r-r_0)^2}{2v_0^2t^2}\right)+O(r-r_0)^3. \tag{3.43}$$

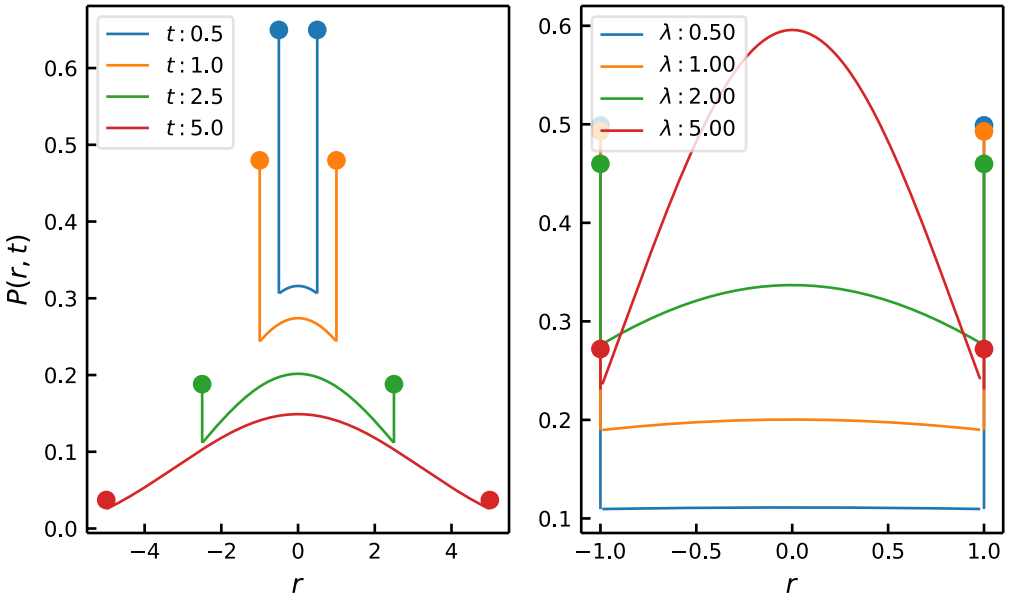

Fig. 3.8: Probability density function for a Levy walk with an exponential waiting time distribution for a fixed interaction rate $\lambda = 1.5$ (left), the exponential decay of the traveling front is clearly visible. In the right image, the probability density functions for a fixed time $t = 1$ and varying interaction rates λ are shown.

Hence, for large t and $r \approx r_0$, χ increases almost linearly with t as $\chi \approx \lambda t/2$. Using the relation

$$I_n(\chi) \overset{\chi\to\infty}{\approx} \frac{1}{\sqrt{2\pi\chi}} e^{\chi} \tag{3.44}$$

as given in Wolf, 2013, we can rewrite equation (3.42) as

$$P(r, t_\infty) = \frac{\lambda}{4v_0} e^{-\lambda t/2} \frac{1}{\sqrt{2\pi\chi}} e^{\chi} \left(1 + \frac{\lambda t}{2\chi}\right). \tag{3.45}$$

Substituting χ by its Taylor expanded form (3.43) yields

$$P(r, t_\infty) = \frac{1}{2\sqrt{4\pi \frac{v_0^2}{\lambda} t \left(1 - \frac{(r-r_0)^2}{2v_0^2 t^2}\right)}} e^{-\frac{(r-r_0)^2}{4v_0^2 t/\lambda}} \left(1 + \frac{1}{1 - \frac{(r-r_0)^2}{2v_0^2 t^2}}\right). \tag{3.46}$$

For large values of t this expression simplifies to

$$P(r, t_\infty) = \frac{1}{\sqrt{4\pi \frac{v_0^2}{\lambda} t}} e^{-\frac{(r-r_0)^2}{4v_0^2 t/\lambda}}. \tag{3.47}$$

Consequently, on long timescales the step-size distribution of our Levy walk converges to a normal distribution with a mean of $\mu = r_0$ and a variance of $\sigma^2 = 2\frac{v_0^2}{\lambda} t$. We start our analysis of the two- and three-dimensional CTRW by again deriving the mean squared displacement.

Analogously to (3.29), the multidimensional mean squared displacement (MSD) can be obtained by

$$\langle \boldsymbol{r}^2(t)\rangle = -\nabla_{\boldsymbol{k}}^2 P(\boldsymbol{k},t)|_{\boldsymbol{k}=\boldsymbol{0}} \tag{3.48}$$

$$= -\mathscr{L}^{-1}\left[\nabla_{\boldsymbol{k}}^2 P(\boldsymbol{k},t)|_{\boldsymbol{k}=\boldsymbol{0}}\right]. \tag{3.49}$$

Since $P(\boldsymbol{k},t)$ contains $\boldsymbol{k}$ only in the argument of Ψ and ψ, applying $\nabla_{\boldsymbol{k}}$ to $P(\boldsymbol{k},t)$ is analogous to taking the derivative with respect to s and multiplying with $-i\boldsymbol{v}$. Consequently, one finds Zaburdaev et al., 2016

$$\nabla_{\boldsymbol{k}}^2 P(\boldsymbol{k},t)|_{\boldsymbol{k}=\boldsymbol{0}} = \left[\frac{\Psi(s)\psi''(s)}{(1-\psi(s))^2} + \frac{\Psi''(s)}{1-\psi(s)}\right]\int \boldsymbol{v}^2 h(\boldsymbol{v})d\boldsymbol{v}. \tag{3.50}$$

To proceed further, we replace the waiting time distributions by $\Psi(s) = 1/(\lambda+s)$ and $\psi(s) = \lambda/(\lambda+s)$ to arrive at

$$\nabla_{\boldsymbol{k}}^2 P(\boldsymbol{k},t)|_{\boldsymbol{k}=\boldsymbol{0}} = \left[\frac{2\lambda}{(s+\lambda)^4\left(1-\frac{\lambda}{s+\lambda}\right)^2} + \frac{2}{(s+\lambda)^3\left(1-\frac{\lambda}{s+\lambda}\right)}\right]\int \boldsymbol{v}^2 h(\boldsymbol{v})d\boldsymbol{v} \tag{3.51}$$

$$= \frac{2}{s^2(s+\lambda)}\langle \boldsymbol{v}^2\rangle \tag{3.52}$$

Remarkably the time evolution of this expression is structurally independent of the dimensionality, which affects the term $\langle \boldsymbol{v}^2\rangle$ only. To express $\langle \boldsymbol{r}^2(t)\rangle$ explicitly, we start by calculating the inverse Laplace transform of (3.52),

$$\langle \boldsymbol{r}^2(t)\rangle = \left(e^{-\lambda t} - 1 + \lambda t\right)\frac{2\langle \boldsymbol{v}^2\rangle}{\lambda^2} \tag{3.53}$$

which is identical to $\langle \boldsymbol{r}^2(t)\rangle_{1D}$. In order to evaluate $\langle \boldsymbol{v}^2\rangle$, we use the fact that the observed process is isotropic, i. e. the velocity probability density distribution depends on $|v|$ only. With $h(\boldsymbol{v}) = \boldsymbol{e}_v v_0$ where $\boldsymbol{e}_v$ is a unit vector with a random orientation, we immediately see that $\langle \boldsymbol{v}^2\rangle = v_0$ and therefore

$$\langle \boldsymbol{r}^2(t)\rangle = \left(e^{-\lambda t} - 1 + \lambda t\right)\frac{2v_0^2}{\lambda^2}. \tag{3.54}$$

Although this result is independent of the dimensionality, one should note that the parameter λ implicitly depends on the scattering cross section and therefore on the dimensionality.

Due to the limitations of our experimental setup introduced in the following section we are restricted to observations of tracer particles in the focal plane and loose information about motion in the z-direction. To account for this fact, we are interested how the projection of $\langle \boldsymbol{r}^2\rangle$ onto the x-axis scales with time. Following the ideas of Zaburdaev et al. Fouxon et al., 2017, we note that for a function $g(\boldsymbol{k}\cdot\boldsymbol{v})$ the average over g with respect to $\boldsymbol{v}$ can be expressed as

$$\langle g\left(\boldsymbol{k}\cdot\boldsymbol{v}\right)\rangle_{\boldsymbol{v}} = \int g\left(kv_x\right)h\left(v_x\right)dv_x, \tag{3.55}$$

where $h(v_x)$ denotes the probability density function (pdf) of v_x, the x-component of $\boldsymbol{v}$. For our application, where $\boldsymbol{v}$ assumes a constant value v_0 with a random orientation during a step in the CTRW, $h(v_x)$ is given by Fouxon et al., 2017

$$h(v_x) = S_{(d/2)-2,v_0}(v_x), \tag{3.56}$$

where $S_{(d/2)-2,v_0}(v_x)$ is the power semicircle pdf in d dimensions

$$S_{(d/2)-2,v_0}(v_x) = \frac{\Gamma(d/2)}{\sqrt{\pi}v_0\Gamma((d-1)/2)}\left(1-\frac{v_x^2}{v_0^2}\right)^{(d-3)/2}, \tag{3.57}$$

and Γ is the Gamma function. The resulting expression for the mean squared displacement in $d \leq 2$ - dimensions is

$$\langle \boldsymbol{r}^2(t)\rangle_{d,x} = \left(e^{-\lambda t} - 1 + t\lambda\right)\frac{2}{\lambda^2}\int_{-v0}^{v0} v_x^2 S_{(d/2)-2,v_0}(v_x)\, dv_v. \tag{3.58}$$

For $d = 2$ this expression simplifies to

$$\langle \boldsymbol{r}^2(t)\rangle_{2D,x} = \left(e^{-\lambda t} - 1 + t\lambda\right)\frac{v_0^2}{\lambda^2} \tag{3.59}$$

and for $d = 3$ to

$$\langle \boldsymbol{r}^2(t)\rangle_{3D,x} = \left(e^{-\lambda t} - 1 + t\lambda\right)\frac{2v_0^2}{3\lambda^2}. \tag{3.60}$$

Although the aforementioned procedure to reduce the d-dimensional expression of $\langle g(\boldsymbol{k}\cdot\boldsymbol{v})_{\boldsymbol{v}}\rangle$ is also applicable to $p(\boldsymbol{k}, s)$, no analytic expression for $p(\boldsymbol{r}, t)$ is known and we have to rely on numerical simulations to study $p(\boldsymbol{r}, t)$ for $d > 1$.

3.2.3 Alternating Continuous Time Random Walk

In this section we extend the current continuous time random walk model to include alternating states of free diffusion and fixed velocity Levy walks, motivated by the short phases of swimmer-tracer interactions and the long waiting times until the next swimmer arrives. The duration of free diffusion phases is characterized by an exponential waiting time distribution $\psi_f(\tau) = \lambda_f e^{-\lambda_f \tau}/$ where parameter λ_f depends on the number of active swimmers in the solution and the dimensionality of the system. The probability density function of the step displacements $q_f(\boldsymbol{r}, \tau)$ is the joint probability distribution $q_f(\boldsymbol{r}, \tau) = \phi_f(\boldsymbol{r}|\tau)\psi_f(\tau)$. Since the swimmers undergo free diffusion, the step-size distribution for a fixed step duration τ is a Gaussian with $\phi_f(\boldsymbol{r}|\tau) = \exp\left(-r^2/4D\tau\right)/\left(4\pi D\tau\right)^{d/2}$, where D is the diffusion coefficient of the tracer particles in the medium without swimmers and d the dimension. As in the previous section, the durations of the swimmer-tracer interactions are exponentially distributed with the rate parameter λ_i and due to the fixed displacement velocity $\boldsymbol{v}_0$ the step size distribution is $\phi_i(\boldsymbol{r}|\tau) = C_n\delta(|\boldsymbol{r}| - v_0 t)$, where the constant C_n depends on the dimensionality of the system. In two dimensions, the tracers are located in a ring with radius $v_0\tau$ and hence $C_2 = 1/2\pi$. For the three-dimensional case, the traces spread on the surface of a sphere and the normalization constant becomes $C_3 = 1/4pi$. Analogue to q_f, the probability density function for the interaction steps is $q_i(\boldsymbol{r}, \tau) = \phi_i(\boldsymbol{r}|\tau)\psi_i(\tau)$.

We start the derivation of the probability density function $P(\boldsymbol{r},t)$ by explicitly taking all possible combinations of alternating interaction and resting phases into account. Accordingly, $P(\boldsymbol{r},t)$ is composed of the probability of not finishing an interaction step plus the combined probability of a completed interaction step and an incomplete rest phase. This series is extended by further combination of interaction and resting, leading to the expression,

$$\begin{aligned} P(\boldsymbol{r},t) = Q_i(\boldsymbol{r},t) &+ \int_0^t dt' \int d\boldsymbol{r}' q_i(\boldsymbol{r}',t') Q_r(\boldsymbol{r}-\boldsymbol{r}', t-t') \\ &+ \int_0^t dt' \int_0^{t'} dt'' \int d\boldsymbol{r}' \int d\boldsymbol{r}'' q_i(\boldsymbol{r}',t') q_r(\boldsymbol{r}-\boldsymbol{r}, t-t') Q_i(\boldsymbol{r}'-\boldsymbol{r}'', t'-t'') \\ &+ \dots . \end{aligned} \tag{3.61}$$

Here, $Q_f(\boldsymbol{r},t)$ and $Q_f(\boldsymbol{r},t)$ are the distributions for the incomplete steps. They are defined as $Q_f(\boldsymbol{r},t) = \phi_f(\boldsymbol{r}|t)(1-\int_0^t \psi_f(t')dt')$ and $Q_i(\boldsymbol{r},t) = \phi_i(\boldsymbol{r}|t)(1-\int_0^t \psi_i(t')dt')$. It is also possible to choose an incomplete resting phase as the starting point for this derivation, which leads to similar results. Taking the Fourier Laplace transform of the former equation and using the properties of the geometric series, equation (3.61) simplifies to

$$P(\boldsymbol{k},s) = Q_i(\boldsymbol{k},s) + q_i(\boldsymbol{k},s)Q_f(\boldsymbol{k},s) + q_i(\boldsymbol{k},s)q_f(\boldsymbol{k},s)Q_i(\boldsymbol{k},s) + \dots \tag{3.62}$$

$$= [Q_i(\boldsymbol{k},s) + Q_f(\boldsymbol{k},s)q_i(\boldsymbol{k},s)] \sum_{l=0}^{\infty} q_i(\boldsymbol{k},s)^l q_f(\boldsymbol{k},s)^l \tag{3.63}$$

$$= \frac{Q_i(\boldsymbol{k},s) + Q_f(\boldsymbol{k},s)q_i(\boldsymbol{k},s)}{1 - q_f(\boldsymbol{k},s)q_i(\boldsymbol{k},s)}. \tag{3.64}$$

Next, we derive the explicit form of $Q_f(\boldsymbol{k},s)$ by applying the Fourier transform and using the Laplace shift property, resulting in the following equation,

$$q_f(\boldsymbol{k},s) = \mathscr{L}\left[e^{-\boldsymbol{k}^2 Dt}\psi_f(t)\right] \tag{3.65}$$

$$= \psi(s + D\boldsymbol{k}^2) \tag{3.66}$$

$$= \frac{\lambda_f}{\lambda_f + s + D\boldsymbol{k}^2} \tag{3.67}$$

$$= \lambda_f Q_f(\boldsymbol{k},t). \tag{3.68}$$

Repeating these steps for Q_f, we find

$$Q_f(\boldsymbol{k},s) = \frac{1}{\lambda_f + s + D\boldsymbol{k}^2}. \tag{3.69}$$

For the one-dimensional system the relations $q_i = \lambda_i/(s+\lambda_i)$ and $Q_i = 1/(s+\lambda_i)$ were already derived in the previous section. Since $\phi_i(\boldsymbol{r}|\tau)$ defines a ring in two dimensions and the shell of a sphere in three dimensions, the Fourier Transform of $\phi_i(\boldsymbol{r}|\tau)$ is not as trivial as in the one-dimensional case. A derivation of the n-dimensional Fourier transformation of the radial δ-distribution is given in Vembu, 1961,

$$\mathscr{F}\left[C_n\delta(|\boldsymbol{r}|-a)\right] = \frac{2^\nu J_\nu(|\boldsymbol{k}|a)}{(|\boldsymbol{k}|a)^\nu}. \tag{3.70}$$

Here, J_ν is the Bessel function of first kind and ν is related to the dimension n as $\nu = n/2-1$ for $n > 1$. Using this result, we can derive the explicit form of $q_i(\boldsymbol{k}, s)$ as

$$q_i(\boldsymbol{k}, s) = \mathscr{L}\left[\frac{2^\nu J_\nu(|\boldsymbol{k}|v_0 t)}{(|\boldsymbol{k}|v_0 t)^\nu}\psi_t(t)\right] \tag{3.71}$$

$$\tag{3.72}$$

For $n = 2$ this expression evaluates to

$$q_i(\boldsymbol{k}, s) = \mathscr{L}\left[J_0(|\boldsymbol{k}|v_0 t)\lambda_i e^{-\lambda_i t}\right] \tag{3.73}$$

$$= \frac{\lambda_i}{\sqrt{v_0^2 k^2 + (s+\lambda_i)^2}}. \tag{3.74}$$

Inserting these results into 3.64 yields the following result,

$$P(\boldsymbol{k}, s) = \frac{\frac{1}{\sqrt{v_0^2 k^2+(s+\lambda_i)^2}} + \frac{1}{\lambda_f+s+D\boldsymbol{k}^2}\frac{\lambda_i}{\sqrt{v_0^2 k^2+(s+\lambda_i)^2}}}{1 - \frac{\lambda_f}{\lambda_f+s+D\boldsymbol{k}^2}\frac{\lambda_i}{\sqrt{v_0^2 k^2+(s+\lambda_i)^2}}} \tag{3.75}$$

and for the three-dimensional case we get

$$q_i(\boldsymbol{k}, s) = \mathscr{L}\left[\frac{\sqrt{2}J_{1/2}(|\boldsymbol{k}|v_0 t)}{\sqrt{|\boldsymbol{k}|v_0 t}}\lambda_i e^{-\lambda_i t}\right] \tag{3.76}$$

$$= \frac{\lambda_i\left(\pi - 2\tan^{-1}\left(\frac{s+\lambda_i}{|\boldsymbol{k}|v_0}\right)\right)}{\sqrt{\pi}|\boldsymbol{k}|v_0} \tag{3.77}$$

For the one-dimensional case we use the results for $Q_i = 1/(s+\lambda_i)$ from the previous section and insert them into equation (3.64) to arrive at

$$P(k, s) = \frac{(s+\lambda_f)\left(s+\lambda_f+\lambda_i+Dk^2\right)}{(s+\lambda_f+Dk^2)\left(k^2v^2+(s+\lambda_i)^2\right) - \lambda_f\lambda_i(s+\lambda_i)}. \tag{3.78}$$

Using relation (3.52) we obtain the mean squared displacement for the alternating model by first taking the second derivative of $P(k, s)$ and evaluating it at $k = 0$,

$$\begin{aligned}\frac{\partial^2 P(k,s)}{\partial k^2}|_{k=0} = &\frac{2D(\lambda_l+s)}{(\lambda_f+s)(\lambda_i+s)^2 - \lambda_f\lambda_i(\lambda_i+s)} \\ &- \frac{(\lambda_i+s)(\lambda_f+\lambda_i+s)\left(2D(\lambda_i+s)^2+2v^2(\lambda_f+s)\right)}{\left((\lambda_f+s)(\lambda_i+s)^2 - \lambda_f\lambda_i(\lambda_i+s)\right)^2}\end{aligned} \tag{3.79}$$

and then apply the inverse Laplace transformation. This yields

$$\begin{aligned}\langle r^2(t)\rangle = &\frac{2\left(\lambda_f D\lambda_i+\lambda_i v^2\right)}{\lambda_f(\lambda_f+\lambda_i)^2}e^{-(\lambda_f+\lambda_i)t} + \frac{2\left(\lambda_f v^2-\lambda_i v^2\right)}{\lambda_f\lambda_i^2}e^{-\lambda_i t} \\ &+ \frac{2\left(D\lambda_i^2+\lambda_f v^2\right)}{\lambda_i(\lambda_f+\lambda_i)}t - \frac{2\left(D\lambda_i^3+\lambda_f^2 v^2+\lambda_f\lambda_i v^2-\lambda_i^2 v^2\right)}{\lambda_i^2(\lambda_f+\lambda_i)^2}.\end{aligned} \tag{3.80}$$

We note that for vanishing interactions times ($\lambda_i \to \infty$) the mean squared displacement becomes diffusive with $\lim_{\lambda_i\to\infty}\langle r^2(t)\rangle = 2Dt$, while for very small resting times ($\lambda_f \to \infty$), the result of pure Levy walk model (3.40) is recovered. For increasing observation times, the

influence of the exponential terms vanishes and the mixed model shows diffusive behavior with a diffusion constant of

$$D_{mixed} = \frac{D\lambda_i^2 + \lambda_f v_0^2}{\lambda_i(\lambda_f + \lambda_i)} \tag{3.81}$$

$$= D_f \frac{\lambda_i}{\lambda_f + \lambda_i} + D_i \frac{\lambda_f}{\lambda_f + \lambda_i}. \tag{3.82}$$

with $D_i = v_0^2/\lambda_i$. To find the small time behavior of 3.80, we replace the exponential terms by their Taylor expansion up to second order $e^{-\lambda_i t} = 1 - \lambda_i t + \lambda_i^2 t^2/2 + O(3)$ and find

$$\langle r^2(t \ll 1)\rangle = t^2 \left(v^2 + D\lambda_i\right). \tag{3.83}$$

Hence, at small time scales the tracer particles spread ballistically. Again, the transition time from the ballistic to the diffusive regime is determined by the inverse of the rate parameter λ_i. In contrast to the pure Levy model, a direct transition to diffusive motion is only observed for large values of λ_f, corresponding to short phases of free diffusion.

To better approximate the experimental conditions, we have to change the initial conditions of our model to include a mixture of starting in interaction phase (interact-first) and particles starting in the free diffusion phase (rest-first). The probability density function for the extended model is

$$P_{mix}(\boldsymbol{r}, t) = \frac{\lambda_f}{\lambda_f + \lambda_i} P_{if}(\boldsymbol{r}, t) + \frac{\lambda_i}{\lambda_f + \lambda_i} P_{rf}(\boldsymbol{r}, t), \tag{3.84}$$

where P_{if} and P_{rf} are the pdfs for the interact first and rest first model, respectively. The weights between both distributions were chosen in dependence of λ_f and λ_i since we expect the number of particles to be observed in either phase to be proportional to the time they spend on average in each phase. The mean squared displacement is then given by

$$\langle r_{mix}^2(t)\rangle = \alpha\langle r_{if}^2(t)\rangle + (1-\alpha)\langle r_{rf}^2(t)\rangle, \tag{3.85}$$

where $\langle r_{if}^2(t)\rangle$ is the result from equation (3.80). To derive $\langle r_{rf}^2(t)\rangle$, i.e. the expression for the wait-first model in one dimension, we use the same approach as for the interact-first model and find

$$P_r(k, s) = \frac{k^2 v^2 + \lambda_f(\lambda_i + s) + (\lambda_i + s)^2}{(\lambda_f + Dk^2 + s)\left(k^2 v^2 + (\lambda_i + s)^2\right) - \lambda_f \lambda_i(\lambda_i + s)} \tag{3.86}$$

for the probability density function and

$$\langle r_r^2(t)\rangle = \frac{2t\left(D\lambda_i^2 + \lambda_f v^2\right)}{\lambda_i(\lambda_f + \lambda_i)} - \frac{2\left(\lambda_f D + v^2\right) e^{-t(\lambda_f + \lambda_i)}}{(\lambda_f + \lambda_i)^2} \tag{3.87}$$

$$+ \frac{2\left(\lambda_f D\lambda_i^2 - \lambda_f^2 v^2 - 2\lambda_f \lambda_i v^2\right)}{\lambda_i^2(\lambda_f + \lambda_i)^2} + \frac{2v^2 e^{\lambda_i(-t)}}{\lambda_i^2} \tag{3.88}$$

for the mean squared displacement. As in the interact-first model, the rest-first model exhibits diffusive behavior for increasing observation times with the same diffusion constant (3.82). At small time scales with $t < 1/\lambda_f$ the msd is also diffusive, but with $\langle r_i^2(t)\rangle \approx 2D_f t$. The transition between both diffusive regimes is characterized by a phase of ballistic spreading.

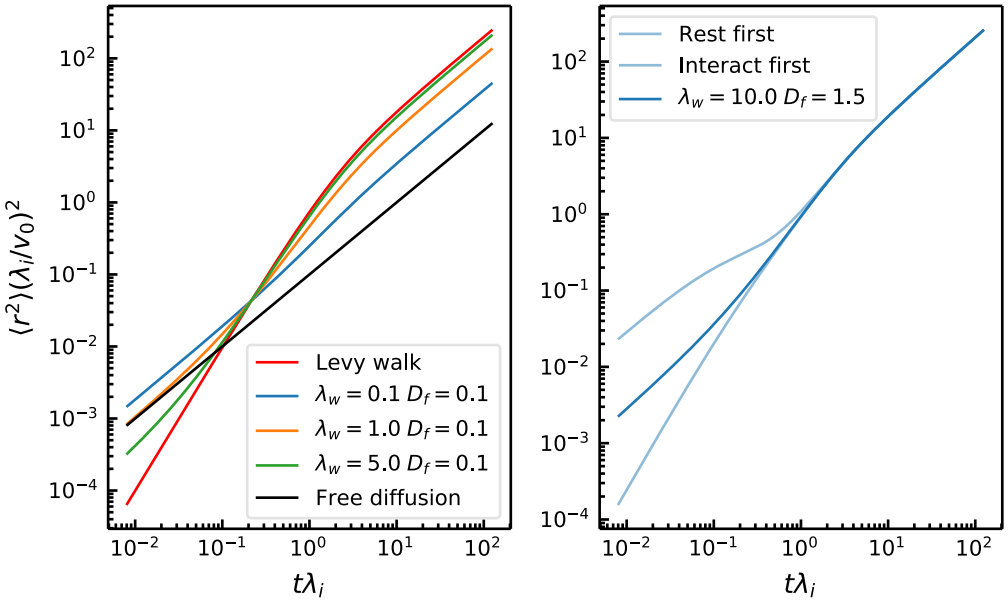

Fig. 3.9: Mean squared displacement curves for the alternating CTRW model with varying rest parameters λ_f and a fixed diffusion constant D_f (left). In addition, the mean squared displacements for the Levy walk model as well as for free diffusion are shown. In the right figure three different initial conditions are shown for the alternating model, including the limiting cases where all tracers start in free diffusion mode (rest-first) or in the interaction phase (interact-first). In the third case, the number of resting and interacting swimmers corresponds to the ratio of λ_f to the interaction rate λ_i.

As visualized in figure 3.9, the rest-first and the interact-first process forms the limiting case for the mixed model and the experimentally observed mean squared displacement curves should be located between the curves defined by these models. In contrast to the pure Levy walk model, no inversion of $P_r(k, s)$ is known and we have to rely on numerical simulations to calculate the probability density function for the mixed model.

3.3 Numerical simulation of Continuous Time Random Walk model

To support our previous findings and approximate the probability density functions for the multidimensional case, we perform a number of numerical studies.

3.3.1 Numerical procedures

A single trajectory for the Levy walk model is generated by consecutively drawing interaction times from the distribution $\Psi(\tau)$ until the maximum observation time T is reached. This series of interactions times defines the reorientation events - at the beginning of each interaction time τ_i, the particle is located at position $\boldsymbol{r}_i$ and assumes a random orientation e_r. The position after the next interaction period is then defined by $\boldsymbol{r}(t_{i+1}) = \boldsymbol{r}(t_i) + \boldsymbol{e}_i \cdot \tau_{i+1} \cdot v_0$.

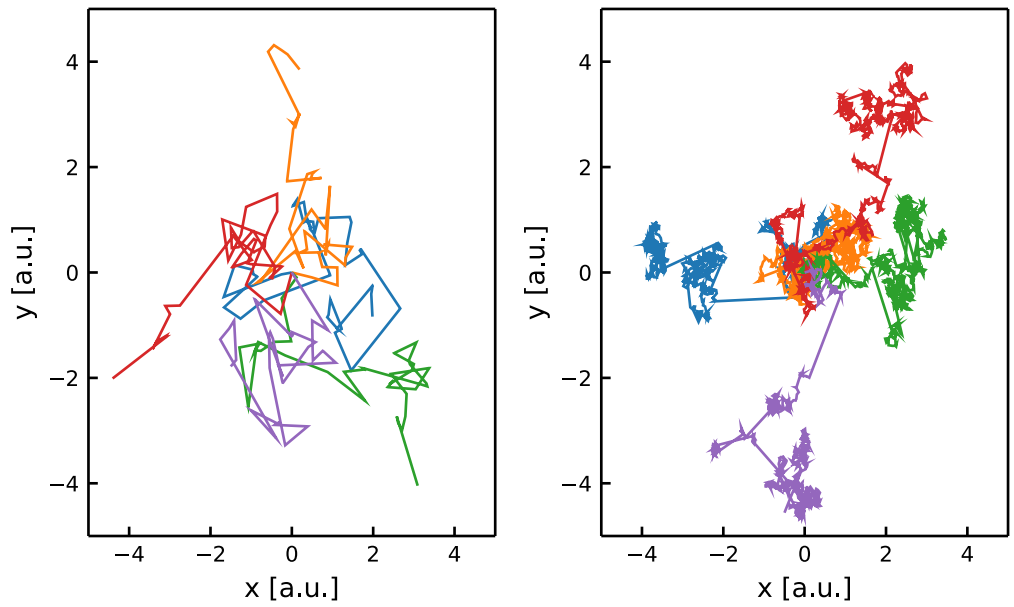

Fig. 3.10: Sample trajectories generated using the pure Levy walk model (left) and the extended model with interchanging phases of free diffusion and tracer swimmer interactions (right). For both simulations the interaction rate was set to $\lambda_i = 2$ and the swimmer speed to $v = 1$

Following this procedure we obtain a series of positions $R = r(t_0)...r(T)$ that defines a trajectory at the reorientation points. For further analysis we want to evaluate the trajectories at specific times points t_i and must therefore derive the positions between the reorientation points. Since the tracer moves with a constant velocity, we find its position $\boldsymbol{r}(t_i + t')$ with $t' < \tau_{i+1}$ by means of linear interpolation, i.e. $\boldsymbol{r}(t_i + t') = \boldsymbol{r}(t_i) + \boldsymbol{e}_i t' v_0$.

In order to check the accuracy of our numerical procedure, we generate multiple samples with an increasing number of trajectories and compare them to our analytical findings. Starting by evaluating the performance of the numerical procedure during an approximation of the mean squared displacement (3.40), we find that the relative error ϵ_r scales like

$$\epsilon_r = \sum_{i=1}^{N} \frac{\left|\langle r^2(t_i)\rangle - \langle r^2_{num}(t_i)\rangle\right|}{\langle r^2(t_i)\rangle} \propto \frac{1}{\sqrt{N}}, \tag{3.89}$$

where N is the number of individual random walks. As depicted in figure 3.11 the relative error depends on the dimensionality D of the system, with $\epsilon_r(D) = \epsilon_r/D$ To study the numerical accuracy of our procedure to model the probability density function, we start with the one dimensional case and generate a sample of $N = 10000$ trajectories. We calculate the pdf at multiple times t_i and compare it to the analytical solution from equation (3.42). The results are shown in figure 3.12. Again, the numerical procedure reproduces the analytical findings quite well, with small deviations for the ballistic front. We proceed by generating the distributions for the two- and three-dimensional case and note that the dimensionality affects the distribution by changing the magnitude of the ballistic front. Especially for the three-dimensional case, the distributions exhibits a visible front only at very short timescales and looks bell-shaped for larger times. In an experiment, the frequency of tracer-swimmer interaction increases with the concentrations of active swimmers in the solution, but is

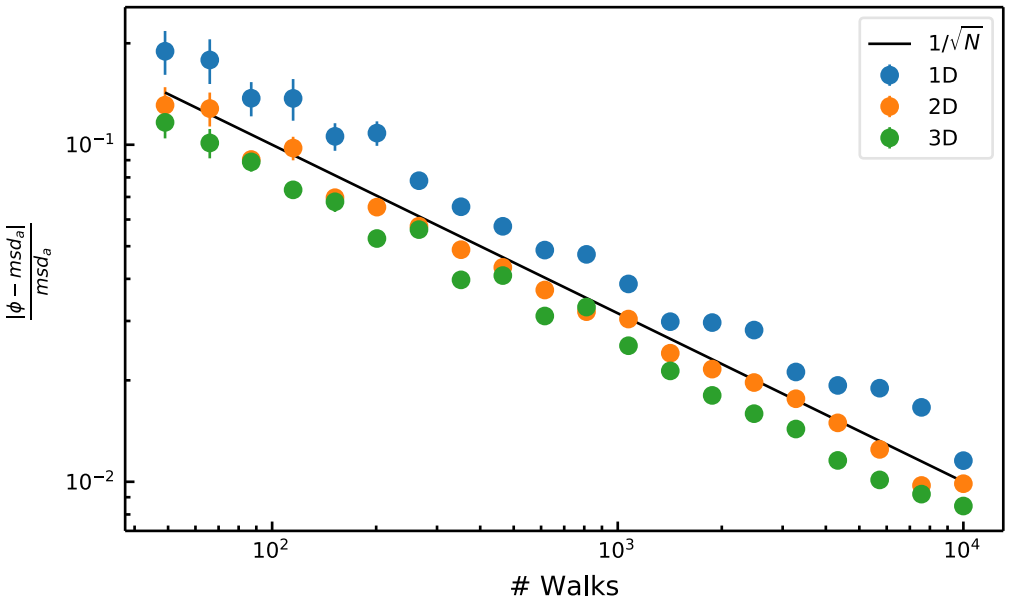

Fig. 3.11: Relative error between the numerically estimated mean squared displacement of the pure Levy walk model and its analytical counterpart (3.40) for increasing numbers of independent Levy walks in different dimensions. The points mark the mean relative error for a sample of 50 different realizations for each Levy walk with sample size N. The error bars indicate the standard deviation of the different samples. The errors decreases with $1/\sqrt{N}$, as indicated by the black line.

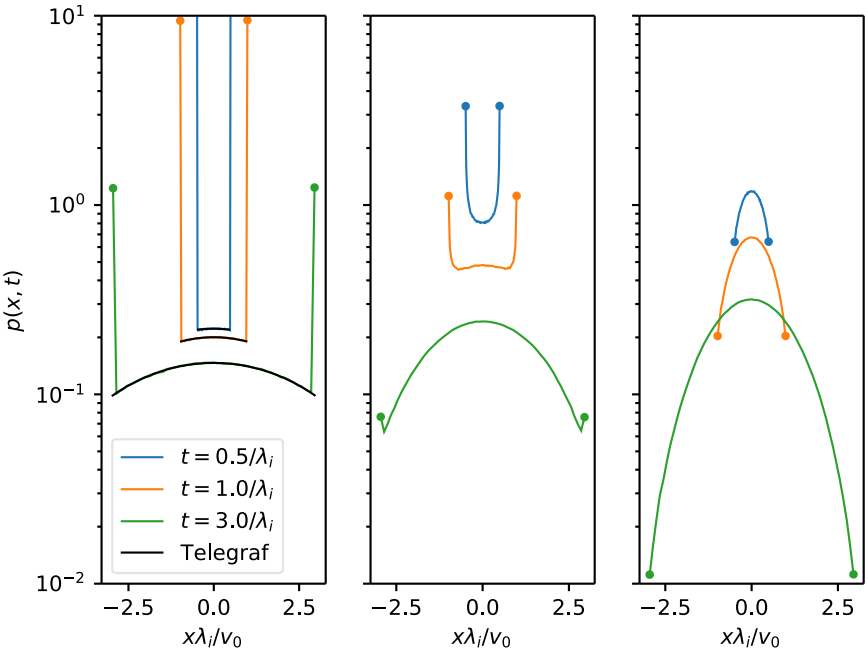

Fig. 3.12: Numerical approximation of the step size distribution for the pure Levy walk model in one, two and three dimensions. For the one-dimensional case, the analytical distribution from equations (3.42) was included as reference.

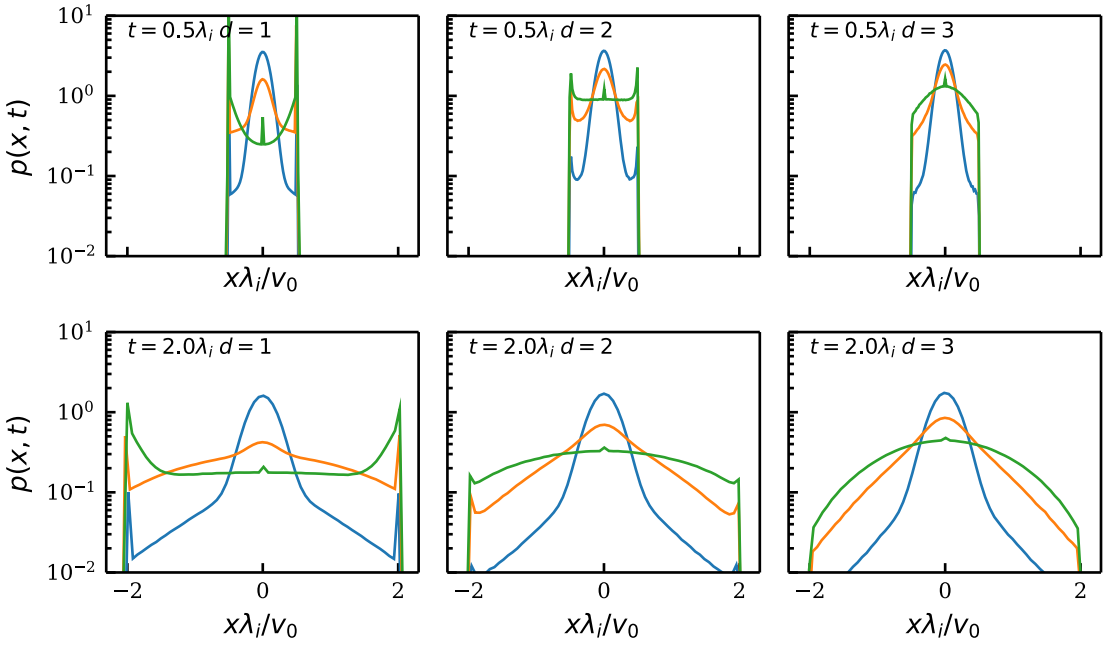

Fig. 3.13: Numerical displacement distribution for rest model with different rest rates λ_f in one, two and three dimensions. The blue, orange and green lines correspond to a rest rate of $\lambda_f = 0.1$, $\lambda_f = 1$ and $\lambda_f = 10$ respectively.

ultimately limited by the available nutrients that are required by the swimmers, resulting in periods of rest between the interaction phases. Analogous to our analytical model, we incorporate this fact by extending the current simulation procedure to include a phase of rest after each interaction. During this rest, the tracer undergoes diffusive motion with a diffusion constant D_f. The duration of the resting periods is drawn from an exponential distribution ψ_f with a waiting time parameter λ_f which depends on the swimmer concentration. We discretize this period of Brownian motion using time steps of size τ_f and construct the trajectory using a random walk with a stepsize distribution

$$P(r_f, \tau_f) = \frac{1}{\sqrt{2\pi n D \tau_f}} e^{-r^2/2nD\tau_f}, \tag{3.90}$$

where n is the dimensionality. The number of runs starting in free diffusion resp. in interaction mode is chosen to correspond to the ratio between λ_f and λ_i.

Using this extended model, we compute the mean squared displacements and the probability density function for different dimensionality and combinations of λ_i, λ_f, D_f and compare these results to equation (3.88). Again, the results of this simulations agree well with our theoretical predictions. We proceed further by calculating the pdfs for the different scaling regimes of the pdfs using multiple combinations of parameters. The results are visualized in figure 3.13. Not surprisingly, for large observation times, the pfds show the typical Gaussian shape that is indicative of free diffusion. At short timescales, however, the fat tails mentioned in Leptos et al., 2009 are visible.

3.4 Experimental Observations

The change in diffusive behavior was first observed by Wu and Libchaber Wu and Libchaber, 2000. They recorded tracer motion in a quasi two-dimensional soap film with fluorescent beads and swimming *E. coli* cells and noticed two different regimes in the mean square displacement. Follow up experiments performed by Leptos et al Leptos et al., 2009, as well as Kurtuldu et al. Kurtuldu et al., 2011 included different concentrations of swimmers and measured the effects on the probability density functions of the step sizes. We extend these experiments even further by using genetically modified bacteria to explore the influence of different swimming patterns as well as a range of swimmer concentrations.

3.4.1 Model strain

We use *Shewanella Putrefaciens* as our model organism, a marine bacterium often found in soil and and other structured environments. Its cellbody has a cylindrical shape with a diameter of $0.7 - 1.1\mu m$ and a length of $2 - 4\mu m$. The wildtype is propelled by a large polar flagellum and a number of smaller, lateral flagella. These lateral flagella play a major role in biofilm formation and may thereby prevent observations of swimming bacteria at high concentrations. We therefore used a strain ($\Delta flagL$) for which the lateral flagella were genetically removed. With the remaining polar flagellum, the cells exhibit a swimming pattern of alternating forward and backward run phases with a maximum velocity of approximately $57\mu m/s$ Bubendorfer et al., 2014. To change the swimming pattern, we introduced two additional modifications to the $\Delta flagL$ strain, namely an enhancement to switch between forward and backward motion, resulting in an increased switching frequency between those states ($\Delta flagL - cheY - GOF$). The second modification was a deletion of the aforementioned switch, leading to a version of *Shewanella* that is locked in forward swimming mode ($\Delta flagL \Delta cheY$).

3.4.2 Experimental setup

For each of the different experimental conditions, the bacteria were grown overnight in LB medium until they reached an optical density (OD) of 600. To reach the desired concentration of bacteria, the sample solutions with the bacteria were first centrifuged at 1,200 × g for 5 minutes. Afterwards the sediment was diluted with the appropriate volume of the tracer suspension to achieve the correct dilution factor. The concentration was checked by measuring the optical density. The tracer particles are fluorescently coated latex beads with a diameter of $0.33\mu m$. The fluorescent dye is mCherry, a fluorophore with a peak absorption wavelength of $587nm$ and a peak emission wavelength of $610nm$. The swimmer-tracer solution was placed on a microscope slide with vertical spacers and enclosed by a cover slip. Observations were performed using a Leica DMI 6000 B inverse microscope with a pco.edge sCMOS camera (PCO). The images were acquired at room temperature with a time resolution of 100 frames per second. To measure the relation of active and inactive swimmers as well as the swimming speed, additional time lapse images were acquired for each sample. Since the swimmers were not visible in the fluorescent channel, the control images were recorded using differential interference contrast (DIC) microscopy.

Parameter	Description	Value
T	Temperature	$295K$
r_{bead}	Radius of fluorescent beads	$0.33\mu m$
η	Dynamic viscosity	$0.95mPa \cdot s$
d_{px}	Pixel size	$0.0645\mu m$
t_{frame}	Frame duration	$10ms$

Tab. 3.1: The various experimental parameters and their values.

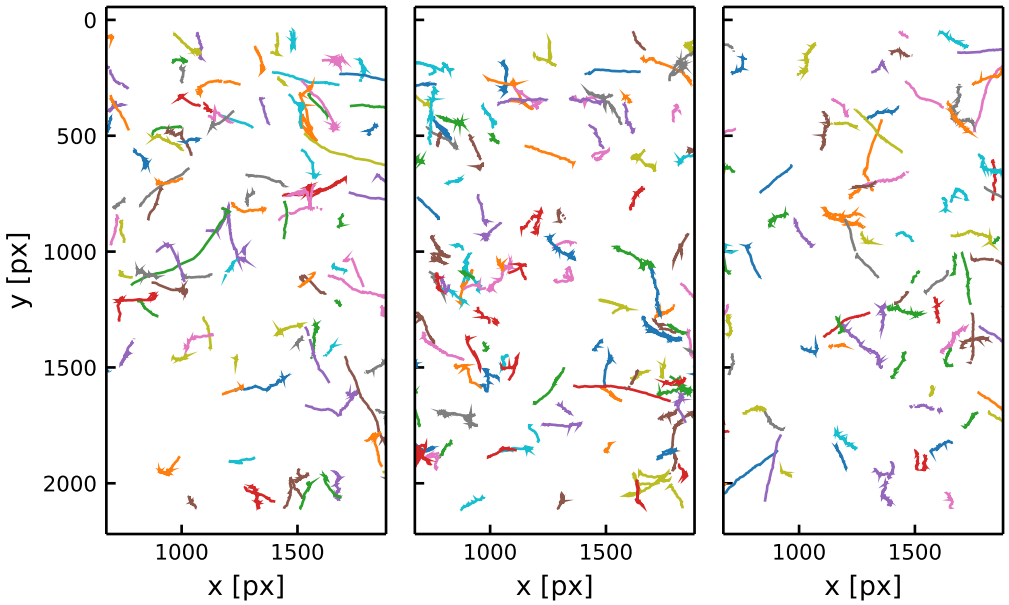

Fig. 3.14: A sample of observed swimmer trajectories for the different strains of *S. Putrefaciens*. The cells were recorded for $T = 3.0s$ and each pixel has an edge length of $64nm$. The unmodified species in the image to the left displays a mixture of rather straight paths and a number of trajectories with sharp reorientations. For the Δ*flagL-cheY-GOF* mutant in the middle, the tracks contain more bends and the straight sections are shorter. The sample trajectories of the Δ*flagL*Δ*cheY* mutant appear to be similar to the unmodified strain, containing slightly more straight trajectories than the latter.

3.4.3 Track analysis

We start our analysis by extracting some basic properties from the swimmer trajectories to compare the different strains and to detect potential influences of the swimmer concentration on the swimming behavior. By visualizing a subset of the recorded tracks and comparing them for the individual strains, the different swimming properties become visible 3.14. As expected the Δ*flagL*Δ*cheY* strain predominantly moves in long, nearly straight trajectories while the Δ*flagL-cheY-GOF* frequently changes its swimming direction, resulting in short trajectories. The wildtype's behavior is in between both mutants, displaying some reorientation events during the observation time, but significantly less than the Δ*flagL-cheY-GOF* mutant. We start to quantify these qualitative differences by estimating the swimming velocity and the duration of run phases. To estimate the transition from ballistic motion to undirected diffusive spreading, we calculate the mean squared displacements of swimmer trajectories and average over all tracks for each strain. The mean squared displacement curves are displayed in figure 3.15 and reflect the aforementioned qualitative results. The Δ*flagL-*

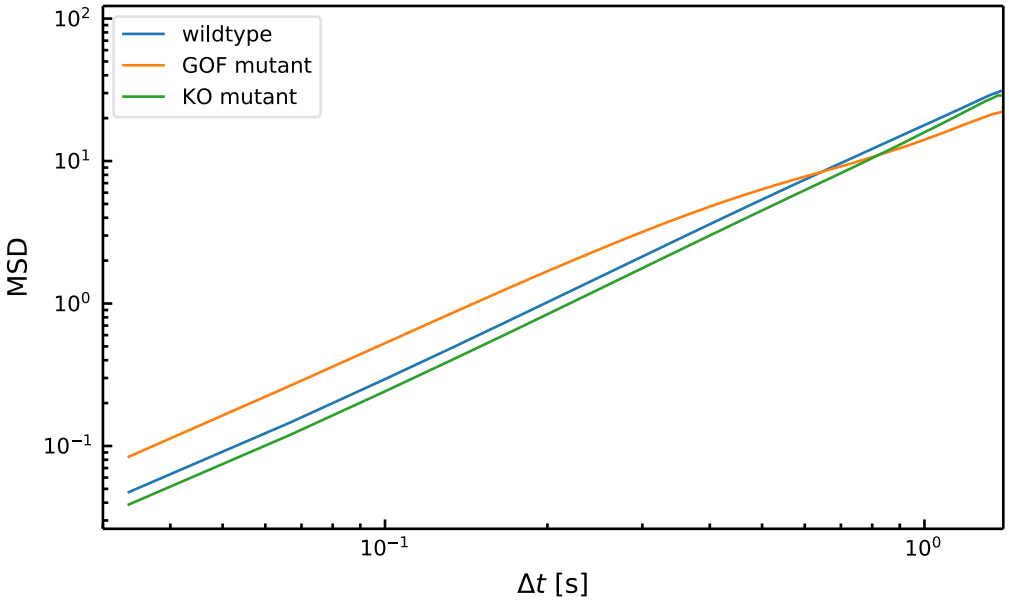

Fig. 3.15: Mean squared displacement curves for the three examined *Shewanella* strains. The wildtype as well as the KO-mutant exhibit ballistic motion over the accessible observation period, while the GOF-mutant changes from ballistic to diffusive motion at $\Delta t > 0.1s$.

cheY-GOF mutant moves ballistically up to a duration of $t \approx 0.4s$. For the wildtype and the Δ*flagL*Δ*cheY* strain, the transition is not visible during the observation time. To estimate the swimmer's average velocity we measure the distance Δr that a swimmer travels in time Δt and calculate the probability density distribution of $\bar{v} = \Delta r / \Delta t$. As long as Δt remains smaller than the transition time to the diffusive regime, $\bar{v}$ should be comparable for all strains, since the genetic modification affects the reversal times only and not the propulsion mechanism. As depicted in figure 3.16, the distribution of observed swimming speeds has a maximum at $\bar{v}_{max} \approx 4.8 \mu m/s$ for all strains at $\Delta t = 20ms$. The mean swimming speed varies between $\bar{v} = 8.72 \mu m/s$ for the wildtype, $7.81 \mu m/s$ for the KO mutant and due to the wider distribution $11.23 \mu m/s$ for the GOF mutant. For longer averaging times Δt, the wildtype and the Δ*flagL-cheY-GOF* mutant display a decrease in $\bar{v}$ due to an increasing number of reorientations during the swimming phase. In contrast to observations reported in Kühn et al., 2018 we observed no second peak in the swimmer speed distribution. This difference is caused by differences in the general experimental setup, especially in the concentration of swimmer cells. The high concentrations used in our setup lead to a rapid depletion of oxygen, which is necessary for fast propulsion. Following the analysis of Leptos et al Leptos et al., 2009, we calculate the probability density function of tracer displacements at different times and rescale them by $\langle x^2 \rangle$. We do this for all three strains and swimmer concentrations. As depicted in figure 3.17, the central part of the distributions resembles the characteristic shape of a Gaussian distribution. On small time scales the curves exhibit strongly pronounced tails departing from the normal distributed center. Using the experimental conditions summarized

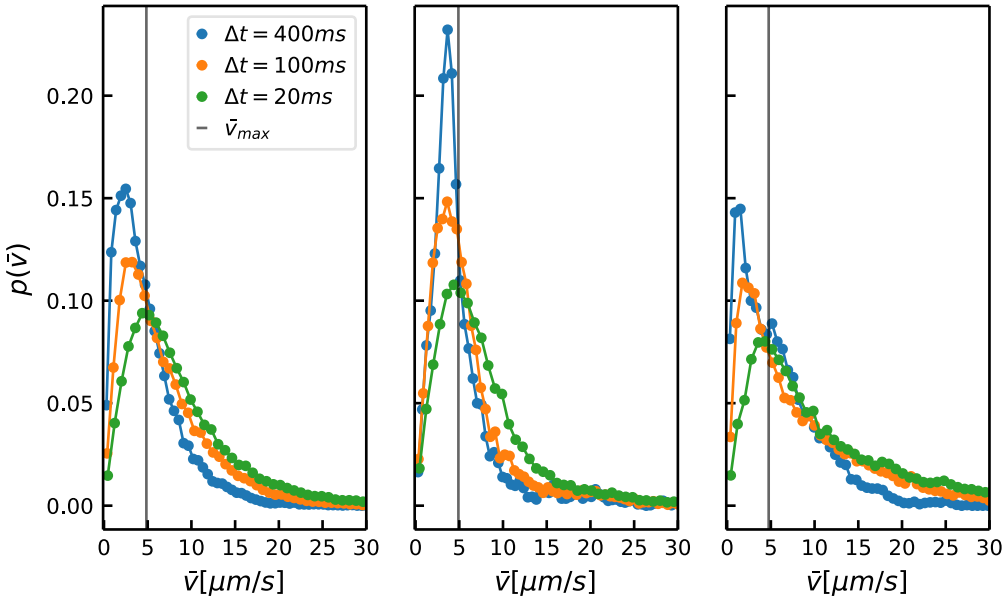

Fig. 3.16: Distribution of average swimmer velocities $\bar{v} = \Delta r/\Delta t$ of unmodified strain (left), Δ*flagL*Δ*cheY* mutant (middle) and Δ*flagL-cheY-GOF* mutant (right). For short averaging times Δt, all strains display similar distributions, with a maximum roughly at $\bar{v}_{max} \approx 4.8\mu m/s$. For longer Δt, both the wildtype and the Δ*flagL-cheY-GOF* mutant show a decreasing average velocity, caused by an increasing number of reorientations during the observation time.

in table 3.1 and the Einstein-Smoluchowski relation we estimate the tracer's free diffusion constant as

$$D_f = \frac{k_b T}{6\pi\eta r_{bead}} \tag{3.91}$$

$$= 0.68\frac{\mu m^2}{s} \tag{3.92}$$

and compare the observed bell curves with their theoretical counterparts for free diffusing particles, see figure 3.17. For small time scales, the inner part of the observed distribution fits the theoretical curve quite well, indicating that many tracer particles are unaffected by the swimmers over this period of time and undergo normal diffusion. The tails are obviously caused by tracer-swimmer interactions and are visible for all strains and concentrations.

For larger time scales the tails become less pronounced and nearly disappear for the wildtype and the KO mutant. Only the GOF mutant exhibits pronounced tails for all observation times, suggesting that the frequent reorientations play a significant role in the process. The effects of the different swimmer concentrations seem to be small. Only the GOF mutant shows clear differences between the base concentration and the fourfold concentrated swimmers. Counter-intuitively, the tails in the distribution of the high concentrated GOF mutant are less pronounced compared to the base concentration and the twofold concentrated swimmers. This might indicate a fast depletion of nutritions due to the large number of cells, leading to actually fewer swimming cells. With the diffusive contributions these experimentally obtained curves differ from the pure Levy walk model of section 3.2.2 but show similarities to our mixed model. To quantify these observations, we fit the free parameters of the mixed

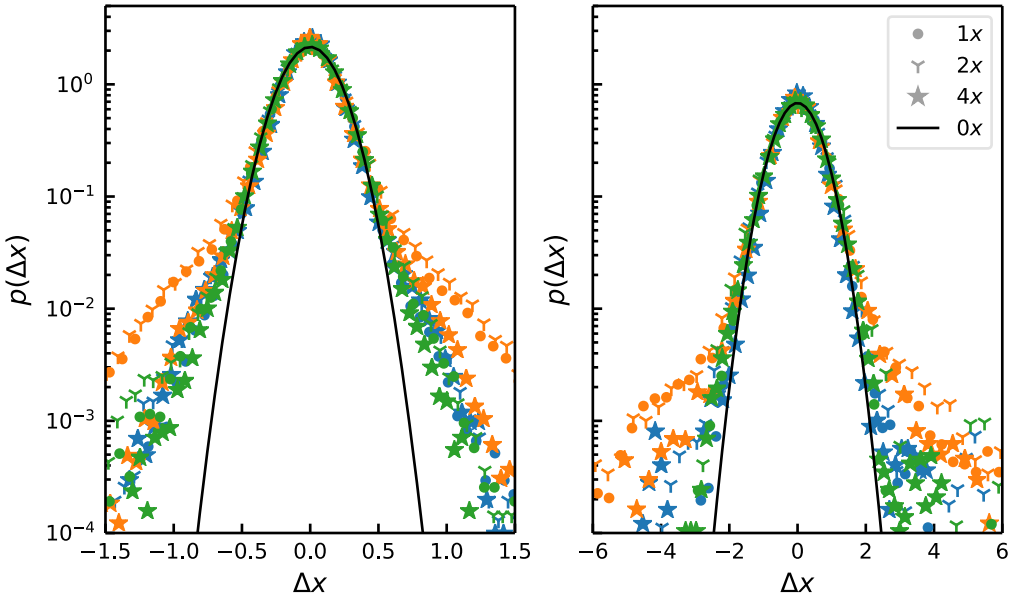

Fig. 3.17: Histogram of measured tracer displacements for different strains and concentrations after $t = 0.05s$ (left) and $t = 0.5s$ (right). The wildtype data is shown in blue, the GOF mutant in orange and the KO mutant in green. The different swimmer concentrations are indicated by the marker symbols. As reference, the black line marks the theoretical curve for free diffusing tracers.

model, keeping the diffusion constant fixed at $D = 0.68\mu m^2/s$. We choose a swimmer velocity of $v = 10\mu m/s$ account for the positive skewness of the distribution. Since λ_f is the rate at which a free tracer will encounter a swimmer, we expect λ_f to be proportional to the swimmer concentration c, the swimmer speed v and the interaction cross section A. We expect that v and A remain constant under all observed conditions and vary the concentration c to observe different values of λ_f. In addition to λ_f, we have to estimate the interaction rate λ_i based on a fit to the experimental data. Due to the lack of an analytical expression for the displacement distribution $P(x,t)$, we have to rely on numerical simulations to model $P(x,t)$ based on histograms, using the same bins as for the experimentally obtained histograms. By the means of least-square optimization, we estimate λ_f and λ_i for the different experimental conditions. For each condition, the data is fitted for the time lags of $\Delta t = 0.1s,\ 0.3s$ and $0.5s$. These results are listed in table 3.2 and a selection of fits are plotted in figure 3.18 and in the appendix 5.3,5.4. The central part of the fitted numerical models are in good agreement with the experimental data, but the tails are limited due to the swimmer velocity of $v = 10\mu m/s$. Comparing λ_f for the different concentrations of the same strain doesn't show the expected linear relation, probably due to the negligible differences between the concentration in the experimental data. We continue our analysis by computing the mean squared displacement from the tracer trajectories for the different experimental conditions. The results are plotted in figure 3.19. Both the wildtype and the KO mutant show a nearly linear increase over the observed times, while the MSD curve of the GOF mutant displays a change in the slope similar to the theoretical MSD curves in figure 3.9. We use formula (3.88) to fit the MSD curves numerically and summarize the resulting fit parameters in table 3.2.

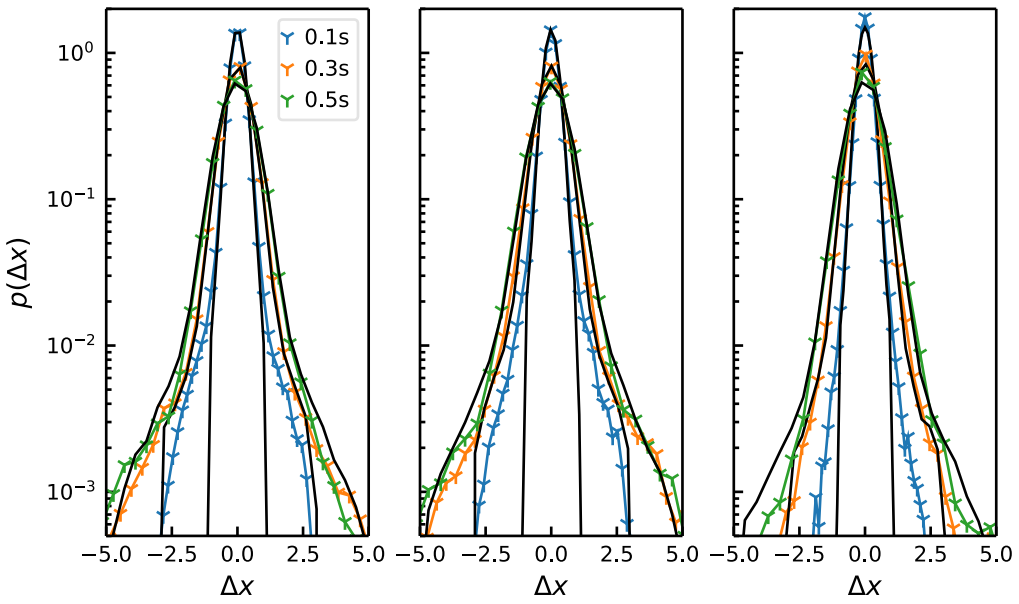

Fig. 3.18: Distribution of tracer displacements for different swimmer concentrations of the GOF strain of *S. Putrefaciens* and corresponding numerical CTRW fits. The data for the base concentration is shown in the left image, the double concentrated in the center and the tracer displacements for the four fold concentrated swimmers are shown to the right. The displacements are calculated for three time intervals of $\Delta_t = 0.1s$, $\Delta_t = 0.3s$ and $\Delta_t = 0.5s$. The fit parameters are listed in table 3.2.

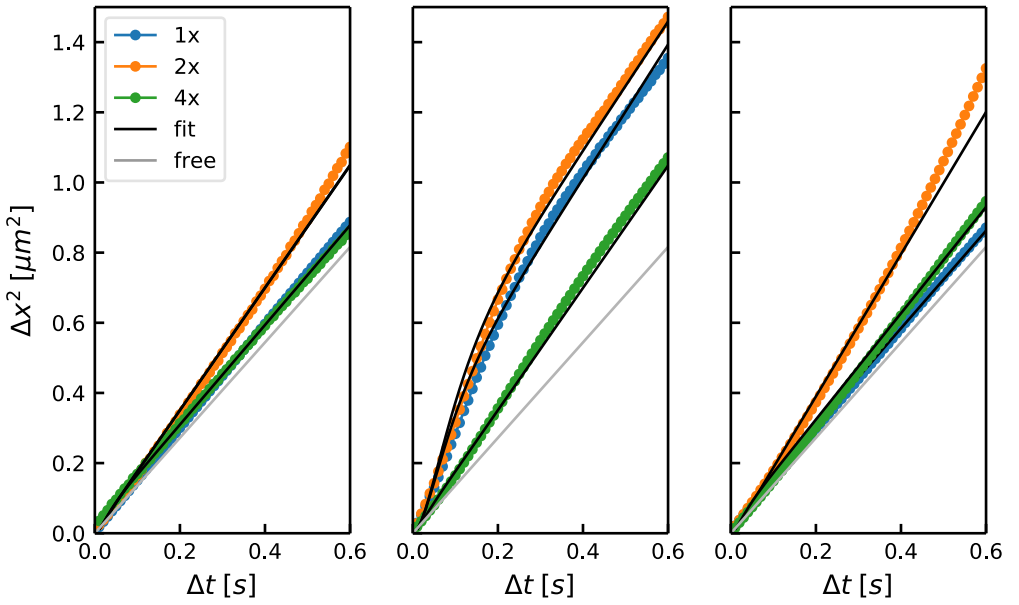

Fig. 3.19: Mean squared displacement of tracer displacement for different swimmer strains and concentrations. The wildtype strain is shown in the left column, the GOF mutant in the middle and the KO mutant to the right. The fits to the MSD curve of the mixed CTRW model 3.88 are shown in black and the values of the corresponding parameters are listed in table 3.2. As reference, the theoretical MSD curve for free diffusing tracer beads is displayed in gray.

		Histogram		MSD	
Strain	rel. conc.	$\lambda_i\ [s^{-1}]$	$\lambda_f\ [s^{-1}]$	$\lambda_i\ [s^{-1}]$	$\lambda_f\ [s^{-1}]$
Wildtype	1x	15.50	0.35	62.29	2.11
Wildtype	2x	16.21	1.10	63.91	17.21
Wildtype	4x	15.74	0.05	64.21	18.10
GOF	1x	4.87	0.25	19.55	1.17
GOF	2x	5.01	0.31	22.11	1.72
GOF	4x	4.82	0.15	55.29	14.53
KO	1x	16.61	0.63	62.98	1.14
KO	2x	16.63	1.42	66.32	45.2
KO	4x	16.02	0.85	60.52	5.12

Tab. 3.2: Fit parameters obtained by fitting the numerical model to experimentally obtained histograms as well as parameters obtained by fitting (3.88) to the measured mean squared displacement curves. The free diffusion coefficient of the tracers was fixed to $D = 0.68\mu m^2/s$ and the swimmer velocity was set to $v = 10\mu m/s$.

$\phi\ [\%]$	$\lambda_i\ [s^{-1}]$	$\lambda_f\ [s^{-1}]$	$D_{eff,fit}\ [\mu m^2/s]$	$D_{eff,exp}\ [\mu m^2/s]$
0.4	99.30	0.75	1.03	0.52
0.8	97.21	1.51	1.85	0.76
1.6	105.20	3.03	2.93	1.46
2.2	101.29	4.13	4.14	2.01
comb.	102.8	1.875ϕ	–	$0.23 + 81.3\phi$

Tab. 3.3: Fit parameters and effective diffusion constants for data from Leptos et al. The effective diffusion coefficients $D_{eff,fit}$ and $D_{eff,leptos}$ were obtained from equation (3.82) and figure 2 in Leptos et al., 2009.

In addition to our own measurements, we fit the mixed model to the distribution obtained by Leptos et al. Leptos et al., 2009. The authors performed multiple tracking experiments with $1\mu m$ sized microspheres as tracer particles and different concentrations of *Chlamydomonas reinhardtii*, a spherical green alga, as swimmer organism. Using the quoted diffusion constant of $D_0 = 0.28\mu m^2/s$ and a cell speed of $v = 100\mu m/s$, we again fit the parameters λ_f and λ_i of the mixed model to the step size distribution, which was obtained by digitizing figure 2 in Leptos et al., 2009. The resulting values are listed in 3.3. In addition to the individual fits, we estimate λ_i and λ_f for all concentrations in parallel, where λ_f was set to $\lambda_{free,c} = c_i\lambda_{free,0}$ with $c_i = 1, 2, 4, 5.5$ to include the different swimmer concentrations.

The mean squared displacement measured by Leptos et al. increases linearly with $\langle r^2\rangle \approx 2D_{eff}t$ over the observation period, which seems to contradict the results of our model at first, but is again explained by the small time scales at which the transition from ballistic to diffusive spreading happens in our model. Calculating the diffusion constants D_{mixed} using the estimated parameters from the combined fit, we observe a good agreement with the effective diffusion constants denoted by Leptos et al.

3.5 Conclusion

Although based on relative simple assumptions, the continuous time random walk model presented in this chapter offers a powerful framework to study the statistics of an ensemble of tracer particles in a solution of active swimmers. We have derived an analytical expression for

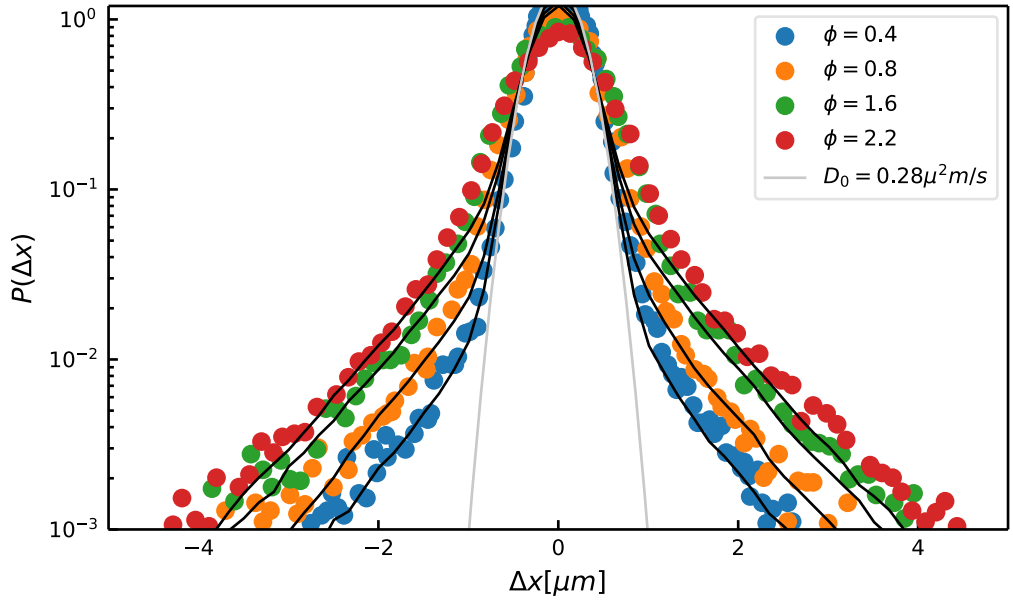

Fig. 3.20: Experimentally obtained step size distributions from Leptos et al. Leptos et al., 2009 for different concentrations of *C. reinhardtii* and corresponding numerical fits of the mixed model.

the mean squared displacement of the tracer displacement in one, two and three dimensions an were able to test this expression against the experimentally measured MSD curves for fluorescent tracer beads in solutions of different strains of *S. Putrefaciens*. We have shown that the model can reproduce the experimentally obtained tracer displacement distribution curves from our own experiments as well as the distributions measured by Leptos et al. over different swimmer concentrations.

4 Diffusion on cell surfaces

4.1 Introduction

Recent developments in high resolution imaging allow to track the diffusion of surface proteins with high temporal and spatial resolution. Wildenberg et al., 2011; Moerner and Fromm, 2003; Deich et al., 2004; Yu, 2006; Marguet et al., 2006; Elf et al., 2007 To a good approximation, the basic problem is homogeneous diffusion on a cylindrical surface, and an easy exercise in diffusion. Problems arise from the projection onto an observation plane which introduces inhomogeneities that are of a geometric nature.

We here discuss the basic time scales and the phenomenology of observations of diffusion on a cylinder with a view towards observations of diffusing surface proteins. After a discussion of the mathematical side of the problem, we compare our findings to observations on *Bacillus subtilis*.

4.2 Surface diffusion on a cylinder

The probability density functions (pdf) for diffusion on a cylinder is a product of the pdf for diffusion around the circumference and along the axis z. The first process runs into saturation, with a uniform distribution around the circumference, while the second one shows the usual diffusive spreading.

To further analyze this process, we formulate the probability density function for the displacements at time t. Diffusion along the axis is governed by

$$p(z,t) = \frac{1}{\sqrt{4\pi D_0 t}} e^{-\frac{(z-z_0)^2}{4D_0 t}}, \tag{4.1}$$

with D_0 the molecular diffusion constant and z_0 the initial position of the source. For diffusion around the circumference, we express $p(z,t)$ in terms of the azimuthal angle ϕ,

$$p(\phi,t) = \frac{1}{\sqrt{2\pi D_R t}} e^{-\frac{(\phi-\phi_0)^2}{2D_R t}}, \tag{4.2}$$

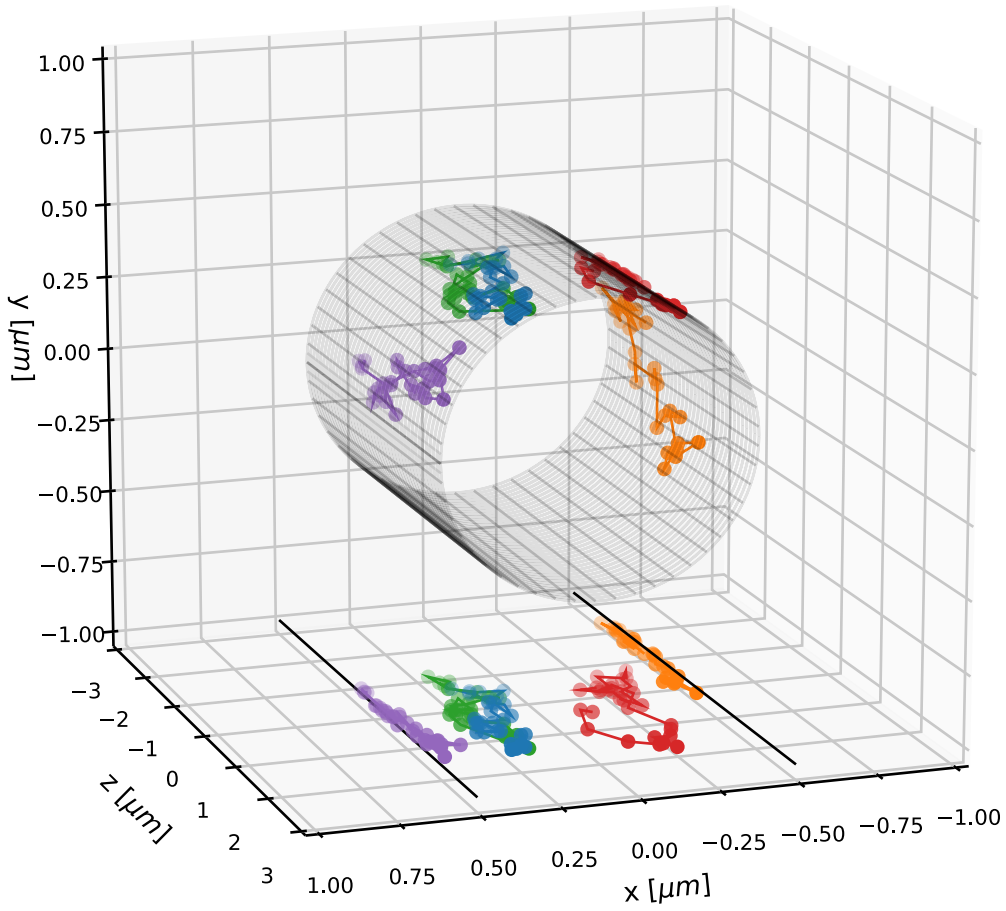

Fig. 4.1: Isotropic surface diffusion on a cylinder with radius $r = 0.5\mu m$. The trajectories were simulated using a random walk with normally distributed step sizes. The diffusion coefficient was set to $D = 4\mu m^2/s$ and the trajectories were sampled at a frequency of $100Hz$. To illustrate the effects of the projection and the resulting anisotropy in the observed tracks, the projection of the 3D trajectories onto the x-z-plane is also shown.

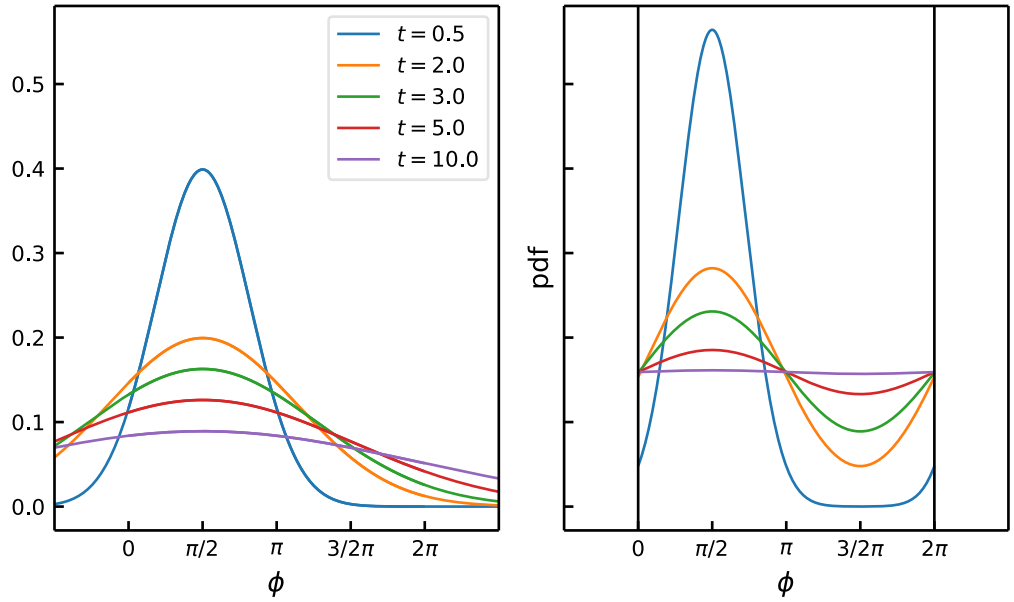

Fig. 4.2: Left: Probability density function for a normal distribution with $\mu = \pi/2$, $\sigma^2 = D_R t$ and $D_R = 1/s$ for different times. Right: Wrapped normal distribution with the same parameters, illustrating diffusion around the circumference of a cylinder and the effects of the periodicity.

where ϕ is defined on the domain $(-\infty, \infty)$ and the radial diffusion coefficient depends on the cylinder radius R, with $D_R = 2D_0/R^2$. Transferring the process to the domain $(0, 2\pi)$ using the relation $p_w(\phi, t) = \sum_{k=-\infty}^{\infty} p(\phi + 2\pi k, t)$ results in the wrapped distribution

$$p_w(\phi, t) = \frac{1}{\sqrt{2\pi D_R t}} \sum_{k=-\infty}^{\infty} e^{-\frac{(\phi-\phi_0+2\pi k)^2}{2D_R t}} \tag{4.3}$$

As depicted in figure 4.2, the probability density function undergoes diffusive spreading at short timescales and approaches a uniform distribution at longer timescales when the effects of the periodicity come into play.

4.2.1 Surface diffusion in projection

Although recent developments in microscopy allow the measurement of the 3D positions of fluorescently labeled proteins Shashkova and Leake, 2017, most of these techniques do not offer the required temporal resolution to track proteins reliably. Hence it is necessary to track the proteins using two-dimensional imaging techniques, where the 3D positions of objects within a small region above and below the focal plane are projected onto the camera sensor, thereby loosing the information about the third dimension.

The pdf of the step size distributions in this observation plane follows by projection with $x = R\cos\phi$, with the two possible values for $\phi_\pm(x) = \pm\cos^{-1}(x/R)$, where $\cos^{-1}$ has values in $(0, \pi)$. As illustrated in figure 4.1 This introduces a singularity from projections, such that a uniform distribution on the surface becomes non-uniform in the plane with a singularity

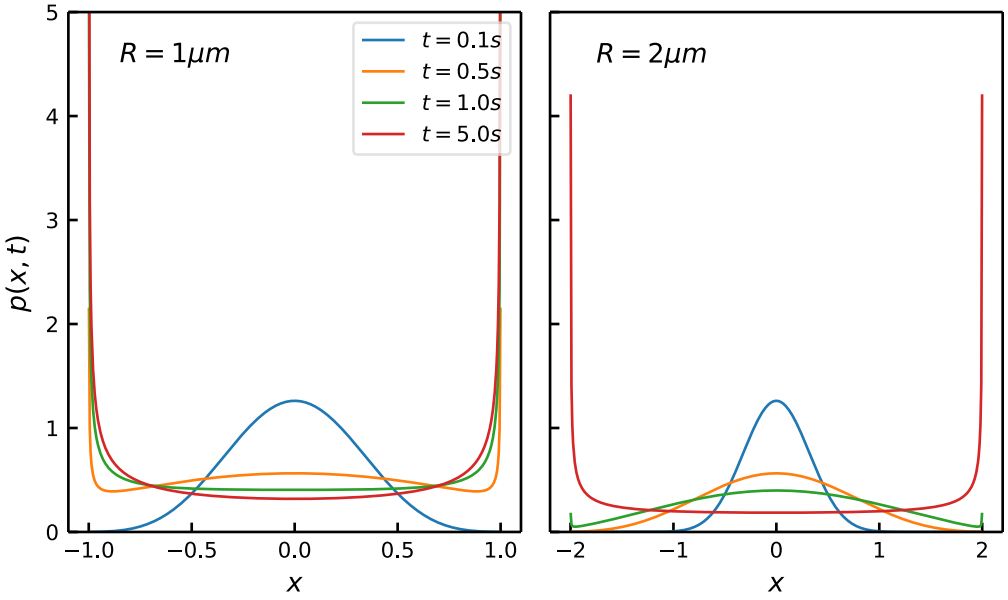

Fig. 4.3: Probability density function for the azimuthal diffusion process in the projection onto the x-z plane, for $D_0 = 1\mu m^2/s$, $x_0 = 0$ and different radii.

near $x = \pm R$. Using the change-of-variable technique, we can derive the pdf for the diffusion process in the plane of projection. We find

$$p(x,t) = \left|\frac{d}{dx}\phi_-(x)\right| p_w(\phi_-(x)) + \left|\frac{d}{dx}\phi_+(x)\right| p_w(\phi_+(x)) \tag{4.4}$$

$$= \frac{1}{\sqrt{2\pi D_R t}} \frac{1}{\sqrt{R^2 - x^2}} \sum_{k=-\infty}^{\infty} \left(e^{\frac{-(\cos^{-1}(x/R) - \phi_0 - 2\pi k)^2}{2D_R t}} + e^{\frac{-(-\cos^{-1}(x/R) - \phi_0 + 2\pi k)^2}{2D_R t}} \right). \tag{4.5}$$

As pointed out above, for long observation times ($t \to \infty$) the distribution $p_w(\phi, t)$ asymptotically approaches a uniform distribution with $p_u(\phi) = 1/2\pi$ and the observed distribution of surface proteins in the projection plane is

$$p_u(x) = \left|\frac{d}{dx}\phi_-(x)\right| (p_u(\phi_-(x)) + p_u(\phi_+(x)) \tag{4.6}$$

$$= \frac{1}{\pi\sqrt{R^2 - x^2}}, \tag{4.7}$$

with singularities at both $-R$ and R.

In order to characterize the diffusion process over time, we now calculate the first and second moment of the distribution. More generally, the n-th moment is given by

$$\langle x^n \rangle = \frac{1}{\sqrt{2\pi D_R t}} \int_{-R}^{R} \frac{x^n}{\sqrt{R^2 - x^2}} \sum_{k=-\infty}^{\infty} \left[e^{\frac{-(\cos^{-1}(x/R) - \phi_0 - 2\pi k)^2}{2D_R t}} + e^{\frac{-(\cos^{-1}(x/R) + \phi_0 - 2\pi k)^2}{2D_R t}} \right] \tag{4.8}$$

By substituting $x = R\cos(\phi)$ and regrouping the sum to evaluate the integral from $-\infty$ to ∞, the above expression simplifies to

$$\langle x^n \rangle = \frac{R^n}{\sqrt{2\pi D_R t}} \int_{-\pi}^{\pi} \cos^n(\phi) \sum_{k=-\infty}^{\infty} e^{\frac{-(\phi-\phi_0-2k\pi)^2}{2D_R t}} d\phi \tag{4.9}$$

$$= \frac{R^n}{\sqrt{2\pi D_R t}} \int_{-\infty}^{\infty} \cos^n(\phi) e^{\frac{-(\phi-\phi_0)^2}{2D_R t}} d\phi \tag{4.10}$$

To calculate the first moment, we use the definition of the characteristic function χ_p of a probability distribution $p(x)$, which is just its Fourier transform,

$$\chi_p = \int_{-\infty}^{\infty} e^{-ixk} p(x) dx \tag{4.11}$$

$$= \int_{-\infty}^{\infty} (\cos(xk) + i\sin(xk)) p(x) dx. \tag{4.12}$$

We obtain

$$\langle x \rangle = \frac{R}{\sqrt{2\pi D_R t}} \int_{-\infty}^{\infty} \cos(\phi) e^{\frac{-(\phi-\phi_0)^2}{2D_R t}} d\phi \tag{4.13}$$

$$= \frac{R}{\sqrt{2\pi D_R t}} \text{Re}\left(\int_{-\infty}^{\infty} e^{-i\phi} e^{\frac{-(\phi-phi_0)^2}{2D_R t}} d\phi \right) \tag{4.14}$$

$$= R\text{Re}\left(e^{i\phi_0 - D_R t/2} \right) \tag{4.15}$$

$$= R\cos(\phi_0) e^{-D_R t/2} \tag{4.16}$$

Using the same approach, we can derive the second moment,

$$\langle x^2 \rangle = \frac{R^2}{\sqrt{2\pi D_R t}} \int_{-\infty}^{\infty} \cos^2(\phi) e^{\frac{-(\phi-\phi_0)^2}{2D_R t}} d\phi \tag{4.17}$$

$$= \frac{R}{\sqrt{2\pi D_R t}} \int_{-\infty}^{\infty} \frac{1+\cos(2\phi)}{2} e^{\frac{-(\phi-\phi_0)^2}{2D_R t}} d\phi \tag{4.18}$$

$$= \frac{R^2}{2} \left(1 + \text{Re}\left(e^{2i\phi_0 - D_R t} \right) \right) \tag{4.19}$$

$$= \frac{R^2}{2} \left(1 + \cos(2\phi_0) e^{-D_R t} \right). \tag{4.20}$$

Combining both results, it is easy to calculate the variance $Var(x,t) = \langle x^2 \rangle(t) - \langle x \rangle^2(t)$ of the projected diffusion process,

$$Var(x,t) = \frac{R^2}{2} \left(1 - e^{-D_R t} \right). \tag{4.21}$$

Another interesting property is the mean squared displacement (msd) $d_x(\tau) = \langle (x(\tau) - x_0)^2 \rangle$, which is often used to experimentally determine the diffusion constant. With $x_0 = R\cos(\phi_0)$, the msd with respect to x is given by

$$d_x(\tau, \phi_0) = \langle x^2 \rangle + x_0^2 - 2x_0 \langle x \rangle \tag{4.22}$$

$$= R^2 \left(1 - e^{-D_R t/2} \right) + \frac{R^2}{2} \cos(2\phi_0) \left(1 - e^{-D_R t/2} \right)^2. \tag{4.23}$$

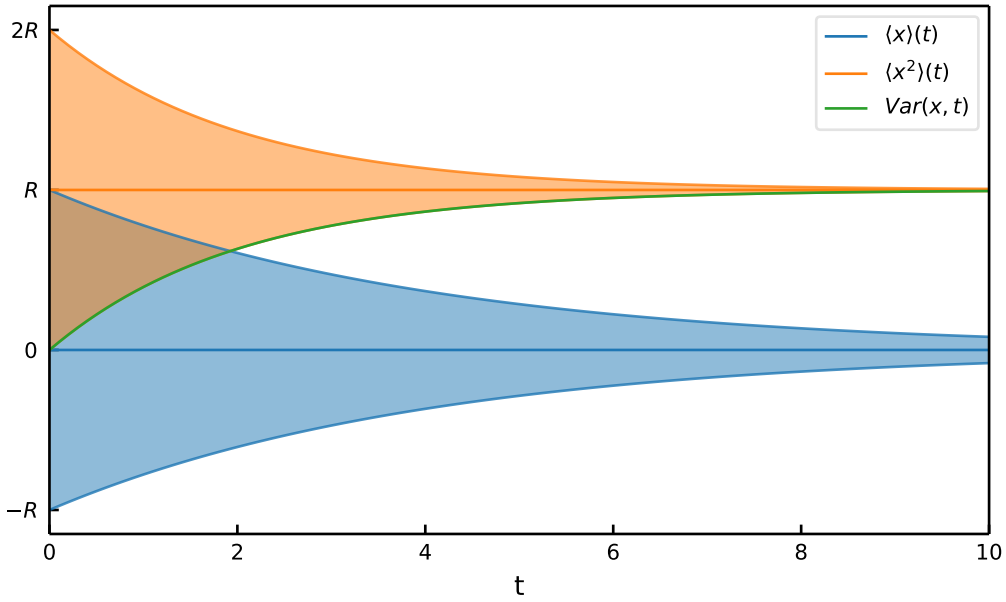

Fig. 4.4: Change of mean $\langle x \rangle(t)$, second moment $\langle x^2 \rangle(t)$ and variance $\langle (x - \langle x \rangle)^2 \rangle(t)$ over time. Both mean and second moment depend on the initial angle ϕ_0 and the upper and lower bound correspond to $\phi_0 = 0$ resp. $\phi_0 = \pi$ for $\langle x \rangle(t)$ and to $\phi_0 = 0$ resp. $\phi_0 = \pi/2$ for $\langle x^2 \rangle(t)$. The variance is independent of ϕ_0.

Experimentally, the msd is obtained by combining the data of many independent tracks which in our case amounts to averaging (4.23) over the initial angle ϕ_0,

$$\langle d_x(\tau, \phi_0) \rangle_{\phi_0} = R^2 \left(1 - e^{-D_R t/2}\right). \tag{4.24}$$

Both the variance and d_x will asymptotically approach a constant value of $Var(x)_\infty = R^2/2$ respectively $d_x = R^2$, which does not include any information about the diffusion coefficient D_0. For fast diffusing particles this may lead to a high uncertainty for the estimation of D_0, since for a low temporal sampling frequency the timespan until $Var(x) \approx R^2$ or $d_x \approx R^2$ might be too short to estimate D_0 reliably. To overcome this limitation, one might measure the diffusion along the cell axis only, which is not influenced by the cell curvature. A drawback of this approach is the dependence on the cell orientation, which has to be measured separately to reliably distinguish azimuthal and axial motion. To include both directions into the estimation of D_0 one can calculate the mean squared displacement in the x-z-plane, which additionally eliminates the necessity to measure the cell orientation. The mean squared displacement is derived as follows:

$$d_r(\tau, \phi_0) = \langle (x(\tau) - x_0)^2 \rangle + \langle (z(\tau) - z_0)^2 \rangle \tag{4.25}$$

$$= R^2 \left(1 - e^{-2D_0 t/2R^2}\right) + \frac{R^2}{2} \cos(2\phi_0) \left(1 - e^{-2D_0 t/2R^2}\right)^2 + 2D_0 t \tag{4.26}$$

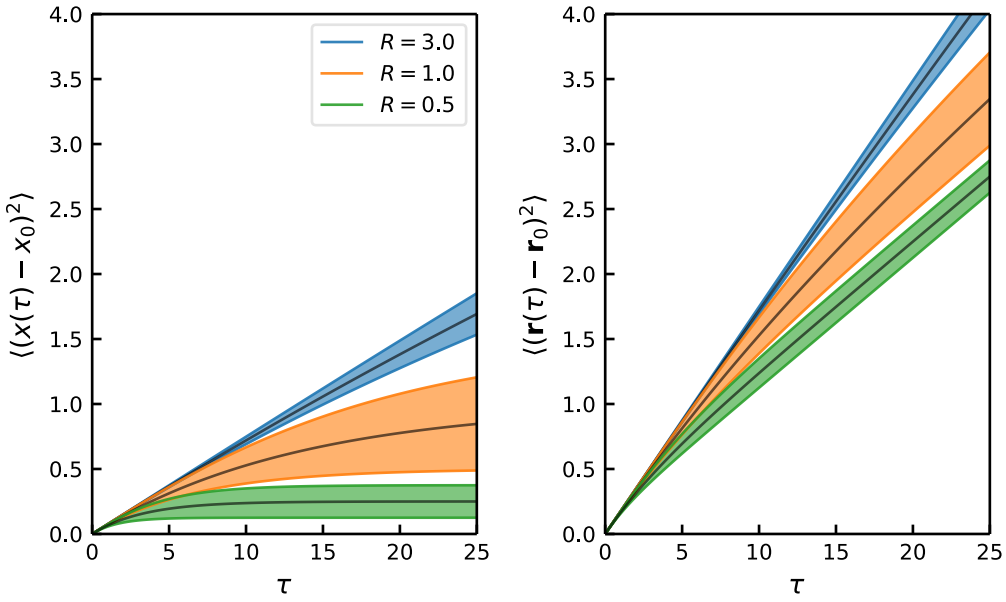

Fig. 4.5: Mean squared displacement for projected diffusion in radial direction only (left) and in the x-z-plane (right). The diffusion coefficient is fixed to $D_0 = 0.1$. The upper and lower bound for each curve correspond to $\phi_0 = 0$ resp. $\phi_0 = \pi/2$, while the dashed line marks the case of $\phi_0 = \pi/4$ which is equal to the mean squared displacement averaged over ϕ_0.

Assuming that d_r is calculated using a combination of multiple tracks, we can again average over ϕ_0 and arrive at

$$\langle d_r(\tau, \phi_0)\rangle_{\phi_0} = R^2 \left(1 - e^{-2D_0 t/2R^2}\right) + 2D_0 t \tag{4.27}$$

For long observation times the d_r can be linearly approximated with a slope of $2D_0$ and an intersect of R^2. On short timescales, we can expand the radial component to $d_x = D_0 t + O(t^2)$ and observe a scaling of $d_r \approx 3Dt$.

Another interesting property of the diffusion process for conditions without any knowledge about the cell orientations is the distribution of the squared step sizes r^2. To estimate the probability density functions $p(r^2, t)$ we rely on numerical simulations. In a first step, a sample of $N = 10000$ two-dimensional random walks with 100 steps is generated. The individual steps in x and y direction are drawn from a normal distribution with $\mu = 0$ and $\sigma^2 = 2D_0\tau$. The tracks are then mapped on the surface of a cylinder with radius R and in a final step projected onto the focal plane. For the resulting tracks we estimate $p(r^2, t)$ by computing a histogram of the square step sizes $r^2(t)$. The results for a cylinder with $R = 1\mu m$ are shown in figure 4.6. Compared to the pdf for free diffusion $p(r^2, t)_{free}$ which is given by the χ^2_2-distribution scaled with $2D_0 t$, the pdf for the projected displays increased probabilities for small step sizes.

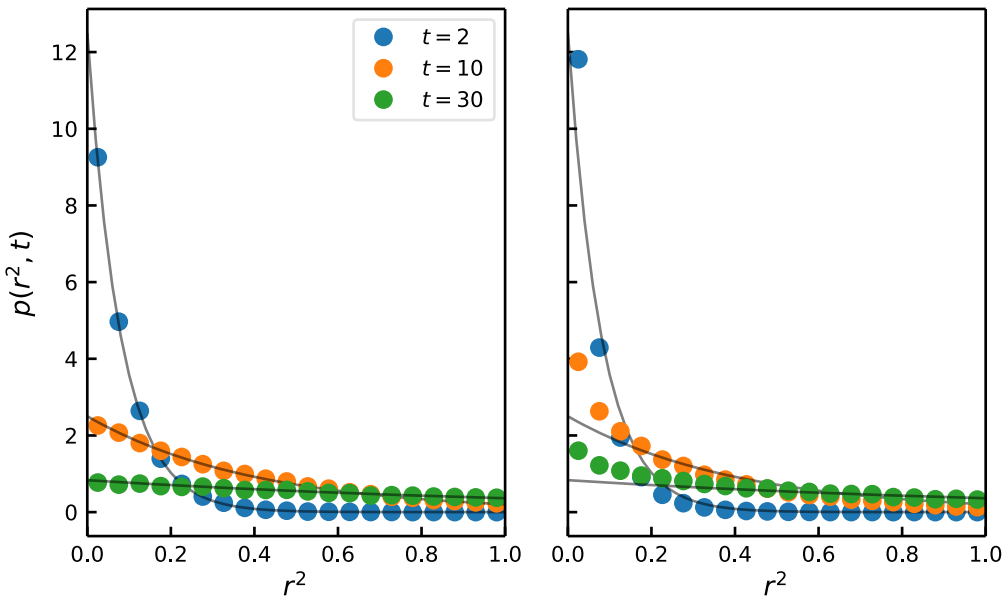

Fig. 4.6: Histograms to estimate the probability density function for the squared displacement d_R for free diffusion with $D_0 = 0.01\mu m^2/s$ in the plane (left) and diffusion on a cylinder with $R = 1\mu m$. The black lines indicate the χ^2_2 distribution scaled with $2D_0t$.

4.3 Relation to experiments

Under experimental conditions, the focus of the microscope is limited and only a small layer at a certain height of the cell is observable. This limits the area where surface proteins can be tracked. Moreover, the total observation time for a single particle is limited as well since it will eventually leave the focal plane. To decide whether to place the focus on top of the cell or in the midplane, we calculate the accessible azimuthal angle ϕ for both strategies and a focus height of H,

$$\phi_{Top} = \pi - 2\sin^{-1}((R-H)/R), \tag{4.28}$$

$$\phi_{Mid} = 4\sin^{-1}(H/2R). \tag{4.29}$$

The results a illustrated in figure 4.7. For the midplane, the observable angle is split into two parts. Hence, the time a particle spends in one of both parts is significantly shorter.

To estimate how the available angle ϕ influences the observable time, we extend our previous simulation to include the effect of a limited focus and end all tracks as soon as they run out of focus. The number of remaining tracks over time is plotted in figure 4.8. As expected, setting the focus in the midplane of the cell, significantly shortens the observation time.

We also examine the effect of the limited focus height on the observed mean squared displacement. From the previous results it is already clear that in addition to experimental factors like photobleaching, the observation time for a single trajectory is limited due to the focus. With the decreasing number of tracks for longer time lags, the uncertainty in

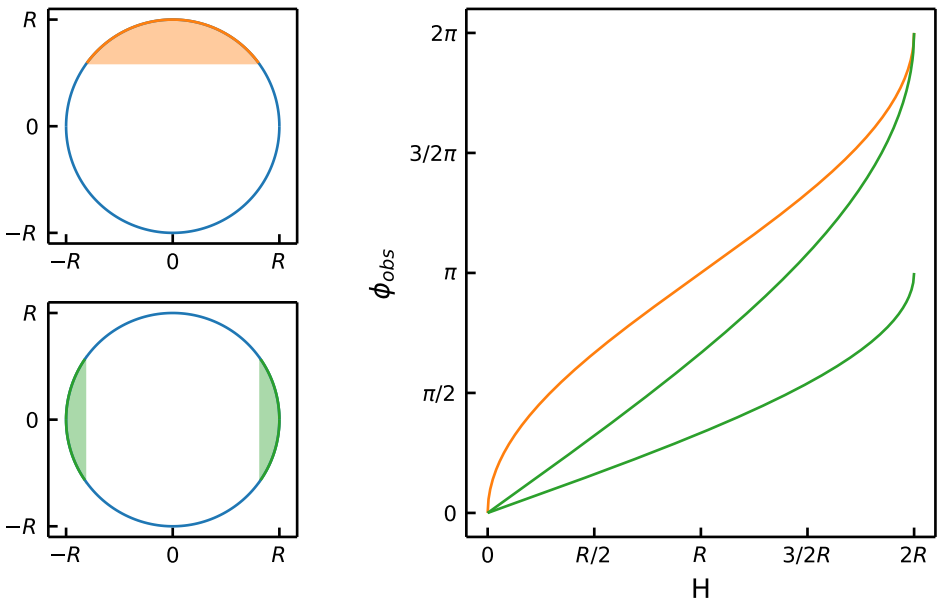

Fig. 4.7: Observable region of the cell surface for a fixed depth of field H. Setting the focus on top of the cell (orange) result in a larger observable angle ϕ_{obs} and hence a prolonged observation time. Setting the focus to the midplane results in a smaller ϕ_{obs} (dashed green line). In addition the observable angle is split into two parts (solid green line), reducing the time a particle is observable even further.

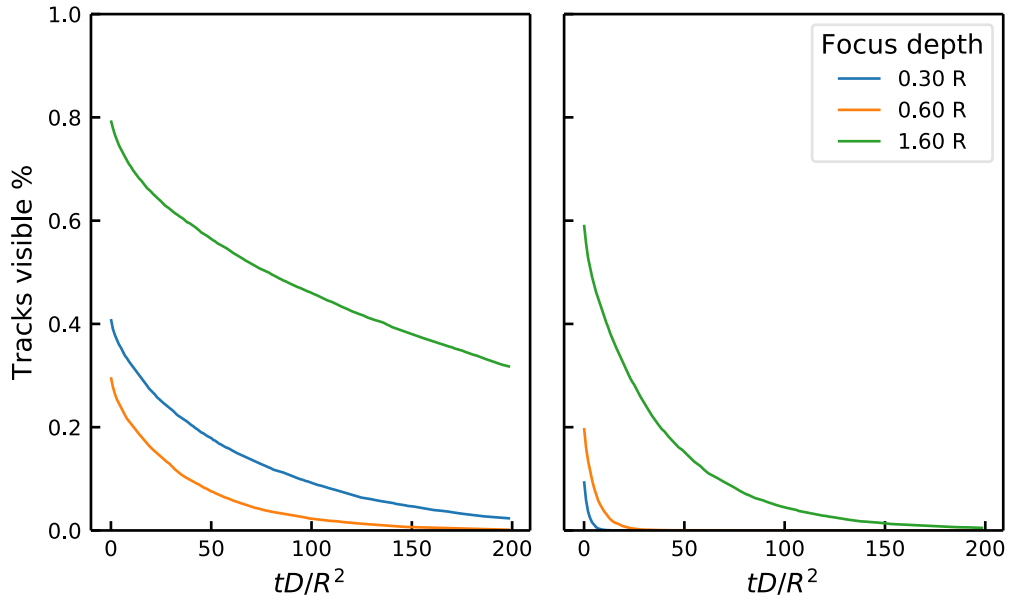

Fig. 4.8: Percentage of observed tracks over time for different depths of field, with the focus set on the top of the cell (left) and in the midplane (right).

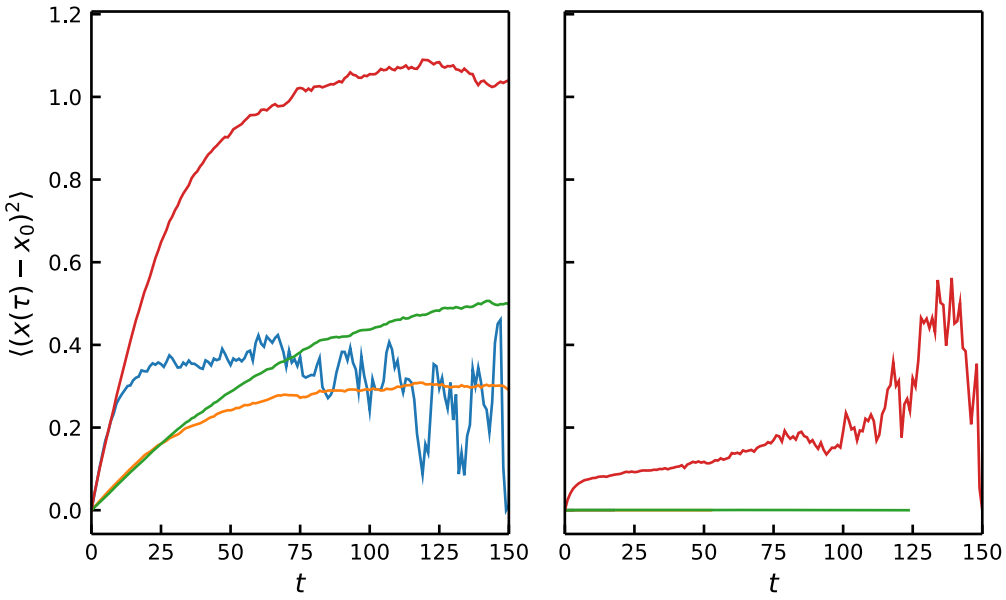

Fig. 4.9: Radial mean squared displacement with limited focus height.

the mean squared displacement increases and complicates the estimation of the diffusion coefficient.

In addition to the limited observation time, the focus height also introduces a bias in the radial motion. For the case where the focus is placed on the top of the cell, the particle can be observed over a relatively wide range of x, while for the second observation strategy where focus set to the midplane, the range of visible x-positions is quite limited. Using the same numerical setup as for the observation durations, we calculate the mean squared displacements for both strategies using a number of combinations of focus height, cell radius and diffusion coefficient. The results are depicted in figure 4.9. For the midplane observation and a small depth of field H, the increase of the mean squared displacement is very limited, but even for $H = 1.9R$ the curve stays flat compared to the model without focus limitation.

On the whole, the radial motion for a limited focus contributes only little to the combined mean squared displacement of radial and axial motion. Especially for observations in the mid plane of the cell, the observed mean squared displacement is well approximated by one dimensional free diffusion.

To understand the observed effect, we focus on the strategy where the focus is set to the top of the cell. For a focus depth smaller than the cell radius, we observe only particles above the cell mid plane. Consequently, the periodic nature of diffusion on the cylindrical surface does not apply any longer, but the motion is better characterized by a truncated normal distribution with respect to the angle ϕ, where ϕ may assume values between $\phi_{min} > 0$ and $\phi_{max} < \pi$.

In addition to the mean squared displacement, the step size distribution is affected by the limited depth of field as well. Again, the effect is largest for a small depth of field and the

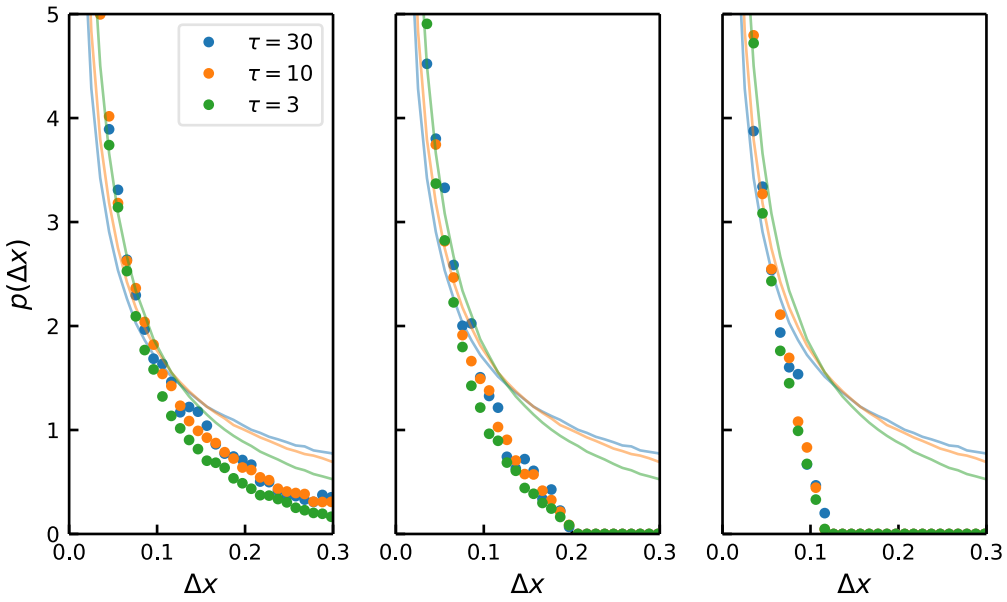

Fig. 4.10: Probability density function for step sizes Δx. The focus is centered on the cell center and the focus depth is $15/16R$ (left), $5/6R$ (middle) and $3/4R$ (right). The observation times are color coded. The cell radius is set to $1\mu m$ and the diffusions coefficient to $0.05\mu m^2/s$. The dashed line indicate the step size distribution with an unlimited focus.

focal plane set to midplane of the cell. For the focus set to the top of the cell, the effect is small and becomes significant only for very small depths of field.

Using the results from above, we seek to find a good strategy to estimate the diffusion coefficient under experimentally relevant conditions. The bacterium *Bacillus subtilis* is often used as a model organism for Gram-positive bacteria in the study of chromosome replication and cell differentiation. It is rod shaped with a typical diameter of $0.87\mu m$ and a length between $2.3\mu m$ and $4.7\mu m$, depending on the growth conditions Weart et al., 2007. To track membrane proteins, different microscopy techniques were developed, which are commonly referred to as single molecule fluorescence microscopy Wildenberg et al., 2011; Shashkova and Leake, 2017. A typical technique within this category is total internal reflection fluorescence microscopy (TIRF), where an evanescent light field is used to stimulate the fluorophores in a thin region on the specimen. Within this region, which has a typical height of up to $400nm$ Martin-Fernandez et al., 2013, single molecules can be tracked on a sub-diffraction-limited level using centroid tracking techniques Weart et al., 2007. A modern detector is capable of capturing images at a rate of 50 to 100 frames per second, depending on the observed area. Using this exemplary setup, we can derive a strategy to estimate the diffusion coefficient for a membrane protein.

The diffusion coefficients of membrane proteins vary over many orders of magnitude, depending on their size as well as their association to the membrane. Slow moving proteins are reported to diffuse with lateral diffusion coefficients as small as $D \approx 10^{-3}\mu m^2/s$, while fast proteins were observed to diffuse with up to $D \approx 10\mu m^2/s$ Knight et al., 2010; Weiß et al., 2013; Berg et al., 2002; Goose and Sansom, 2013; Ramadurai et al., 2009.

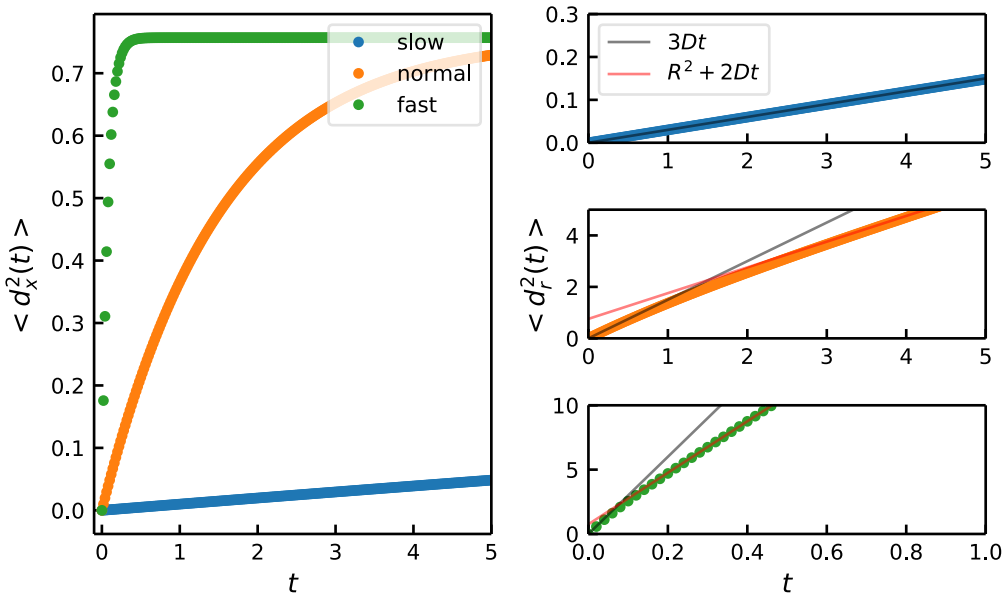

Fig. 4.11: Mean squared displacements for a slow ($D = 0.01\mu m^2/s$), a medium fast ($D = 0.5\mu m^2/s$) and a fast protein ($D = 10\mu m^2/s$)

In a first step we ignore the effects of the limited depth of field and concentrate on the mean squared displacement only. Assuming a maximal observation time of $5s$, we plot (fig. 4.11) d_x and d_r for a slow protein with $D = 0.01\mu m^2/s$, a medium fast protein with $D = 0.5\mu m^2/s$ and a fast protein with $D = 10\mu m^2/s$. For the fast protein the radial component quickly approaches the constant value of R^2 after roughly 10 frames and the mean squared displacement can be approximated by $d_r \approx R^2 + Dt$. The mean squared displacement curve for the slow protein, on the other hand, scales diffusively with $d_r \approx 2Dt$ over the observed time and the effects of the cell curvature are negligible. For the medium fast protein on the other hand, the transition between regular two-dimensional diffusion and curvature induced pseudo 1D diffusion extends over the observed timescale and neither of both linear approximations is an optimal choice. An option to estimate the diffusion coefficient for proteins within this category is a direct least squares fit to the derived equation for d_r (4.27).

To include the effects of a limited depth of field we again calculate the mean squared displacement curves using numerical simulations. We set the focus depth to $H = 0.25\mu m$ and stop each track as soon as the simulated protein leaves the focus. Assuming that for each protein type a group of 250 independent tracks is recorded, we calculate the mean squared displacement for each track and average over the whole population to improve our estimation. In order to check the accuracy of this estimate, we repeat the process 100 times and calculate the mean and standard deviation for all displacement curves. The results are displayed in figure 4.12.

As expected the effects of the limited focus depth on the slow moving protein are almost negligible. In fact, the displacement curve suggests a slightly increased slope compared to the model without focus limitations. This effect is caused by the missing contributions from

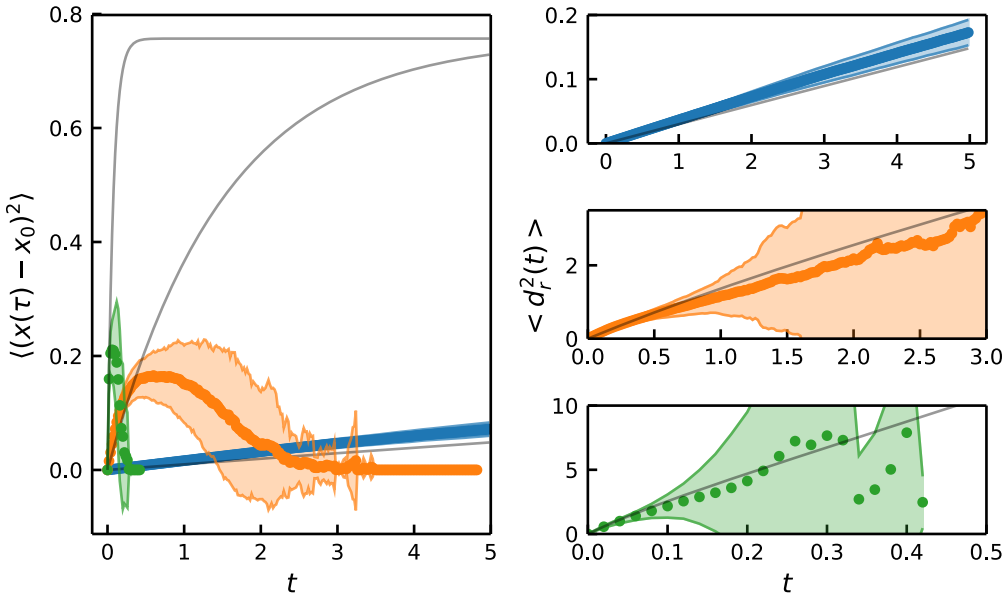

Fig. 4.12: Mean squared displacements for a limited focus depth of $H = 0.25R$ and slow, medium and fast moving proteins. The black line is the mean squared displacement curve for a fully observable cell.

proteins located at $x \approx \pm R$, since radial displacements in these regions are extremely small and lower the overall diffusion rate. For both the medium fast and the fast protein, the departure of proteins from the observable region is significant and leads to a premature stop of the displacement curve with high uncertainties towards the end of the tracks.

4.4 Conclusion

The study of membrane proteins with conventional microscopy techniques requires special care for the analysis. As described above, the cell curvature and a limited focus height have strong effects on the observed radial motion of a particle, which is visible in the mean squared displacement as well as for the step size distribution. To obtain a good estimate of the diffusion coefficient, different strategies for the experimental setup emerge and one has to choose the one best suited for the given conditions.

5 Appendix

5.1 Image analysis

To successfully extract the tracer positions from the images, it is useful to understand how the images a constructed in the first place. The value of each pixel in the image $I(\mathbf{r}_{i,j}, t)$ is a superposition of different effects. The way the light emitted by the fluorescent beads is modified by the microscope is characterized by the objective function $f(\mathbf{r}_{i,j}, t)$. In addition to the actual signal, the image contains a noise signal $R(\mathbf{r}_{i,j}, t)$.

$$I(\mathbf{r}_{i,j}, t) = f(\mathbf{r}_{i,j}, t) + R(\mathbf{r}_{i,j}, t) \tag{5.1}$$

To extract the tracer trajectories from the fluorescence images, the python implementation of the widely used algorithm developed by John Crocker and Eric Weeks was applied Crocker and Grier, 1996; Allan et al., 2016. In a first step, the background noise in the images caused by fluctuations of the individual pixels of CCD chip was removed. To achieve this, the image was convoluted with a Gaussian kernel. A similar approach was used to remove the effects of uneven illumination, namely a boxcar filter. The boxcar filter is a 2D convolution of the image with a matrix filled with ones and normalized by the number of its elements. The combination of both filters is equal to a bandpass, removing both high and low frequencies from the image. The resulting image contains many interference patterns caused by out of focus beads. These ring - like structures have a lower signal strength compared to beads close to the focus layer. To remove them, a threshold filter is applied, setting all pixels below the threshold value to zero and the remaining ones to one. A histogram was calculated over all pixel intensities to identify a suitable threshold level. The remaining non zero values are used as starting points for a fitting procedure to achieve subpixel accuracy. This fitting procedure is based on the assumption that the signal generated by a single bead is shaped like a two dimensional gaussian bell curve. The center of the resulting gaussian is the location of the bead, while the width represents the size of the particle. From these results, only the ones with a width compatible with the beads size was kept. In addition to position and width of the particles, additional features including total brightness, eccentricity and signal to noise ratio were calculated and used to filter spurious detections. The used filter criteria are listed in table 5.1 After the detection step was applied to all images in the time series, the individual detected particles had to be linked to form trajectories. Since the particle trajectories do not follow a specific pattern, but a are rather random, the search strategy for identifying the same particle over a series of images is based on a nearest neighbor search. Starting from the particles position in the previous image, the particle with the smallest euclidean distance to this position is selected as candidate. If the distance between both position is below the maximal reasonable step size, the position is added to the trajectory. The maximal step size was selected to be equal to $15px$, the mean swimmer speed times

Parameter	Value
Gausian kernel size	$2px$
Boxcar kernel size	$100px$
Threshold level	40
Maximal link distance	$8px$
Pixel size	$0.0645\mu m$
Frame duration	$10ms$

Tab. 5.1: The various particle tracking parameters for fluorescent beads and their values.

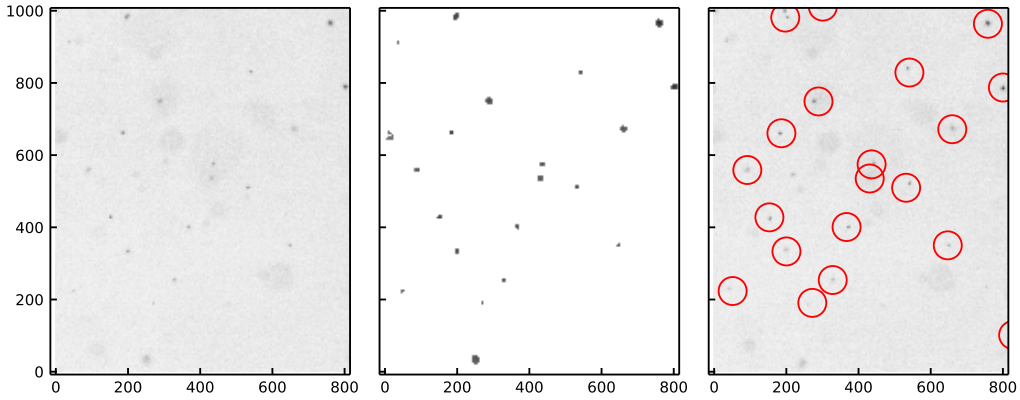

Fig. 5.1: Example of captured raw image with fluorescent tracer beads (left). Image after applying background and noise filtering as well as thresholding (center). Tracer particles detected by algorithm(right).

the frame duration. In order to obtain good statistics, only trajectories with more than 30 consecutive observations were kept.

The swimmer cells were imaged using differential interference contrast (DIC) microscopy, a technique that enhances the visibility of nearly transparent specimen like bacteria Murphy and Davidson, 2012. A drawback of this technique is the seemingly three-dimensional contour that is added to the imaged objects and can pose difficulties to standard object detection algorithms. To overcome these limitations we modified the algorithm presented above and include an additional preprocessing step. Since the observed cells are only roughly ten pixels wide and the DIC technique brightens the one part of the cell outline and darkens the opposite, the use of a gradient filter on the images marks the cells as regions of hight gradient. These modified image pose a good starting point for the standard algorithm presented above, since cells are converted to bright spots similar to the fluorescent beads in focus.

Swimmers trajectories were estimated with the same algorithm as for the passive tracers, but with a larger value for the maximal step size. The different tracking parameters are listed in table 5.2 In order to identify active and inactive swimmers. The mean squared displacement for each swimmer trajectory was calculated. For active swimmers we expect the MSD to follow $< x^2 >= kt^\alpha$ with $\alpha \approx 2$ and consequently keep only swimmer trajectories with $\alpha > 1.7$.

Parameter	Value
Gaussian kernel size	$2px$
Boxcar kernel size	$100px$
Gradient disk size	$5px$
Threshold level	100
Maximal link distance	$15px$
Pixel size	$0.0645\mu m$
Frame duration	$25ms$

Tab. 5.2: The various particle tracking parameters for swimmer cells and their values.

5.2 Experimentally observed characteristics of the flagellum of *Shewanella Putrefaciens*

In addition to the diameter and the pitch of the flagella shown in figure 2.12 we here list the geometrical parameters axial length and contour length of the different strain of *Shewanella Putrefaciens* that were used in section 2. The results are visualized in figure 5.2. The analysis is based on a sample of 50 individual cells for each strain.

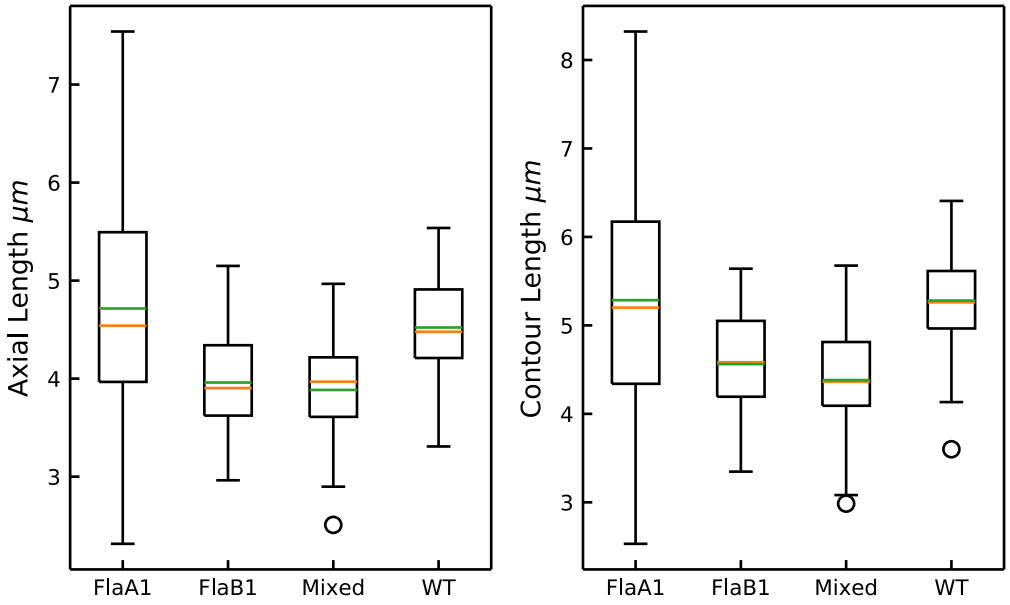

Fig. 5.2: Box-and-whisker plot of the experimentally observed axial and contour length of the flagella for the different strains of *Shewanella Putrefaciens* used in section 2. The median and mean are indicated by yellow and green lines. Data was provided by M. Kühn Kühn et al., 2017; Kühn et al., 2018.

5.3 Tracer displacement distributions

For completeness, we here list the distributions of the tracer displacements and the corresponding numerical fits.

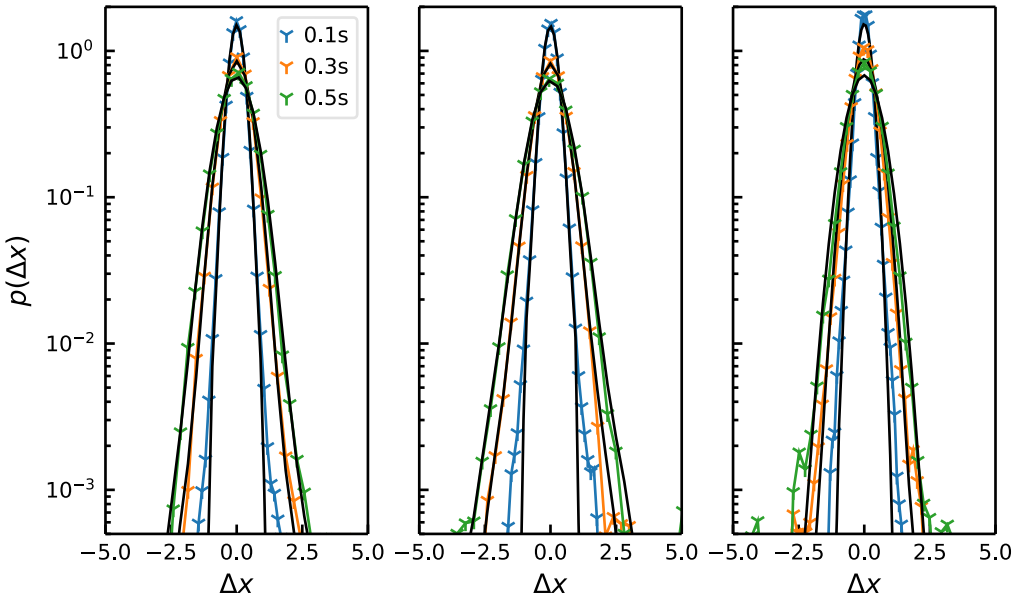

Fig. 5.3: Distribution of tracer displacements for different swimmer concentrations of the wildtype strain of *S. Putrefaciens* and corresponding numerical CTRW fits. The data for the base concentration is shown in the left image, the double concentrated in the center and the tracer displacements for the four fold concentrated swimmers are shown to the right. The displacements are calculated for three time intervals of $\Delta_t = 0.1s$, $\Delta_t = 0.3s$ and $\Delta_t = 0.5s$. The fit parameters are listed in table 3.2.

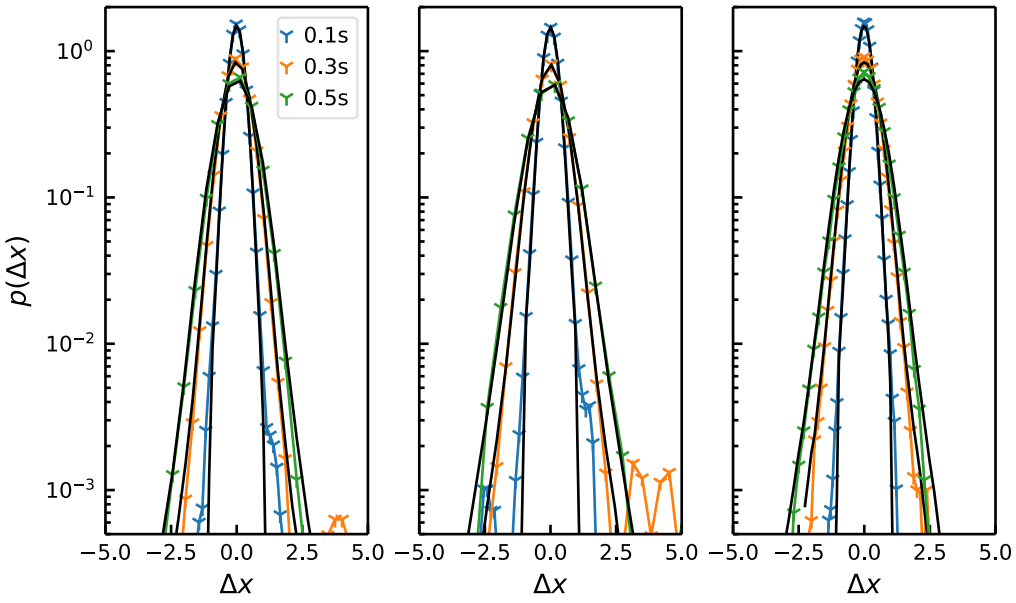

Fig. 5.4: Distribution of tracer displacements for different swimmer concentrations of the KO mutant of *S. Putrefaciens* and corresponding numerical CTRW fits. The data for the base concentration is shown in the left image, the double concentrated in the center and the tracer displacements for the four fold concentrated swimmers are shown to the right. The displacements are calculated for three time intervals of $\Delta_t = 0.1s$, $\Delta_t = 0.3s$ and $\Delta_t = 0.5s$. The fit parameters are listed in table 3.2.

List of Publications

6

6.1 Related to this Work

Marco J. Kühn, Felix K. Schmidt, Bruno Eckhardt, Kai M. Thormann. ”Bacteria exploit a polymorphic instability of the flagellar filament to escape from traps”. In: *Proceedings of the National Academy of Sciences* 114.24 (2017)

Marco J. Kühn, Felix K. Schmidt, Nicola E. Farthing, Florian M. Rossmann, Bina Helm, Laurence G. Wilson, Bruno Eckhardt, Kai M. Thormann. ”Spatial arrangement of several flagellins within bacterial flagella improves motility in different environments”. In: *Nature Communications* 9.1 (2018)

Felix Dempwolff, Felix K. Schmidt, Ana B. Hervás, Alex Stroh, Thomas C. Rösch, Cornelius N. Riese, Simon Dersch, Thomas Heimerl, Daniella Lucena, Nikola Hülsbusch, Claudia A. O. Stuermer, Norio Takeshita, Reinhard Fischer, Bruno Eckhardt, Peter L. Graumann. ”Super Resolution Fluorescence Microscopy and Tracking of Bacterial Flotillin (Reggie) Paralogs Provide Evidence for Defined-Sized Protein Microdomains within the Bacterial Membrane but Absence of Clusters Containing Detergent-Resistant Proteins”. In: *PLOS Genetics* 12.6 (2016)

6.2 Diploma thesis

Felix Schmidt, ”Experiment Design For Parameter Estimation In Gene Regulatory Networks”

Danksagung

Für diese Arbeit schulde ich vielen Menschen einen großen Dank und möchte mich an dieser Stelle ganz herzlich bei ihnen Bedanken. Insbesondere danke ich:

Professor Bruno Eckhardt für die vielen spannenden Diskussionen und Ideen die diese Arbeit erst möglich gemacht haben, sowie für die gute Betreuung während meine Diplomarbeit und der Promotionszeit.

Marco Kühn für die Vorbereitung der Shewanella Stämme und seine Expertise bei der Durchführung der Experimente sowie für die Antworten auf meine vielen Fragen Rund um den experimentellen Aufbau und die Besonderheiten von Shewanella.

Peter Graumann und Kai Thorman für spannende Diskussionen über das Leben von Bakterien im Allgemeinen und die vielen Besonderheiten die man auf Proteinebene antrifft im Besonderen.

Allen früheren und aktuellen Mitglieder der AG komplexe Systeme für das gute Arbeitsumfeld und den Austausch zu vielen spannenden Themen aus verschiedensten Bereichen der Physik. Besonders danke ich dabei Jan Thiede und Tobias Bischoff für ihre kritischen Fragen und das Korrekturlesen dieser Arbeit.

Abschließend möchte ich meiner Familie danken, meinen Eltern, meinem Bruder und Schwiegereltern für die viele Unterstützung. Ein besonderer Dank geht an meine Lieben – Michi, Hannes und Lina – danke, dass ihr immer für mich da seid und mich an die schönen Seiten des Lebens erinnert.

Bibliography

Adhyapak, Tapan Chandra and Holger Stark (2016). „Dynamics of a bacterial flagellum under reverse rotation“. In: *Soft Matter* 12.25, pp. 5621–5629 (cit. on pp. 7, 11).

Adler, J. (1966). „Chemotaxis in bacteria“. In: *Science* 153.3737, pp. 708–716 (cit. on p. 31).

Allan, Daniel, Thomas Caswell, Nathan Keim, and Casper van der Wel (2016). *Trackpy: Trackpy V0.3.2* (cit. on p. 77).

Bar-On, Yinon M., Rob Phillips, and Ron Milo (2018). „The biomass distribution on Earth“. In: *Proceedings of the National Academy of Sciences* 115.25, pp. 6506–6511 (cit. on p. 1).

Berg, H.C. and L. Turner (1993). „Torque generated by the flagellar motor of Escherichia coli“. In: *Biophysical Journal* 65.5, pp. 2201–2216 (cit. on p. 4).

Berg, Howard C. (2003). „The rotary motor of bacterial flagella“. In: *Annual Review of Biochemistry* 72.1, pp. 19–54 (cit. on p. 4).

Berg, Howard C and Douglas A Brown (1972). „Chemotaxis in Escherichia coli analysed by three-dimensional tracking“. In: *Nature* 239.5374, pp. 500–504 (cit. on p. 31).

Berg, Jeremy M., John L. Tymoczko, and Lubert Stryer (2002). *Biochemistry (Chapters 1-34)*. W. H. Freeman (cit. on p. 73).

Bickel, Thomas, Arghya Majee, and Alois Würger (2013). „Flow pattern in the vicinity of self-propelling hot Janus particles“. In: *Physical Review E* 88.1 (cit. on p. 33).

Blake, J. R. (1971). „A spherical envelope approach to ciliary propulsion“. In: *Journal of Fluid Mechanics* 46.01, p. 199 (cit. on p. 33).

Bubendorfer, S., M. Koltai, F. Rossmann, V. Sourjik, and K. M. Thormann (2014). „Secondary bacterial flagellar system improves bacterial spreading by increasing the directional persistence of swimming“. In: *Proceedings of the National Academy of Sciences* 111.31, pp. 11485–11490 (cit. on p. 54).

Calladine, C. R. (1975). „Construction of bacterial flagella“. In: *Nature* 255.5504, pp. 121–124 (cit. on p. 4).

Cash, J. R. and Alan H. Karp (1990). „A variable order Runge-Kutta method for initial value problems with rapidly varying right-hand sides“. In: *ACM Transactions on Mathematical Software* 16.3, pp. 201–222 (cit. on p. 12).

Chen, Xiaobing and Howard C. Berg (2000). „Torque-speed relationship of the flagellar rotary motor of Escherichia coli“. In: *Biophysical Journal* 78.2, pp. 1036–1041 (cit. on p. 4).

Chirico, Giuseppe (1996). „Torsional-bending infinitesimal dynamics of a DNA chain“. In: *Biopolymers* 38.6, pp. 801–811 (cit. on pp. 10, 12).

Cisneros, Luis, Christopher Dombrowski, Raymond E. Goldstein, and John O. Kessler (2006). „Reversal of bacterial locomotion at an obstacle“. In: *Physical Review E* 73.3 (cit. on p. 5).

Coombs, Daniel, Greg Huber, John O. Kessler, and Raymond E. Goldstein (2002). „Periodic chirality transformations propagating on bacterial flagella“. In: *Physical Review Letters* 89.11 (cit. on p. 19).

Coq, N., O. du Roure, J. Marthelot, D. Bartolo, and M. Fermigier (2008). „Rotational dynamics of a soft filament: Wrapping transition and propulsive forces“. In: *Physics of Fluids* 20.5, p. 051703 (cit. on p. 7).

Crocker, John C. and David G. Grier (1996). „Methods of digital video microscopy for colloidal studies“. In: *Journal of Colloid and Interface Science* 179.1, pp. 298–310 (cit. on p. 77).

Dabiri, John O. (2010). „Role of vertical migration in biogenic ocean mixing“. In: *Geophysical Research Letters* 37.11, n/a–n/a (cit. on p. 31).

Darnton, Nicholas C. and Howard C. Berg (2007). „Force-extension measurements on bacterial flagella: triggering polymorphic transformations“. In: *Biophysical Journal* 92.6, pp. 2230–2236 (cit. on pp. 4, 12).

Darwin, Charles (1953). „Note on hydrodynamics“. In: *Mathematical Proceedings of the Cambridge Philosophical Society* 49.02, p. 342 (cit. on p. 31).

Deich, J., E. M. Judd, H. H. McAdams, and W. E. Moerner (2004). „Visualization of the movement of single histidine kinase molecules in live Caulobacter cells“. In: *Proceedings of the National Academy of Sciences* 101.45, pp. 15921–15926 (cit. on p. 63).

Drescher, K., J. Dunkel, L. H. Cisneros, S. Ganguly, and R. E. Goldstein (2011). „Fluid dynamics and noise in bacterial cell-cell and cell-surface scattering“. In: *Proceedings of the National Academy of Sciences* 108.27, pp. 10940–10945 (cit. on p. 33).

Drescher, Knut, Raymond E. Goldstein, Nicolas Michel, Marco Polin, and Idan Tuval (2010). „Direct measurement of the flow field around swimming microorganisms“. In: *Physical Review Letters* 105.16 (cit. on p. 33).

Eckhardt, B. and S. Zammert (2012). „Non-normal tracer diffusion from stirring by swimming microorganisms“. In: *The European Physical Journal E* 35.9 (cit. on p. 32).

Elf, J., G.-W. Li, and X. S. Xie (2007). „Probing Transcription Factor Dynamics at the Single-Molecule Level in a Living Cell“. In: *Science* 316.5828, pp. 1191–1194 (cit. on p. 63).

Fissell, W. H., C. L. Hofmann, R. Smith, and M. H. Chen (2009). „Size and conformation of Ficoll as determined by size-exclusion chromatography followed by multiangle light scattering“. In: *AJP: Renal Physiology* 298.1, F205–F208 (cit. on p. 5).

Fouxon, Itzhak, Sergey Denisov, Vasily Zaburdaev, and Eli Barkai (2017). „Limit theorems for Lévy walks inddimensions: rare and bulk fluctuations“. In: *Journal of Physics A: Mathematical and Theoretical* 50.15, p. 154002 (cit. on pp. 45, 46).

Fujii, Mikako, Satoshi Shibata, and Shin-Ichi Aizawa (2008). „Polar, Peritrichous, and Lateral Flagella Belong to Three Distinguishable Flagellar Families“. In: *Journal of Molecular Biology* 379.2, pp. 273–283 (cit. on p. 4).

Fujime, S., M. Maruyama, and S. Asakura (1972). „Flexural rigidity of bacterial flagella studied by quasielastic scattering of laser light“. In: *Journal of Molecular Biology* 68.2, pp. 347–359 (cit. on p. 12).

Glud, Ronnie N., Frank Wenzhöfer, Mathias Middelboe, et al. (2013). „High rates of microbial carbon turnover in sediments in the deepest oceanic trench on Earth“. In: *Nature Geoscience* 6.4, pp. 284–288 (cit. on p. 1).

Goldstein, Raymond E., Alain Goriely, Greg Huber, and Charles W. Wolgemuth (2000). „Bistable Helices“. In: *Physical Review Letters* 84.7, pp. 1631–1634 (cit. on p. 19).

Goldstein, S. (1951). „On Diffusion by discontinuous movements, and on the telegraph equation“. In: *The Quarterly Journal of Mechanics and Applied Mathematics* 4.2, pp. 129–156 (cit. on p. 43).

Goose, Joseph E. and Mark S. P. Sansom (2013). „Reduced Lateral Mobility of Lipids and Proteins in Crowded Membranes“. In: *PLoS Computational Biology* 9.4. Ed. by Dennis R. Livesay, e1003033 (cit. on p. 73).

Goriely, Alain and Michael Tabor (2000). „The Nonlinear Dynamics of Filaments“. In: *Nonlinear Dynamics* 21.1, pp. 101–133 (cit. on p. 7).

Harshey, Rasika M. (2003). „Bacterial Motility on a Surface: Many Ways to a Common Goal“. In: *Annual Review of Microbiology* 57.1, pp. 249–273 (cit. on p. 31).

Hasegawa, Etsuko, Ritsu Kamiya, and Sho Asakura (1982). „Thermal transition in helical forms of Salmonella flagella“. In: *Journal of Molecular Biology* 160.4, pp. 609–621 (cit. on p. 4).

Hoshikawa, Hiroshi and Ritsu Kamiya (1985). „Elastic properties of bacterial flagellar filaments“. In: *Biophysical Chemistry* 22.3, pp. 159–166 (cit. on p. 12).

Hotani, Hirokazu (1980). „Micro-video study of moving bacterial flagellar filaments II. Polymorphic transition in alcohol“. In: *Biosystems* 12.3-4, pp. 325–330 (cit. on p. 4).

Jawed, M. K., N. K. Khouri, F. Da, E. Grinspun, and P. M. Reis (2015). „Propulsion and Instability of a Flexible Helical Rod Rotating in a Viscous Fluid“. In: *Physical Review Letters* 115.16 (cit. on p. 7).

Kamiya, Ritsu and Sho Asakura (1976a). „Flagellar transformations at alkaline pH“. In: *Journal of Molecular Biology* 108.2, pp. 513–518 (cit. on p. 4).

– (1976b). „Helical transformations of Salmonella flagella in vitro“. In: *Journal of Molecular Biology* 106.1, pp. 167–186 (cit. on p. 4).

Katija, Kakani and John O. Dabiri (2009). „A viscosity-enhanced mechanism for biogenic ocean mixing“. In: *Nature* 460.7255, pp. 624–626 (cit. on p. 31).

Klausen, Mikkel, Arne Heydorn, Paula Ragas, et al. (2003). „Biofilm formation by Pseudomonas aeruginosa wild type, flagella and type IV pili mutants“. In: *Molecular Microbiology* 48.6, pp. 1511–1524 (cit. on p. 3).

Knight, Jefferson D., Michael G. Lerner, Joan G. Marcano-Velázquez, Richard W. Pastor, and Joseph J. Falke (2010). „Single Molecule Diffusion of Membrane-Bound Proteins: Window into Lipid Contacts and Bilayer Dynamics“. In: *Biophysical Journal* 99.9, pp. 2879–2887 (cit. on p. 73).

Kostrzynska, M, J D Betts, J W Austin, and T J Trust (1991). „Identification, characterization, and spatial localization of two flagellin species in Helicobacter pylori flagella.“ In: *Journal of Bacteriology* 173.3, pp. 937–946 (cit. on p. 4).

Kunze, Eric (2011). „Fluid mixing by swimming organisms in the low-Reynolds-number limit“. In: *Journal of Marine Research* 69.4, pp. 591–601 (cit. on p. 31).

Kurtuldu, H., J. S. Guasto, K. A. Johnson, and J. P. Gollub (2011). „Enhancement of biomixing by swimming algal cells in two-dimensional films“. In: *Proceedings of the National Academy of Sciences* 108.26, pp. 10391–10395 (cit. on pp. 31, 54).

Kühn, Marco J., Felix K. Schmidt, Bruno Eckhardt, and Kai M. Thormann (2017). „Bacteria exploit a polymorphic instability of the flagellar filament to escape from traps“. In: *Proceedings of the National Academy of Sciences* 114.24, pp. 6340–6345 (cit. on pp. 4–6, 12, 79).

Kühn, Marco J., Felix K. Schmidt, Nicola E. Farthing, et al. (2018). „Spatial arrangement of several flagellins within bacterial flagella improves motility in different environments“. In: *Nature Communications* 9.1 (cit. on pp. 4, 23, 56, 79).

Landau, Lev D and EM Lifshitz (1986). *Theory of Elasticity, vol. 7*. Vol. 3. Elsevier, New York, p. 109 (cit. on p. 9).

Leptos, Kyriacos C., Jeffrey S. Guasto, J. P. Gollub, Adriana I. Pesci, and Raymond E. Goldstein (2009). „Dynamics of Enhanced Tracer Diffusion in Suspensions of Swimming Eukaryotic Microorganisms“. In: *Physical Review Letters* 103.19 (cit. on pp. 31, 32, 53, 54, 56, 60, 61).

Leshansky, A. M. and L. M. Pismen (2010). „Do small swimmers mix the ocean?“ In: *Physical Review E* 82.2 (cit. on p. 31).

Lighthill, James (1976). „Flagellar Hydrodynamics“. In: *SIAM Review* 18.2, pp. 161–230 (cit. on pp. 7, 11, 13).

Lighthill, M. J. (1952). „On the squirming motion of nearly spherical deformable bodies through liquids at very small reynolds numbers“. In: *Communications on Pure and Applied Mathematics* 5.2, pp. 109–118 (cit. on p. 33).

Lin, Peng, Kai-Yu Qin, and Hai-Yan Wu (2011). „Stability of piecewise-linear models of genetic regulatory networks“. In: *Chinese Physics B* 20.10, p. 108701 (cit. on p. 31).

Liu, B., T. R. Powers, and K. S. Breuer (2011). „Force-free swimming of a model helical flagellum in viscoelastic fluids“. In: *Proceedings of the National Academy of Sciences* 108.49, pp. 19516–19520 (cit. on p. 7).

Macnab, R. M. and D. E. Koshland (1972). „The Gradient-Sensing Mechanism in Bacterial Chemotaxis“. In: *Proceedings of the National Academy of Sciences* 69.9, pp. 2509–2512 (cit. on p. 31).

Macnab, Robert M. and May Kihara Ornston (1977). „Normal-to-curly flagellar transitions and their role in bacterial tumbling. Stabilization of an alternative quaternary structure by mechanical force“. In: *Journal of Molecular Biology* 112.1, pp. 1–30 (cit. on p. 4).

Magariyama, Y., S. Sugiyama, K. Muramoto, et al. (1994). „Very fast flagellar rotation“. In: *Nature* 371.6500, pp. 752–752 (cit. on p. 4).

Magariyama, Y., S. Sugiyama, K. Muramoto, et al. (1995). „Simultaneous measurement of bacterial flagellar rotation rate and swimming speed“. In: *Biophysical Journal* 69.5, pp. 2154–2162 (cit. on p. 4).

Mannik, J., R. Driessen, P. Galajda, J. E. Keymer, and C. Dekker (2009). „Bacterial growth and motility in sub-micron constrictions“. In: *Proceedings of the National Academy of Sciences* 106.35, pp. 14861–14866 (cit. on p. 5).

Marguet, Didier, Pierre-François Lenne, Hervé Rigneault, and Hai-Tao He (2006). „Dynamics in the plasma membrane: how to combine fluidity and order“. In: *The EMBO Journal* 25.15, pp. 3446–3457 (cit. on p. 63).

Martin-Fernandez, M.L., C.J. Tynan, and S.E.D. Webb (2013). „A ‘pocket guide’ to total internal reflection fluorescence“. In: *Journal of Microscopy* 252.1, pp. 16–22 (cit. on p. 73).

Masoliver, Jaume, Josep M. Porrà, and George H. Weiss (1993). „Solution to the telegrapher’s equation in the presence of reflecting and partly reflecting boundaries“. In: *Physical Review E* 48.2, pp. 939–944 (cit. on p. 43).

Maxwell, Clerk (1869). „On the Displacement in a Case of Fluid Motion.“ In: *Proceedings of the London Mathematical Society* s1-3.1, pp. 82–87 (cit. on p. 31).

Mcgill, Robert, John W. Tukey, and Wayne A. Larsen (1978). „Variations of Box Plots“. In: *The American Statistician* 32.1, pp. 12–16 (cit. on p. 24).

Michaud, Luigi, Francescopaolo Cello, Matteo Brilli, et al. (2004). „Biodiversity of cultivable psychrotrophic marine bacteria isolated from Terra Nova Bay (Ross Sea, Antarctica)“. In: *FEMS Microbiology Letters* 230.1, pp. 63–71 (cit. on p. 1).

Miño, Gastón, Thomas E. Mallouk, Thierry Darnige, et al. (2011). „Enhanced Diffusion due to Active Swimmers at a Solid Surface“. In: *Physical Review Letters* 106.4 (cit. on p. 31).

Moerner, W. E. and David P. Fromm (2003). „Methods of single-molecule fluorescence spectroscopy and microscopy“. In: *Review of Scientific Instruments* 74.8, pp. 3597–3619 (cit. on p. 63).

Murphy, Douglas B. and Michael W. Davidson (2012). *Fundamentals of Light Microscopy and Electronic Imaging*. John Wiley & Sons, Inc. (cit. on p. 78).

Nguyen, Frank T.M. and Michael D. Graham (2017). „Buckling Instabilities and Complex Trajectories in a Simple Model of Uniflagellar Bacteria“. In: *Biophysical Journal* 112.5, pp. 1010–1022 (cit. on p. 15).

Park, Yunyoung, Yongsam Kim, William Ko, and Sookkyung Lim (2017). „Instabilities of a rotating helical rod in a viscous fluid“. In: *Physical Review E* 95.2 (cit. on p. 7).

Powers, Thomas R. (2010). „Dynamics of filaments and membranes in a viscous fluid“. In: *Reviews of Modern Physics* 82.2, pp. 1607–1631 (cit. on p. 7).

Pratt, Leslie A. and Roberto Kolter (1998). „Genetic analysis ofEscherichia colibiofilm formation: roles of flagella, motility, chemotaxis and type I pili“. In: *Molecular Microbiology* 30.2, pp. 285–293 (cit. on p. 3).

Purcell, E. M. (1977). „Life at low Reynolds number“. In: *American Journal of Physics* 45.1, pp. 3–11 (cit. on p. 32).

Pushkin, Dmitri O. and Julia M. Yeomans (2013). „Fluid Mixing by Curved Trajectories of Microswimmers“. In: *Physical Review Letters* 111.18 (cit. on pp. 31, 33).

Pushkin, Dmitri O., Henry Shum, and Julia M. Yeomans (2013). „Fluid transport by individual microswimmers“. In: *Journal of Fluid Mechanics* 726, pp. 5–25 (cit. on p. 33).

Ramadurai, Sivaramakrishnan, Andrea Holt, Victor Krasnikov, et al. (2009). „Lateral Diffusion of Membrane Proteins“. In: *Journal of the American Chemical Society* 131.35, pp. 12650–12656 (cit. on p. 73).

Ranjard, Lionel and Agnès Richaume (2001). „Quantitative and qualitative microscale distribution of bacteria in soil“. In: *Research in Microbiology* 152.8, pp. 707–716 (cit. on p. 5).

Reed, Christopher J., Hunter Lewis, Eric Trejo, Vern Winston, and Caryn Evilia (2013). „Protein Adaptations in Archaeal Extremophiles“. In: *Archaea* 2013, pp. 1–14 (cit. on p. 1).

Rodenborn, B., C.-H. Chen, H. L. Swinney, B. Liu, and H. P. Zhang (2013). „Propulsion of microorganisms by a helical flagellum“. In: *Proceedings of the National Academy of Sciences* 110.5, E338–E347 (cit. on p. 7).

Samatey, Fadel A., Hideyuki Matsunami, Katsumi Imada, et al. (2004). „Structure of the bacterial flagellar hook and implication for the molecular universal joint mechanism“. In: *Nature* 431.7012, pp. 1062–1068 (cit. on p. 3).

Seville, Mark, Takeshi Ikeda, and Hirokazu Hotani (1993). „The effect of sugars on the morphology of the bacterial flagellum“. In: *FEBS Letters* 332.3, pp. 260–262 (cit. on p. 4).

Shashkova, Sviatlana and Mark C. Leake (2017). „Single-molecule fluorescence microscopy review: shedding new light on old problems“. In: *Bioscience Reports* 37.4, BSR20170031 (cit. on pp. 65, 73).

Son, Kwangmin, Jeffrey S. Guasto, and Roman Stocker (2013). „Bacteria can exploit a flagellar buckling instability to change direction“. In: *Nature Physics* 9.8, pp. 494–498 (cit. on pp. 5, 11).

Thiffeault, Jean-Luc and Stephen Childress (2010). „Stirring by swimming bodies“. In: *Physics Letters A* 374.34, pp. 3487–3490 (cit. on pp. 31, 36).

Trachtenberg, Shlomo and Ilan Hammel (1992). „The rigidity of bacterial flagellar filaments and its relation to filament polymorphism“. In: *Journal of Structural Biology* 109.1, pp. 18–27 (cit. on p. 12).

Vazquez, S.C., L.N. Rios Merino, W.P. MacCormack, and E.R. Fraile (1995). „Protease-producing psychrotrophic bacteria isolated from Antarctica“. In: *Polar Biology* 15.2 (cit. on p. 1).

Vembu, S. (1961). „Fourier transformation of the n-dimensional radial delta function“. In: *The Quarterly Journal of Mathematics* 12.1, pp. 165–168 (cit. on p. 47).

Visser, A. W. (2007). „OCEAN SCIENCE: Biomixing of the Oceans?“ In: *Science* 316.5826, pp. 838–839 (cit. on p. 31).

Vogel, R. and H. Stark (2010). „Force-extension curves of bacterial flagella“. In: *The European Physical Journal E* 33.3, pp. 259–271 (cit. on p. 19).

– (2012). „Motor-driven bacterial flagella and buckling instabilities“. In: *The European Physical Journal E* 35.2 (cit. on pp. 7, 13, 15).

Vogel, Reinhard (2012). „The bacterial flagellum: Modeling the dynamics of the elastic filament and its transition between polymorphic helical forms“. PhD thesis. Technische Universitaet Berlin (cit. on p. 10).

Wada, H. and R. R. Netz (2008). „Discrete elastic model for stretching-induced flagellar polymorphs“. In: *EPL (Europhysics Letters)* 82.2, p. 28001 (cit. on p. 19).

Wang, Qingfeng, Asaka Suzuki, Susana Mariconda, Steffen Porwollik, and Rasika M Harshey (2005). „Sensing wetness: a new role for the bacterial flagellum“. In: *The EMBO Journal* 24.11, pp. 2034–2042 (cit. on p. 3).

Weart, Richard B., Amy H. Lee, An-Chun Chien, et al. (2007). „A Metabolic Sensor Governing Cell Size in Bacteria“. In: *Cell* 130.2, pp. 335–347 (cit. on p. 73).

Wei, Y., X. Wang, J. Liu, et al. (2011). „The population dynamics of bacteria in physically structured habitats and the adaptive virtue of random motility“. In: *Proceedings of the National Academy of Sciences* 108.10, pp. 4047–4052 (cit. on p. 5).

Weiß, Kerstin, Andreas Neef, Qui Van, et al. (2013). „Quantifying the Diffusion of Membrane Proteins and Peptides in Black Lipid Membranes with 2-Focus Fluorescence Correlation Spectroscopy“. In: *Biophysical Journal* 105.2, pp. 455–462 (cit. on p. 73).

Wildenberg, Siet M. J. L. van den, Bram Prevo, and Erwin J. G. Peterman (2011). „A Brief Introduction to Single-Molecule Fluorescence Methods“. In: pp. 81–99 (cit. on pp. 63, 73).

Wolf, K. (2013). *Integral transforms in science and engineering*. Springer Us (cit. on p. 44).

Wu, Xiao-Lun and Albert Libchaber (2000). „Particle Diffusion in a Quasi-Two-Dimensional Bacterial Bath“. In: *Physical Review Letters* 84.13, pp. 3017–3020 (cit. on pp. 31, 54).

Xie, L., T. Altindal, S. Chattopadhyay, and X.-L. Wu (2011). „Bacterial flagellum as a propeller and as a rudder for efficient chemotaxis“. In: *Proceedings of the National Academy of Sciences* 108.6, pp. 2246–2251 (cit. on p. 5).

Yeomans, J. M., D. O. Pushkin, and H. Shum (2014). „An introduction to the hydrodynamics of swimming microorganisms“. In: *The European Physical Journal Special Topics* 223.9, pp. 1771–1785 (cit. on pp. 31, 32).

Yu, J. (2006). „Probing Gene Expression in Live Cells, One Protein Molecule at a Time“. In: *Science* 311.5767, pp. 1600–1603 (cit. on p. 63).

Zaburdaev, V., I. Fouxon, S. Denisov, and E. Barkai (2016). „Superdiffusive Dispersals Impart the Geometry of Underlying Random Walks“. In: *Physical Review Letters* 117.27 (cit. on p. 45).

Zaid, I. M., J. Dunkel, and J. M. Yeomans (2011). „Levy fluctuations and mixing in dilute suspensions of algae and bacteria“. In: *Journal of The Royal Society Interface* 8.62, pp. 1314–1331 (cit. on p. 31).

Colophon

This thesis was typeset with LaTeX 2_ε. It uses the *Clean Thesis* style developed by Ricardo Langner. The design of the *Clean Thesis* style is inspired by user guide documents from Apple Inc.

Download the *Clean Thesis* style at http://cleanthesis.der-ric.de/.

Wissenschaftlicher Werdegang

2012 - 2017	Wissenschaftlicher Mitarbeiter der Arbeitsgruppe ”Komplexe Systeme”
Februar 2012	Diplom Physik
2011 - 2012	Diplomarbeit Physik in der Arbeitsgruppe ”Komplexe Systeme” ”Experiment Design for Parameter Estimation In Gene Regulatory Networks”
2008	Vordiplom Physik
2006 - 2012	Studium der Physik (Diplom) Philipps Universität Marburg